The Astrophysical Journal, 854:29 (33pp), 2018 February 10 https://doi.org/10.3847/1538-4357/aaa76e

The Number Density Evolution of Extreme Emission Line Galaxies in 3D-*HST*: Results from a Novel Automated Line Search Technique for Slitless Spectroscopy*

Michael V. Maseda[1,2], Arjen van der Wel[2], Hans-Walter Rix[2], Ivelina Momcheva[3], Gabriel B. Brammer[3], Marijn Franx[1], Britt F. Lundgren[4], Rosalind E. Skelton[5], and Katherine E. Whitaker[6]
[1] Leiden Observatory, P.O. Box 9513, 2300 RA, Leiden, The Netherlands; maseda@strw.leidenuniv.nl
[2] Max-Planck-Institut für Astronomie, Königstuhl 17, D-69117 Heidelberg, Germany
[3] Space Telescope Science Institute, 3700 San Martin Drive, Baltimore, MD 21218, USA
[4] Department of Physics, University of North Carolina Asheville, One University Heights, Asheville, NC 28804, USA
[5] South African Astronomical Observatory, P.O. Box 9, Observatory, 7935, South Africa
[6] Department of Physics, University of Connecticut, 2152 Hillside Road, Unit 3046, Storrs, CT 06269, USA
Received 2015 September 3; revised 2018 January 12; accepted 2018 January 12; published 2018 February 8

Abstract

The multiplexing capability of slitless spectroscopy is a powerful asset in creating large spectroscopic data sets, but issues such as spectral confusion make the interpretation of the data challenging. Here we present a new method to search for emission lines in the slitless spectroscopic data from the 3D-*HST* survey utilizing the Wide-Field Camera 3 on board the *Hubble Space Telescope*. Using a novel statistical technique, we can detect compact (extended) emission lines at 90% completeness down to fluxes of $1.5(3.0) \times 10^{-17}$ erg s^{-1} cm^{-2}, close to the noise level of the grism exposures, for objects detected in the deep ancillary photometric data. Unlike previous methods, the Bayesian nature allows for probabilistic line identifications, namely redshift estimates, based on secondary emission line detections and/or photometric redshift priors. As a first application, we measure the comoving number density of Extreme Emission Line Galaxies (restframe [O III] λ5007 equivalent widths in excess of 500 Å). We find that these galaxies are nearly 10× more common above $z \sim 1.5$ than at $z \lesssim 0.5$. With upcoming large grism surveys such as *Euclid* and *WFIRST*, as well as grisms featured prominently on the NIRISS and NIRCam instruments on the *James Webb Space Telescope*, methods like the one presented here will be crucial for constructing emission line redshift catalogs in an automated and well-understood manner.

Key words: galaxies: dwarf – galaxies: evolution – galaxies: starburst – galaxies: statistics – methods: statistical – quasars: emission lines

1. Introduction

In recent years, combinations of deep imaging and spectroscopy with the *Hubble Space Telescope* (*HST*) have been used to tackle a number of outstanding questions in observational astronomy. The *HST* has a particular advantage in the near-IR with the Wide-Field Camera 3 (WFC3), due to the lower sky background levels compared to ground-based observatories and the higher spatial resolution. Using the grism, all sources within the $\sim 2' \times 2'$ WFC3/IR field of view have dispersed spectra, which are essentially a series of monochromatic (overlapping) two-dimensional images shifted on the detector according to their wavelength. The combined spatial and spectral information gives insight into, for example, the growth of disks and bulges at high-redshifts (Hathi et al. 2009; van Dokkum et al. 2013; Patel et al. 2013), the spatial distribution of star formation (Nelson et al. 2012), the regulation star formation in massive galaxies (Ferreras et al. 2012), and the role of environment and mergers in shaping the galaxy population (Schmidt et al. 2013). Additionally, these surveys are very efficient at covering large areas with a superior multiplexing capacity compared to even the most advanced multi-object spectrographs, allowing for complete studies of rare objects such as cold brown dwarfs (Masters et al. 2012) or $4 < z < 7$ Lyman-break and Lyα-emitting galaxies (Pirzkal et al. 2004; Malhotra et al. 2005; Rhoads et al. 2009).

That being said, slitless grism spectroscopic data are more complex to interpret than standard spectroscopic data. Contamination from unrelated spectra makes a detailed analysis of individual objects challenging, particularly in crowded fields, and often only sources detected via shallow ancillary imaging are analyzed, limiting the potential for discovery. As emission lines contain so much astrophysically interesting information and are the easiest spectral features to detect in faint sources, their detection tends to be the primary focus of grism surveys. Different methods for their discovery have been developed and tuned to the various strengths of the specific set of observations.

Meurer et al. (2007) outline two techniques for finding emission lines in a semi-automated fashion. The first method relies on the detection of sources in the direct image. Each source has its corresponding grism spectrum extracted, and emission lines are detected by visual inspection. This is the preferred method of the *WISP* survey (Atek et al. 2010), a pure-parallel survey using WFC3. There, spectral extractions are performed using the *aXe* software (Kümmel et al. 2009) developed to analyze *HST* grism data. Most spectra are taken with both the G102 and G141 grisms, covering an effective wavelength range of 0.8–1.7 μm.

* This work is based on observations taken by the 3D-*HST* Treasury Program and the CANDELS Multi-Cycle Treasury Program with the NASA/ESA *HST*, which is operated by the Association of Universities for Research in Astronomy, Inc., under NASA contract NAS5-26555.

The second method involves searching for emission lines directly in the grism frames. This is done by smoothing the grism frame with a sausage-shaped filter, designed to match the spatial extent of dispersed first-order spectrum, and then subtracting this smoothed image from the original frame. This effectively removes continuum sources from the image while leaving spectrally compact features, such as emission lines, which can be detected using a simple signal-to-noise ratio (S/N) cut. Undispersed zeroth order spectra from the brightest objects also appear as point sources, but their position is well-known and they are easily masked. For each detected feature in this subtracted frame, a cutout of the direct image is inspected to determine which source could have produced the feature. This is the preferred method of the *PEARS* survey (Straughn et al. 2008; Pirzkal et al. 2013) using the *G*800*L* grism of the Advanced Camera for Surveys (ACS) covering 0.5–1.1 μm. That survey has the added advantage of having multiple position angles, such that identification of the source of the emission line in the direct image is simply a matter of identifying the area where the different spectral traces for the same feature intersect.

Both approaches have a serious limitation: while the line candidate identification may be semi-automated, the significance assessment is not, but instead relies on visual inspection, often requiring multiple people to grade the reliability of each line. Such an approach makes a determination of the true completeness difficult and is not feasible for larger data sets. In addition, the first approach only has high fidelity in redshift assignments in cases where more than one line is detected. We jointly analyze photometric redshift information and grism spectra in the determination of redshifts. This differs from the approaches of some of the aforementioned studies that utilize independent photometric redshifts to verify their results. Relying only on multiple line detections introduces problems in the subjective nature of line identification, as well as preferentially selecting objects in certain redshift ranges, typically where both Hα and [O III] $\lambda\lambda$4959,5007 are visible. Indeed, while the quoted flux limit for compact emission lines in *WISP* is 5×10^{-17} erg s^{-1} cm^{-2}, which is based on the WFC3 exposure time calculator, these lines are often only detected in objects that have a second, brighter line.

In this paper, we develop and apply a new method for detecting significant emission features in grism spectroscopic data, using data from the 3D-*HST* survey[7] (van Dokkum et al. 2011; Brammer et al. 2012b). 3D-*HST* is a near-infrared spectroscopic Treasury program utilizing WFC3. This program provides WFC3/IR primary and ACS parallel imaging and grism spectroscopy over approximately three-quarters (~700 square arcminutes) of the CANDELS fields (Grogin et al. 2011; Koekemoer et al. 2011). We focus here on the WFC3 grism data, which utilizes the G141 grism covering 1075–1700 nm.

3D-*HST* provides several advantages over other existing *HST* grism surveys. As the observations are dithered in a four-point pattern, the processed images offer additional robustness against the effect of hot and bad pixels that a pure-parallel survey cannot. We also have the ability to interlace the frames instead of drizzling them, where the pixels from the input images are alternately placed in the output image according to the position of the pixel centers in the original images: see Figure 3 of Brammer et al. (2012b). Interlacing the frames results in better noise characteristics, which is crucial to consider when pushing toward the faint limits of emission line sensitivity; the interlacing procedure is described fully in Momcheva et al. (2016). This also provides higher spatial resolution than drizzling (each interlaced pixel is 23 Å × 0.″06), and the ability to more easily identify point-like emission sources.

The remainder of this paper is organized as follows. In Section 2 we describe the 3D-*HST* data used. Section 3 lays out our new method to search for significant emission lines in slitless spectroscopic data, utilizing photometric information as a redshift/emission line position prior. Extensive tests of the method to determine the completeness function as well as contamination are performed and discussed in Section 4. We apply our method to the 3D-*HST* data set in Section 5 to obtain a sample of high-equivalent width (high-EW) emission line galaxies. We then employ a Bayesian analysis to constrain a parameterized model for their luminosity and redshift distribution. Finally, in Section 6, we summarize and compare these results to previous studies of high-EW galaxies, namely the population of extreme emission line galaxies (EELGs). We adopt a ΛCDM cosmology with $\Omega_m = 0.3$ and $H_0 = 70$ km s^{-1} Mpc^{-1} throughout.

2. Data

The spectroscopic data comes from the 3D-*HST* survey, designed to provide spectroscopy for four well-studied CANDELS extragalactic fields: AEGIS, COSMOS, GOODS-S, and UDS. The data set is supplemented by grism spectroscopy for GOODS-N (PI: B. Weiner). (Undispersed) objects are detected in a combined CANDELS/3D-*HST* F125W+F140W+F160W image, and multiband photometry is obtained as part of the Skelton et al. (2014) photometric catalog. A thorough description of the 3D-*HST* spectroscopic release, which includes extracted 2D grism spectra for all ~250,000 objects in the Skelton et al. (2014) photometric catalog, and data reduction methods are given in Momcheva et al. (2016). We briefly summarize some of the important points here.

A model for the grism spectra of the entire field is created as follows. For a given object, we distribute the light (and consequently the extraction weight in the spatial direction) according to the *EAZY* (Brammer et al. 2008) continuum fit at the photometric redshift estimate, with the spatial extent according to the F125W+F140W+F160W "postage stamp" image of the object. Next, for bright objects ($m_{F140W} < 22$), we use the the extracted spectrum as a second step to give the continuum the correct shape and to take the brightest emission lines into account.

Creating a continuum model individually for all objects allows us to construct a model of the flux distribution for the entire field. This is useful because of spectral confusion due to overlapping unassociated spectra in the grism data. Since we create the full modeled spectra for each pointing, each extracted 2D spectrum has the modeled spectra from surrounding objects ("contamination") subtracted. We also subtract an object's own continuum ("model") in order to search for positive residuals, namely emission features. For the brightest objects, the model does not always subtract cleanly and can lead to spurious detections in neighboring objects, so we also mask any "contamination" regions where the model flux exceeds 0.004 e$^-$ s^{-1} px^{-1} (see Section 4.3). Likewise, as we are

[7] http://3dhst.research.yale.edu/

primarily interested in emission lines with high-equivalent widths in this study (see Section 5), we focus on objects with $F140W_{AB}$ magnitudes fainter than 24.

3. Simple Model Fitting of Emission Lines in 3D-*HST*

In this section we set out to devise a straightforward, probabilistic method to detect emission lines and assess their significance algorithmically. It is based on the following elements: to start, we calculate what the likelihood of the data is, if there was an emission line with amplitude A at a spectral position Δx with respect to the undispersed image. To assess the redshift and significance of any detection, $A > 0$, we incorporate three pieces of independent information as prior beliefs. First, we know that in most instances there is either one or no significant emission line in the entire spectrum of an object; conversely, that means the vast majority of pixels must contain no emission line. Second, any emission line flux we detect must not violate the total flux constraints from the corresponding broadband image. Finally, in many instances, we have photometric information about the probable redshift of the object ("photometric redshift priors"), which also informs our assessment of any emission line detection significance and line identification. Taken together, this results in a joint statement about whether any object has a significant emission line, and if so at which redshift. In other words, line detection and identification are an integrated process.

3.1. Line Detection Formalism

We presume the following algorithm to operate on continuum-subtracted spectra, which we obtain as follows: every object in the Skelton et al. (2014) photometric catalog has a grism spectrum (S') with an associated noise spectrum (σ_S) and a direct F125W+F140W+F160W-combined postage stamp (I, of dimensions $x_{\max}$ and $y_{\max}$). From each grism spectrum, S', we subtract its continuum flux model and a flux model for all contaminating spectra (see Section 2 and Momcheva et al. 2016) to obtain a spectrum S, in which we search for residual emission features.

As a convolution kernel in the line search, we need to construct an empirical template for the expected spatial distribution of a monochromatic line image at any given wavelength. We construct that from the undispersed image, I, applying a S/N cut of 2σ above the background level. For all sources whose undispersed image has fewer than 20 pixels above this threshold, we instead use the *HST* F140W Point Spread Function (PSF) scaled to the same flux as the image. This choice is justified, as the area of 20 (interlaced) pixels is approximately the size of a WFC3 PSF.

Presuming there is a line image of shape I, offset by Δx along the spectrum and characterized by an amplitude scale factor A, we calculate the likelihood of the data as

$$\ln \mathscr{L}(\{S\}|A, \Delta x) = -\frac{1}{2}\sum_{x=0}^{x_{\max}}\sum_{y=0}^{y_{\max}} \frac{(S_m(x, y|A) - S(x + \Delta x, y))^2}{\sigma_S^2(x + \Delta x, y)}, \quad (1)$$

where the spectral emission line model is $S_m(x, y|A) = A \times I(x, y)$. We are dealing with a two-dimensional projection of the three-dimensional spectral information $S(x_{\text{on-sky}}, y_{\text{on-sky}}, \lambda_{\text{rest}})$. In this context, $\ln \mathscr{L}(\{S\}|A, \Delta x)$ represents a correlation between I and S in the dispersion direction for different Δx. Throughout, we use pixel coordinates $\hat{x}$ in the dispersion direction, which of course reflect different wavelengths, $\hat{\lambda}$. The maximum value of Δx corresponds to the length of S, here denoted as $\Delta x_{\max}$. The scale factor A ranges from 0 to 1. At a given position, $A = 0$ implies that there is no signal present in the spectrum. Conversely, $A = 1$ corresponds to a position where the entire flux[8] of the galaxy is contained in a single emission feature with the same spatial extent as the direct image and is unresolved spectrally. (The mean dispersion of the primary spectral order of the G141 grism is 46.5 Å/pixel or $R = 130$.) We calculate the likelihood at each integer value of Δx, noting that the FWHM of the WFC3 PSF is 1.1 native pixels at 1.4 μm.

However, we want the posterior distribution function $p_{\text{posterior}}(A|\{S\}, \Delta x)$ of the possible line amplitude A, not the likelihood of the data. The two are related via Bayes's theorem:

$$p_{\text{posterior}}(A|\{S\}, \Delta x) \propto \mathscr{L}(\{S\}|A, \Delta x) \times p_{\text{prior}}(A|\Delta x). \quad (2)$$

More specifically, we want the probability that there is a significant line detection, $A > 0$, at any given position:

$$p(A > 0|\{S\}, \Delta x) = \int_{>0}^{1} p_{\text{posterior}}(A|\{S\}, \Delta x)dA. \quad (3)$$

This is illustrated in Figure 1. Equation (2) requires the prior information on both A and Δx. Absent informative photometric redshift information (see Section 3.2), $p_{\text{prior}}(\Delta x)$ is flat: $p_{\text{prior}}(\Delta x) = x_{\max}/\Delta x_{\max}$, for the case of one emission line in the entire spectrum. This is typically $\sim 1/300$ (i.e., $\ll 1$). It is this prior $p_{\text{prior}}(\Delta x)$ that accounts for the fact that we query $\Delta x/x_{\max}$ independent positions along the spectrum whether there is a significant line flux. When considering only the likelihood (Equation (1)), we would expect one spurious "3σ-detection" for every $\sim$200 independent spectral positions, in the absence of any emission line and in the absence of any systematic errors or residuals. The factor $p_{\text{prior}}(\Delta x)$ prevents such false detections, as the prior probability that there is *no* line is $1 - p_{\text{prior}}(\Delta x)$.

We have no external information on the possible line flux in any one object, except that A is bound by [0, 1]. Therefore $p_{\text{prior}}(A)$ is flat in [0, 1], normalized by

$$\int_{-\infty}^{\infty} p_{\text{prior}}(A)dA = \int_{0}^{1} p_{\text{prior}}(A)dA = 1. \quad (4)$$

The two priors on A and Δx can be combined to

$$p_{\text{prior}}(A|\Delta x) = (1 - p_{\text{prior}}(\Delta x)) \times \delta(A = 0) + p_{\text{prior}}(\Delta x) \times p_{\text{prior}}(A), \quad (5)$$

where $\delta(A = 0)$ is the Kronecker delta function.

The question of whether there is any significant line detection in the entire spectrum then boils down to asking whether there are any parts of the spectrum for which $p(A > 0|\{S\}, \Delta x) > p_{\text{threshold}}$ is very high (e.g., $p_{\text{threshold}} > 0.997$). In practice, we expect such regions in Δx to have the extent of the PSF or postage stamp size, $x_{\max}$. This formalism is based on the assumption of a single line in the spectrum. If there are two significant lines (e.g., [O III]

[8] The spectral range of the F125W+F140W+F160W filter combination overlaps with the G141 grism such that those filters cover a slightly larger wavelength range than the grism.

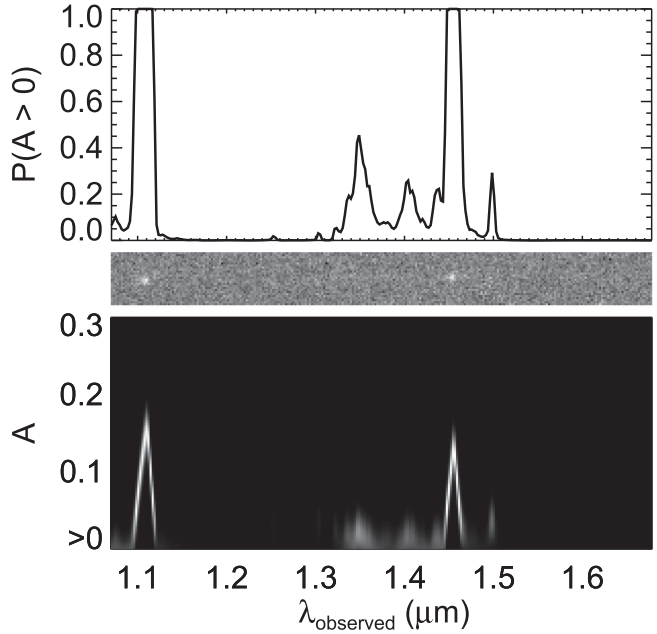

Figure 1. Illustration of Equation (3) for GOODS-S-38590. The bottom panel illustrates the two-dimensional probability array $p_{\rm posterior}(A|\{S\}, \Delta x)$ with the color coding ranging from black (zero probability) to white (high probability). By marginalizing this probability distribution over all nonzero values of A, we arrive at the top panel, which is the same as the bottom set of panels in Figure 3. The object's G141 spectrum is shown in the middle panel.

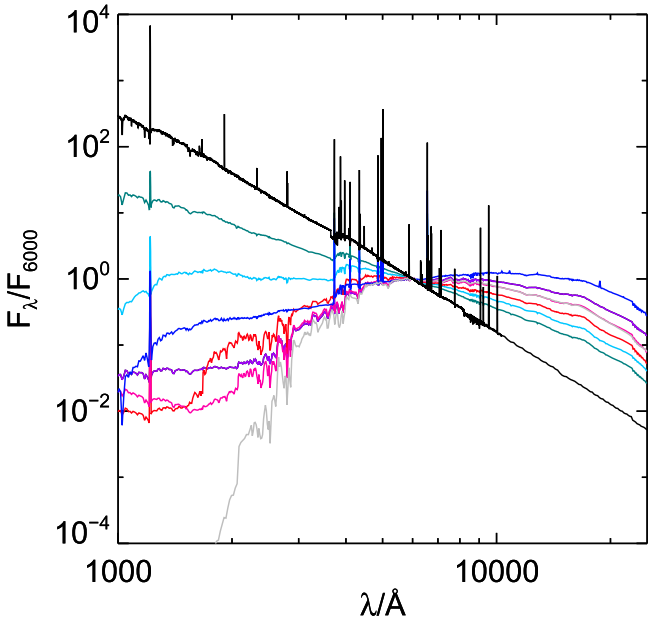

Figure 2. Photometric templates used in our application of *EAZY* (Brammer et al. 2008) normalized at 6000 Å. The colored templates are the default *EAZY* set, created following the Blanton & Roweis (2007) algorithm with PÉGASE models (Fioc & Rocca-Volmerange 1997) and a calibration set of synthetic photometry derived from semi-analytic models, while the black and gray templates are an EELG (from Maseda et al. 2014) and a 1.5 Gyr Bruzual & Charlot (2003) SSP with $A_V = 2.5$ to fully reproduce the SEDs of the bluest and reddest objects in the sample. All galaxy SEDs are fit with linear combinations of these templates.

and Hα), then we would expect two disjoint regions in Δx with significant $p(A > 0|\{S\}, \Delta x) > p_{\rm threshold}$.

If a single position Δx meets the threshold, then we simply translate it into a wavelength λ, a single value of A which can be transformed into a line flux in physical units (also taking into account the normalized wavelength-dependent grism sensitivity), and an uncertainty on that flux given the distribution of $p_{\rm posterior}(A|\{S\}, \Delta x)$. However, given that we are dealing with three-dimensional spectra, a bright emission line in an object that is not a point source produces significant detections of A at positions near the intrinsic $\lambda_{\rm central}$. Our best estimate of the central line position is the "significant" pixel responsible for the maximum peak in $p_{\rm posterior}(A|\{S\})$.

3.2. Incorporating Photometric Redshift Priors

A strength of this approach is that independent information about the likely redshift of the objects can be folded-in straightforwardly and stringently: it simply gets incorporated as a non-constant $p_{\rm prior}(\Delta x)$ in Equation (5). Given the amount of ancillary photometry in the 3D-*HST*/CANDELS fields, spanning from UV to IR wavelengths, specifically 0.3–8 μm, it is straightforward to estimate the redshifts photometrically for the sample (a full description is given in Brammer et al. 2012b). Briefly, we calculate photometric redshifts by applying *EAZY*, which calculates model fluxes by convolving linear combinations of high-resolution spectral templates with the filter transmission curves, to the broadband spectral energy distributions (SEDs) in order to estimate a probability distribution for the redshift, $P(z)$. In addition to the default *EAZY* template sets, we include an additional dusty star-forming template (a Bruzual & Charlot 2003, SSP of 1.5 Gyr and $A_V = 2.5$) and an EELG template (the highest sSFR galaxy from Maseda et al. 2014, UDS-6195), as shown in Figure 2. We choose to use this $P(z)$ distribution in cases when the minimum reduced χ^2 value is less than 5, which happens in ∼90% of the cases; otherwise we adopt a flat $P(z)$ prior. This is illustrated in the upper two panels of Figure 3.

For a single line detection in a given spectrum, we do not know which restframe emission feature it corresponds to. The strongest (blended) emission line complexes we expect to typically observe are Paβ λ12820, He I λ10830, [S III] λ9530, $H\alpha$ λ6563, [O III] $\lambda\lambda$5007,4861, [O II] $\lambda\lambda$3727,3729, and Mg II λ2800. This implies that we are only searching for sources with $z \lesssim 5.1$.[9] We convolve the redshift prior $P(z)$ with the restframe wavelengths of these emission lines to determine a prior probability of a line detection as a function of observed wavelength. At each wavelength within the G141 grism coverage, we determine the probability of a line being present at the pixel position corresponding that wavelength $P(\Delta x)$ is the combined value of the individual line PDFs at that position. Examples are shown in Figure 3. As noted in Skelton et al. (2014), there are indeed some cases in which the photometric redshift for a given object varies greatly from its spectroscopic redshift. This (small) percentage varies from field to field and is likely a function of magnitude, so we adopt a floor in our PDF such that only 98% of the total probability is allocated according to the photometric prior and distribute the remaining 2% uniformly across all observed wavelengths.

[9] This is the redshift where we lose Mg II from the grism coverage. For the photometric redshifts, *EAZY* is run with $z < 6$. A search for higher-redshift restframe-UV emission lines in this grism data is the subject of ongoing work.

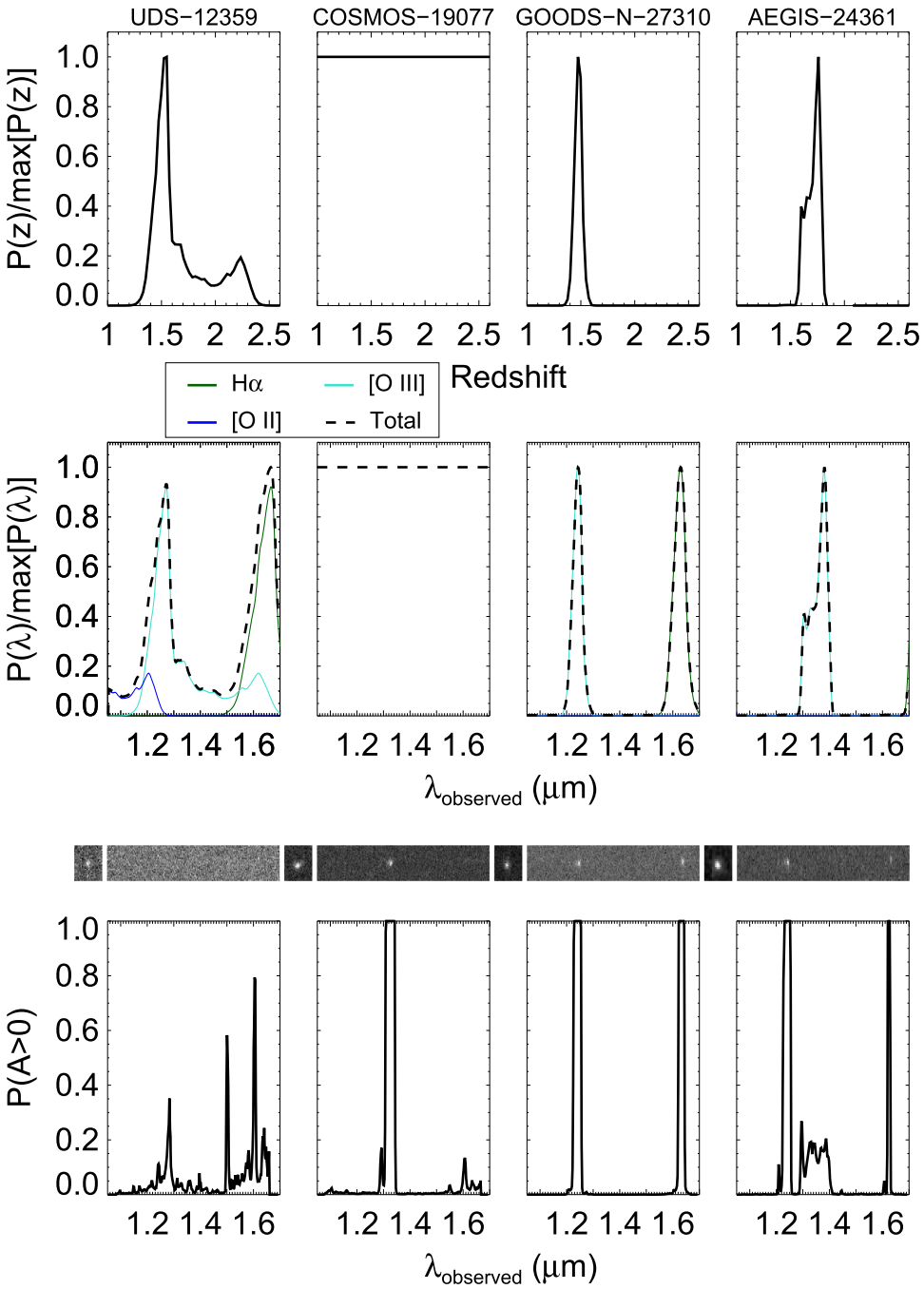

Figure 3. Illustration of the line search process for (left to right) UDS-12359, COSMOS-19077, GOODS-N-27310, and AEGIS-24361. From top to bottom: photometric redshift probability distribution from EAZY ($P(z)$; Brammer et al. 2008), the prior on line positions $P(\Delta x)$ derived from $P(z)$ for lines in the correct observed wavelength range, the direct (undispersed) and grism images for the objects, and the output probability at each wavelength position Δx that A is nonzero (Equation (3)). The colored curves denote the expected positions of Hα, [O III], and [O II] given $P(z)$, while the black curve denotes the overall $P(\lambda)$ for all emission lines that could fall in the grism coverage. Note that in this case, Mg II, [S III], He I, and Paβ do not appreciably contribute any probability for these objects in this observed wavelength range. In the case of UDS-12359, no significant ($>3\sigma$) line detections are found; for COSMOS-19077 (one of the objects studied in Maseda et al. 2013, 2014), a strong line is discovered despite assuming a flat $P(\lambda)$ due to a high-χ^2 EAZY fit: this object's redshift cannot be reliably determined and is therefore excluded; for GOODS-N-27310, the $P(z)$ correctly predicts the positions of the emission lines; and for AEGIS-24361, the lines are slightly offset from the predicted position (although we detect them regardless).

3.3. Redshifts

For every measured emission line, we must determine the redshift of the galaxy. We iteratively assume that the strongest detected line in the grism is Paβ, He I, [S III], Hα, [O III], [O II], and Mg II, and calculate the detection significance at the predicted positions of the other emission lines. If we have significant detection(s) at the predicted position(s), then we have a secure redshift determination. In the case where we do not find a significant additional emission line, we automatically identify the detected line according to the highest probability for a given line species at that wavelength position according to the photometric redshift information.

As a final check, we visually inspect all detected lines to verify that the detection is not caused by severe contamination

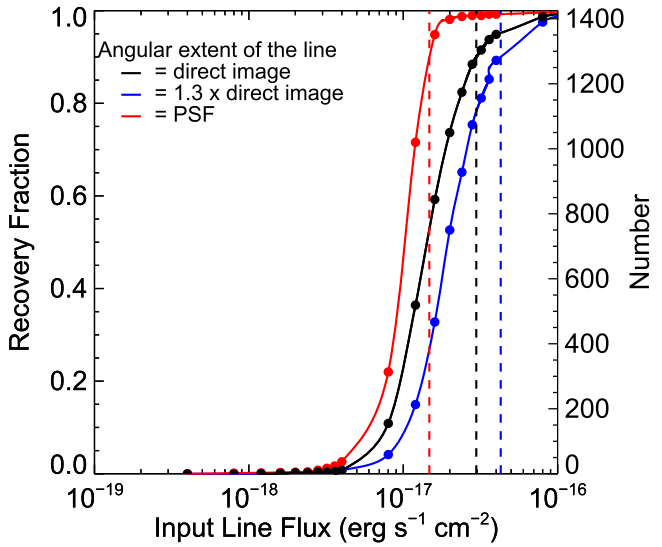

Figure 4. Completeness of line recovery test as a function of the fake emission line flux, inserted at 1.4 μm. Black denotes an emission line with the same profile as the direct image, blue denotes an emission line that is 1.3 times larger (Nelson et al. 2012), and red denotes an emission line the size of the F140W PSF. At 90% completeness, we find flux limits of 3.0×10^{-17} erg s^{-1} cm^{-2}, 4.4×10^{-17} erg s^{-1} cm^{-2}, and 1.5×10^{-17} erg s^{-1} cm^{-2}, with vertical dashed lines denoting these limits.

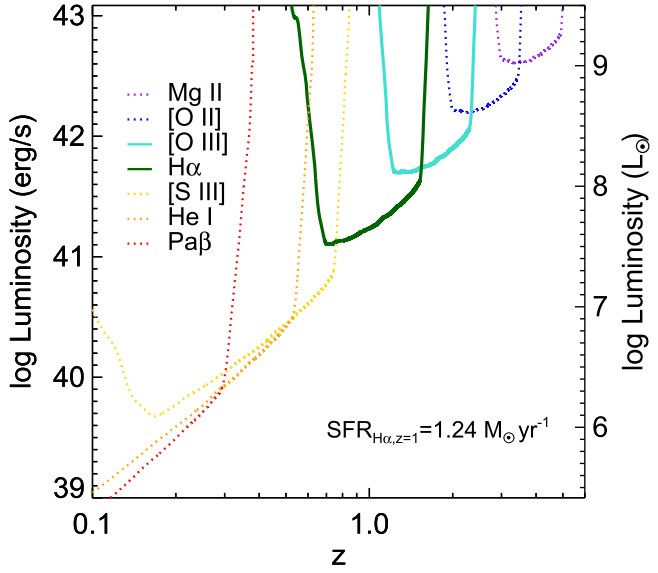

Figure 5. Line luminosity at our 90% completeness limit for direct images, 3.0×10^{-17} erg s^{-1} cm^{-2}, as a function of line species and redshift (dotted lines denote the luminosities for lines we do not consider in constructing our "high-EW" sample; see Section 5). The Hα star formation rate comes from the calibrations of Kennicutt (1998).

or artifacts at the very edges of the detector:[10] this occurs in less than ~5% of spectra (see Section 4.3). We also classify objects based on the agreement between the emission line redshift and the photometric redshift: some objects have significant detections of lines and photometric redshift information that either does not provide strong constraints at the position of the line, and thus the line identification is somewhat dubious, or provides no information due to the reduced-χ^2 cut. Further details on these "unknown" objects are presented in Section 5.2.

4. Completeness of the Sample

While grism spectroscopy allows us in principle to search for emission lines in an unbiased manner, several important issues affect our search completeness.

4.1. Line Detection Limits

The primary test of the method's efficacy is to insert fake emission lines into spectra and attempt to recover them. In order to do this, we identify a control sample of 1425 objects representing a variety of galaxy sizes and morphologies where our search method does not return any spectral positions with a significant detection. We insert a fake emission line at 1.4 μm, which is simply the direct image of the object scaled to a given flux value. We then run our search algorithm, focusing on a $\pm$7 pixel region around 1.4 μm (corresponding to the average physical extent of a galaxy in this sample based on the Kron radii from the Skelton et al. 2014 photometric catalog) to see how many lines are recovered as a function of the scaled flux value. In addition, previous work from 3D-*HST* has shown that typical star-forming galaxies have star formation (as traced by Hα emission) out to ~30% larger radii than the restframe *R*-band stellar continuum (Nelson et al. 2012). We also repeat this test, making the artificial emission line 30% larger at the same integrated flux value.

The results of this test are shown in Figure 4. At 90% completeness, we find a flux limit of 3.0×10^{-17} erg s^{-1} cm^{-2} for the compact line case and 4.4×10^{-17} erg s^{-1} cm^{-2} for the extended line case. When we insert an artificial line with the spatial extent of the F140W PSF, we obtain a 90% completeness limit of 1.5×10^{-17} erg s^{-1} cm^{-2}. This value is comparable to the theoretical point-source calculation from simulated 3D-*HST* G141 spectra of 1.6×10^{-17} erg s^{-1} cm^{-2} at the same completeness (Brammer et al. 2012b). Background-limited grism line searches such as these are primarily sensitive to surface brightness, which is why the black curve in Figure 4, representing a sample with a larger dispersion in object sizes, rises more slowly than the red PSF curve. When we enlarge *all* emission lines by 30%, we decrease the surface brightness of all galaxies at a given flux, and hence we become less sensitive.

Line sensitivity will also vary by wavelength, according to the throughput of the grism. We have performed all of these tests at 1.4 μm, close to the center of the G141 grism. The true sensitivity of our method at a given wavelength, then, is the above-quoted line sensitivity scaled according to the ratio of the 1.4 μm throughput to the throughput at the observed wavelength (see Figure 5). We can convert this flux completeness limit as a function of observed wavelength into a luminosity completeness limit as a function of redshift and line species, as illustrated in Figure 5.

4.2. False Positives

While the above test determines the flux limit at which an emission line is likely to be recovered, it does not inform us how often a noise peak or artifact would be detected significantly. In order to investigate this, we isolate contiguous regions of the grism pointing that do not have continuum model fluxes above

[10] We do not intend to visually verify the existence of the line, but rather to eliminate cases of obvious contamination. Our Bayesian framework eliminates the need for subjective visual searches.

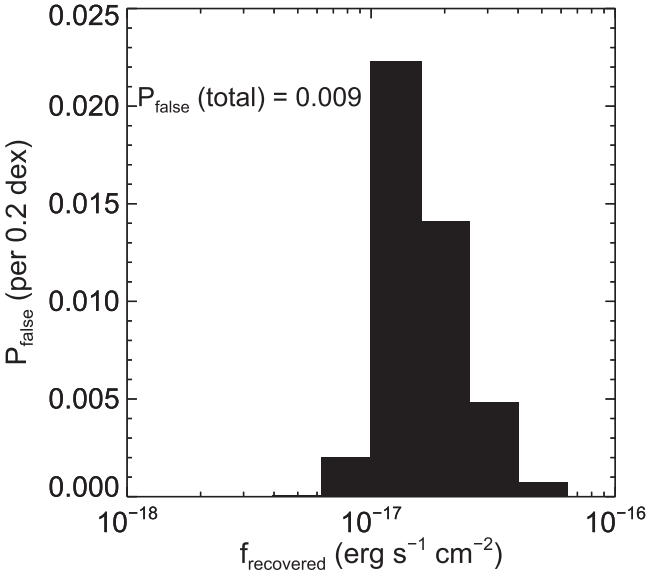

Figure 6. Histogram of recovered line fluxes for "blank" spectra as part of the search for false positives. In 0.2 dex wide bins of recovered line flux, we plot the probability that a line with a measured flux is due to a spurious feature. For the full range in fluxes, redshifts, and equivalent widths, this corresponds to 0.88%. The lack of false detections below 10^{-17} erg s^{-1} cm^{-2} is due to the additional line completeness limits shown in Figure 4.

5×10^{-5} e^- s^{-1} px^{-1} for each field and create artificial 2D extractions, each 284 × 31 pixels in size. As these regions are unlikely to contain real spectral information, any peaks represent noise, unmodeled contamination, or detector artifacts.

We create 176 spectra in this manner, spread across all fields. To mimic our standard line search as closely as possible, we randomly assign one of these "blank" spectra to each of the 159,536 unique objects in the photometric catalog with $m_{\rm det} > 24$ that lie in the 3D-*HST* spectroscopic footprint and perform the standard cross-correlation analysis, also using its photometric redshift prior. Throughout, we utilize the MAG_AUTO value as described in Momcheva et al. (2016). This is important when determining the line fluxes, as this is the magnitude of the object in the same wavelength range as the grism spectrum and within the same segmentation map that we use as the kernel. Overall, 1408 (0.88%) yielded at least one $>3\sigma$ detection (see Figure 6) for all line species and line fluxes.

The number of false positives varies as a function of line flux, as not all cosmetic features and noise peaks are of the same magnitude. As this number is higher than for purely Gaussian noise (which would correspond to 0.27% for 3σ detections), we conclude that the grism exposures contain significant amounts of correlated noise and artifacts that mimic emission features, also due to unmodeled or underpredicted spectral contamination. Additional criteria are applied to create useful samples (e.g., a cut on EW as in Section 5), and thus true contamination levels are likely lower than this.

4.3. Contamination

Due to the slitless nature of grism spectroscopy, some sources are strongly contaminated by overlapping spectra from brighter sources. Chance alignment of sources in the direct image could result in both having "detections" of the same emission line in the grism data, especially if both sources are spatially small. There is no automated way to account for such events, so we must resort to visual inspection: for all objects with detected emission lines, we search for all other objects with detected emission lines that lie in a rectangular aperture with an extent corresponding to the G141 dispersion size (284 interlaced pixels). If multiple sources "produce" the same emission line, we assign the line to a single source based on the overlap with the expected trace of the source (a direct overlap as opposed to a glancing one) and the F140W morphology of the sources.

As described in Section 2 and Momcheva et al. (2016), we have a sophisticated flux model for each object in a pointing. The modeled flux for neighboring sources is subtracted when searching for emission lines in an object's spectrum to avoid potential false detections. Each object's own flux distribution is also subtracted: the flat flux distribution represents the continuum level of an object, which needs to be subtracted in order to discover residual emission lines.

The model, however, occasionally does not subtract perfectly, and we are left with residual flux. This typically scales with the flux of the object, such that brighter regions tend to have larger residuals. Regions of positive residual (S'-Model) appear like spectral features in that they are areas of "real" flux above the background level. These regions are identified as emission features, both in the (bright) object that created the original spectrum and in spectra of objects that happen to overlap with them. We mask out any pixels that have a flux level in the model higher than a threshold value. We seek to strike a balance between masking as few pixels as possible, maximizing our search area, and minimizing the chance of contamination leading to false detections. We select this masking level by utilizing the same framework as in Section 4.2. We determine the number of line detections at or below 10^{-17} erg s^{-1} cm^{-2}, where we should be only ∼10% complete, as a function of the masking threshold. The number of "detections" per pixel is nearly zero when we mask regions where the model flux exceeds 0.004 e^- s^{-1} px^{-1}. This level corresponds to the counts in the central pixel from a dispersed point source of an unresolved emission line with a flux of $\sim 1.7 \times 10^{-20}$ erg s^{-1} cm^{-2} at 1.4 μm. However, once we change to a lower threshold (i.e., the masked region corresponds to brighter fluxes and hence covers a smaller area), we begin to see increasing number counts. We therefore select this as our masking threshold, as it maximizes the usable area while still removing as many potentially problematic regions of the grism frame as possible.

The primary issue for contamination from overlapping spectra, then, comes from the limited area in which we search for lines after applying this masking. The total unusable area depends on the specific pointing in question, but is equal to 18% when averaged over the whole survey area with a standard deviation of 4.1%. There are some specific cases in which the model fails to account for a particularly bright spectrum, typically in higher-orders for bright stars, and we are left with "uncontaminated" regions of residual flux. These cases are obvious to identify and are a reason why all objects with detections are visually inspected.

4.4. Completeness of the Photometric Catalog

The starting point of this search is the photometric catalog of Skelton et al. (2014). Therefore we do not analyze spectra for sources that are not in the input photometric catalog.

In the left panel of Figure 7, we show the completeness fraction of the photometric catalog as a function of line flux and equivalent width, assuming a single emission line is placed in the H_{F160W} filter. This is the emission line version of Figure 14 in Skelton et al. (2014). The 90% catalog completeness limit is

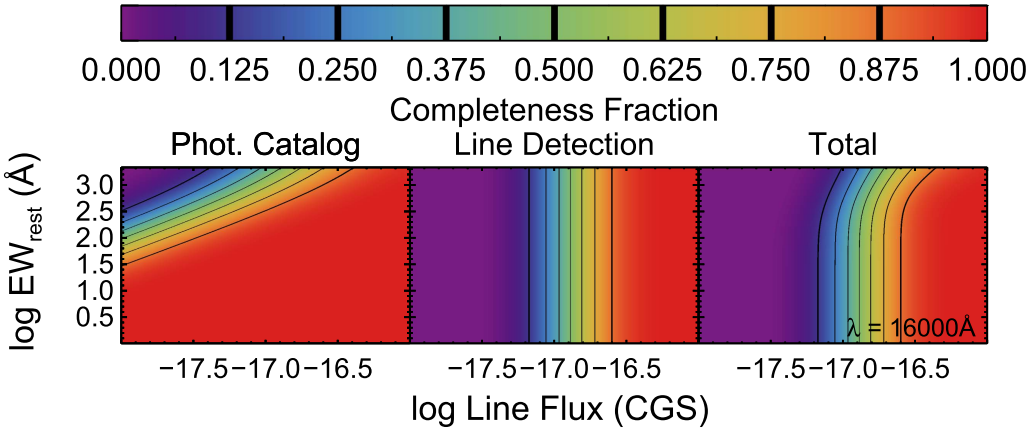

Figure 7. Completeness fraction as a function of line flux and equivalent width at a fixed line position (16,000 Å). The left panel shows the completeness of the Skelton et al. (2014) photometric catalog for objects of a given flux and equivalent width (i.e., continuum magnitude), the central panel shows the flux completeness of our line search from Figure 4 and the G141 sensitivity at that position, and the right panel shows the combination of these two completeness functions. This wavelength correspond to Hα at $z = 1.4$ or [O III] at $z = 2.2$. There are small variations in the grism sensitivity as a function of wavelength, as well as catalog completeness limits that vary by field, but this information is also taken into account in this analysis.

$H_{F160W} = 25.1$, which corresponds to an emission line flux of $\sim 10^{-16}$ erg s^{-1} cm^{-2} if entirely concentrated in a single line of infinite equivalent width. Note that for a given line flux, we are more likely to have the object in the photometric catalog if it has a *lower* equivalent width, as that implies the continuum level is higher.

The requirement that an object must be in the photometric catalog is the single strongest prior we apply to our data. If an emission line source is not in that catalog, by definition we will not be able to detect the line. In the range of fluxes where we can still robustly detect lines, our catalog completeness is approximately 60% for high-EW sources. A full catalog of emission lines for 3D-*HST* galaxies will be presented in M. V. Maseda et al. (2018, in preparation), utilizing a deeper photometric catalog to overcome the issues mentioned here. A comparison of this method to photometric methods for finding high-EW galaxies, namely the *iJH*-selection of van der Wel et al. (2011), is given in Appendix A.

5. A Sample of High-equivalent Width [O III] and Hα Emitters

We apply our method to 93,832 unique objects in 3D-*HST* with full spectral coverage. For objects with multiple spectra due to the overlapping individual pointings, we adopt the redshift corresponding to the highest individual line detection probability. In total, we find 22,786 objects with at least one emission line. In order to estimate line equivalent widths, we use the Skelton et al. (2014) catalog F125W, F140W, or F160W magnitude (depending on the line position) and the measured line flux from 3.1.

In Figure 8 we show the flux histograms for [O III] and Hα emitters from this method and from that of Momcheva et al. (2016). These methods are quite complimentary, given the optimizations for faint lines in objects without strong continuum flux presented in this work.

Here we present a first application of our approach: to measure the number density evolution of extreme EW galaxies with redshift, specifically from $0.7 < z < 2.3$ with an extreme restframe-optical emission line EW ([O III] in excess of 500 Å and/or Hα in excess of 424 Å; see Section 5.2 for specific information about the cuts used). A full analysis of all

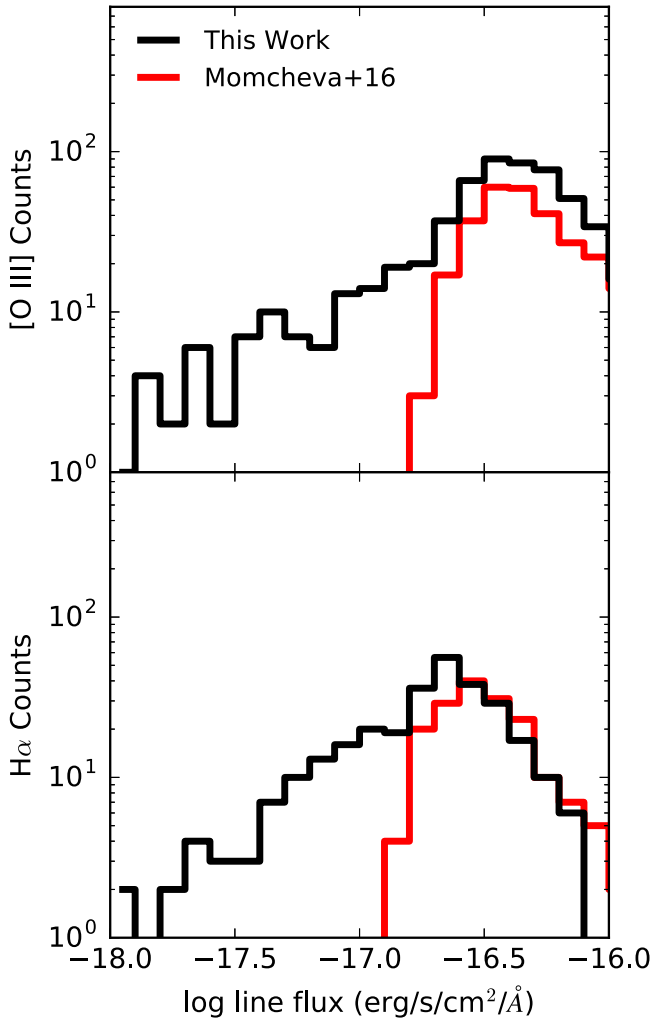

Figure 8. Flux comparison between detected emission lines in the method presented here and that in the 3D-*HST* catalog of Momcheva et al. (2016). The top panel shows the distribution of [O III] emitters and the bottom panel shows the distribution of Hα emitters. In both cases we restrict to objects with 3-σ line detections (flux and EW) and continuum F140W magnitudes fainter than 25. The majority of the lines from this method below fluxes of 10^{-17} erg s^{-1} cm^{-2} are measured due to the presence of a stronger line present in the spectrum (see Section 3.3).

Table 1
Grism and Spectroscopic Redshifts in GOODS-N

ID	$z_{\rm grism}$	$z_{\rm spec}$	$z_{\rm 3D\text{-}HST}$
5878	2.326	0.5583	2.422
7163	2.937	2.931	2.934
7243	1.451	0.8250	1.452
8614	2.287	2.349	2.349
10728	2.975	2.973	2.971
11429	0.9076	2.261	0.9357
11683	1.011	1.016	1.018
12851	2.049	2.088	2.045
13286	2.004	3.162	2.006
14300	1.465	1.457	1.467
14475	2.941	2.939	2.936
16354	2.474	1.652	2.489
16755	1.913	1.919	1.922
17709	3.165	3.161	3.109
19350	2.248	2.427	2.229
20899	2.984	2.987	2.994
21256	2.965	2.962	2.958
21267	1.921	0.4410	1.920
23343	0.7131	0.7431	0.3076
23744	2.303	2.453	2.288
28202	3.255	3.229	3.235
32925	1.976	1.970	1.971

Note. ID numbers and $z_{\rm spec}$ values come from Skelton et al. (2014); $z_{\rm 3D\text{-}HST}$ values come from Momcheva et al. (2016); $z_{\rm grism}$ values are from this work.

line detections and an accompanying catalog is beyond the scope of this methodology paper. With the method outlined in the previous sections, we now have, for the first time, a spectroscopic sample of such objects with a well-quantified selection function. Overall, we have 442 confirmed high-EW [O III] emitters (146 of which have multiple lines) and 340 Hα emitters (117 of which have multiple lines).

Objects with detected lines are put into three classes: multiple significant line detections, single significant line detections with well-known line identifications and hence redshifts from the photometric redshift information, and single significant line detections that have ambiguous identifications either due to broad photometric priors, namely $P([\mathrm{O\ III}]) \sim P(\mathrm{H}\alpha)$, or because they are detected far away from the expected position from the photometry, like a more extreme case than AEGIS-24361 in the right panels of Figure 3.

5.1. Verification of Redshifts

In order to demonstrate the accuracy of our new grism redshifts, we compare them to existing ground-based spectroscopic redshifts. Such samples are typically derived at optical wavelengths for the brighter objects in the sample. While none of our high-EW [O III] and Hα emitters have existing published ground-based spectroscopic redshifts, 22 galaxies in our GOODS-N sample have spectroscopic redshifts (see $z_{\rm spec}$ in Skelton et al. 2014), as well as robust grism redshifts. Of these 22, eight have values that disagree by more than $\Delta z = 0.1$. We note that all eight have published grism redshifts from Momcheva et al. (2016) that agree with our grism redshifts to better than $\Delta z = 0.03$ using an independent analysis of the same data with a different method. These values are summarized in Table 1 and Figure 9.

When considering the $z_{\rm spec}$ values, some care must be taken. Skelton et al. (2014) note that, for GOODS-N, "no quality flags were provided, so there is a mix of reliable and less reliable redshifts in this field." Two examples where $z_{\rm spec}$ and $z_{\rm grism}$ disagree are shown in Figure 10. In these cases, we identify a secure redshift based on the combination of the photometric information and the clear asymmetric profile of the unresolved [O III] doublet (upper panel; GOODS-N-13286), as well as detections of both [O III] and Hα (lower panel; GOODS-N-07243).

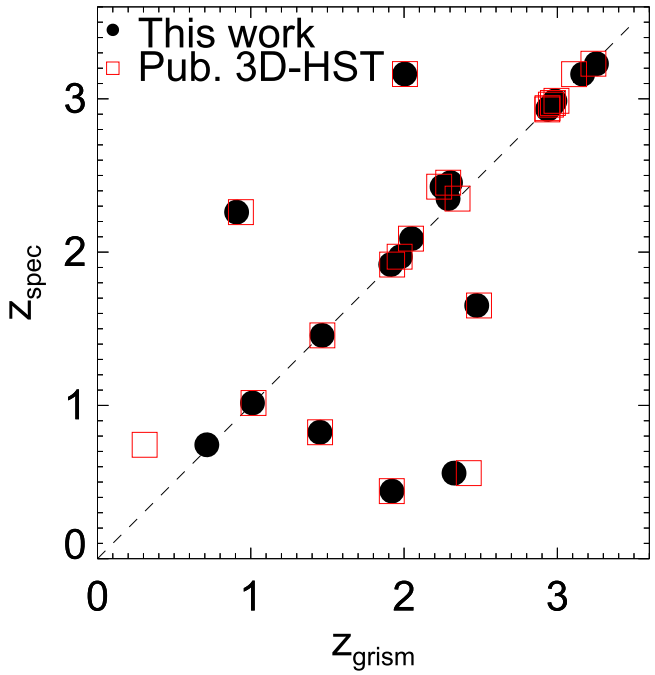

Figure 9. Comparison between grism-based redshifts (black circles show results using the method presented in this work, while red squares show results published in Momcheva et al. 2016) and ground-based spectroscopic redshifts in GOODS-N (as presented in Skelton et al. 2014). There is overall good agreement between the two grism-based methods; some disagreements exist with the published spectroscopic redshifts, but we note that those redshifts are sometimes inaccurate, as shown in Figure 10.

The redshifts at which this work is most efficient, particularly at $1.1 \lesssim z \lesssim 2.3$ when [O III] is visible in the G141 grism, are generally difficult to confirm from the ground at optical wavelengths. Comparison to a small subset of objects that have both grism redshifts and ground-based spectroscopic redshifts shows this difficulty. Further independent verification of the grism-derived redshifts would require additional observations at near-infrared wavelengths. While large samples of such redshifts are currently being obtained, the multiplexing capabilities of slitless grism spectroscopy using WFC3 are difficult to match.

5.2. Stacked Spectra

We need to determine the fraction of objects in this third category that we can positively identify as Hα or [O III] emitters, since uncertain or missing photometry can cause problems in the photometric redshift fitting and cannot be properly taken into account as part of our selection function. Namely, the selection function only contains information from the near-IR imaging, whereas the full galaxy SED is used in the photometric redshift fitting. While we cannot reliably provide line identifications for individual objects in this category, we can determine the relative numbers of Hα and [O III] emitters by comparing spectral stacks with that of known objects.

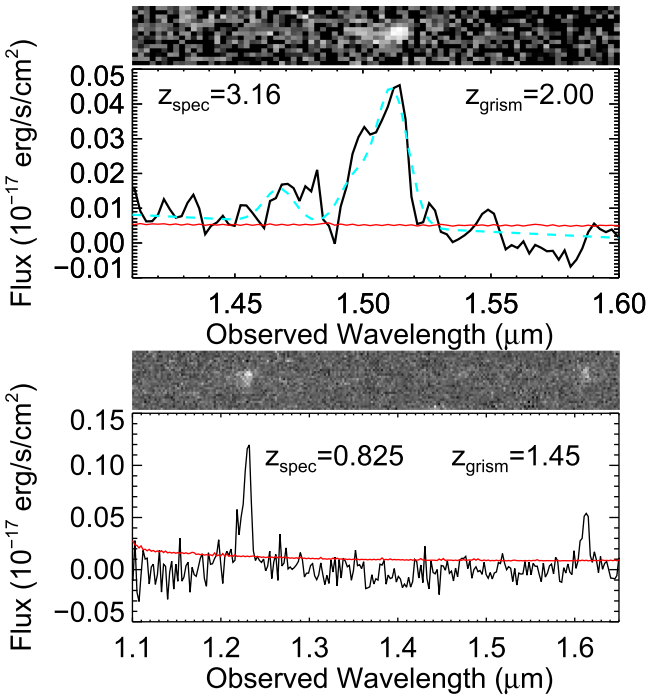

Figure 10. Example 3D-*HST* grism spectra for objects with a disagreement between $z_{\rm spec}$ and $z_{\rm grism}$. The lower panels show 1D spectra, where black lines are the measured spectral fluxes and red lines are the 1-σ errors on the fluxes. The upper panels show the 2D grism spectra. (Top) GOODS-N-13286, showing an emission line at $\sim$1.51 μm. The published $z_{\rm spec}$ value of 3.16 does not predict an emission line at this position. We believe this is a clear case of [O III] and Hβ emission due to the clear asymmetry in the bright line (the unresolved [O III] doublet): the cyan curve shows the best-fit [O III]+Hβ model. (Bottom) GOODS-N-07243, showing clear emission lines at $\sim$1.23 and $\sim$1.61 μm. The published $z_{\rm spec}$ value of 0.825 does not predict emission lines at these locations, which are consistent with [O III] and Hα at $z = 1.45$. In both cases, we suggest that the published spectroscopic redshifts are incorrect.

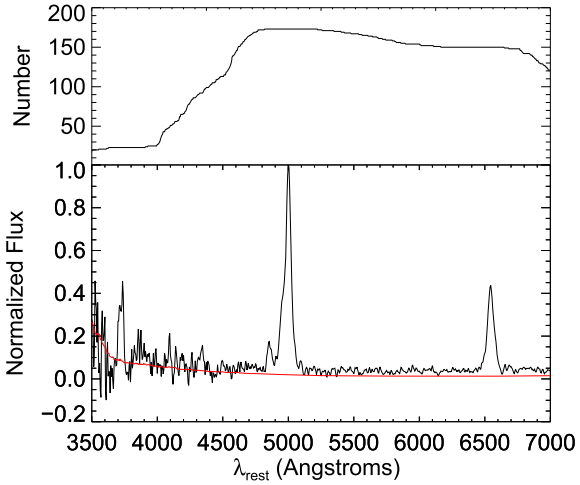

Figure 11. Spectral stack for only the objects with known redshifts due to multiple line detections that hence have an unambiguous (photometric) redshift identification, normalized to the [O III] flux. The upper panel shows the number of unique spectra contributing to the stack at a given wavelength.

Table 2
Stacked Line Ratios

Lines	Ratio
[O III]/Hα	2.03 $\pm$ 0.0327
[O III]/[O II]	3.50 $\pm$ 0.353
[O III]/Hβ	9.50 $\pm$ 0.798

Note. [O III] denotes the single λ5007 component. These ratios are the means for the sample as measured where we have spectral coverage of both lines ($1.15 \lesssim z \lesssim 1.59$ for [O III]/Hα, $1.88 \lesssim z \lesssim 2.40$ for [O III]/[O II], and $1.21 \lesssim z \lesssim 2.40$ for [O III]/Hβ).

From high-EW objects with unambiguous redshifts from multiple significant line detections, we would like to determine the typical line ratios. These ratios are useful to define a flux/EW cut to isolate the same "extreme" objects, as well as to constrain the relative number of the "unknown" objects that are respectively [O III] and Hα.

To do this, we create a stack of all objects in the first class alone (multiple significant line detections) with restframe $\rm EW_{H\alpha}$ or $\rm EW_{[O\,III]}$ in excess of 500 Å, shown in Figure 11. The stacking is done using boxcar extractions of each spectrum in the dispersion direction and weighted according to the grism noise map of the same region. We consider this spectrum as a template EELG, with line ratios that should be representative of the class. These objects alone are used since we are primarily interested in the ratio of [O III] to Hα and to [O II] and hence need a sample containing objects with multiple lines. The relative line ratios are shown in Table 2.

We use these line ratios to construct an equivalent width limit for the sample. We define "high-EW" as having restframe [O III]λ5007 equivalent width in excess of 500 Å. According to the line ratios shown in Table 2 and a continuum slope $F_\lambda \propto \lambda^{-2}$ (van der Wel et al. 2011), this implies a restframe Hα equivalent width limit of 424 Å.

We can then create a similar weighted-mean stack, normalized to the peak line flux, for all 505 of the objects in the third category (single line detections that do not have secure identifications and redshifts), shown in Figure 12. Here, we put the detected emission lines at the same wavelength and apply an observed frame equivalent width limit of 1250 Å (equivalent to a restframe EW of 500 Å at $z = 1.5$). We now use this stack to estimate the fraction of [O III] emitters in this stack by correcting the observed ratio of the peak flux (assuming the line is [O III] λ5007) to the flux at the expected position of Hβ according to the intrinsic ratio from the stack of secure objects. We do not expect any emission line contribution at this spectral position if the primary line is Hα or [O II]. The observed ratio of [O III] to Hβ is 13.3 $\pm$ 1.92, consistent with the observed value within 2-σ. Likewise, we can perform the same exercise with the λ4959 peak of [O III], compared to λ5007. This result is 0.50 $\pm$ 0.034 of the expected 3:1 ratio of λ5007 to λ4959. We note that uncertainties in the object centering due to the low spectral resolution and variations in the emission line morphology can reduce the measured 4959-to-5007 ratio, implying that this 50% could still be a lower limit.

If the primary peak corresponded to Hα, the same test is somewhat more difficult, given that we do not expect to see any other strong emission lines from $0.6 \lesssim z \lesssim 1.1$. While He I and [S III] are covered to varying degrees in this redshift range, they are typically not strong enough to confirm Hα in the absence of other information. If we assume the lines are Hα, we do not detect any feature at the expected wavelength of [O III], placing a 3-σ upper-limit on the [O III]/Hα ratio of 0.02. Compared to the [O III]/Hα ratio from the stack of the objects with secure redshifts, we can conclude that less than 1% of the objects in

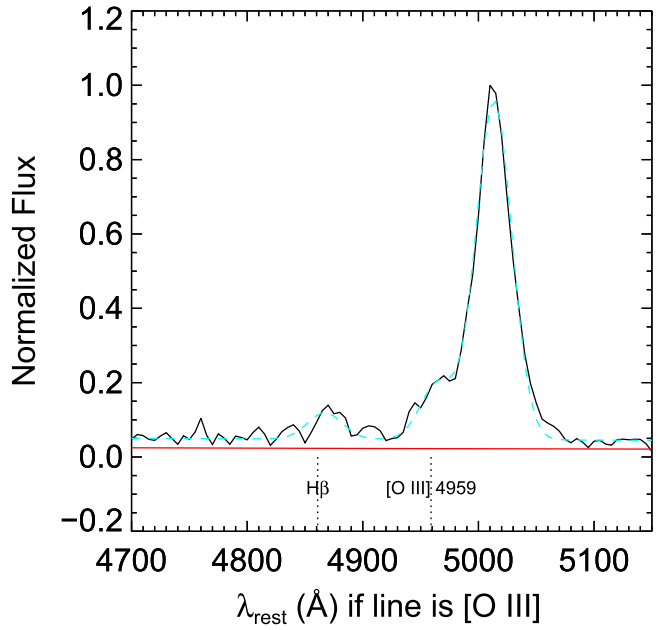

Figure 12. Spectral stack for 505 objects with indeterminate redshifts due to single line detections without an unambiguous photometric redshift identification, normalized to the peak line flux. The *x*-axis shows the wavelengths if the identified emission line is [O III], with the cyan curve showing a Gaussian fit to both [O III] components and Hβ, and the red curve showing the combined 1σ noise of the stack. The additional unfit flux blueward of the central line peak can be attributed to [O III]λ4959 if the line is truly [O III]λ5007. The observed ratio of [O III] to Hβ is 140% of the value we would expect if all objects were [O III] emitters. As we do not observe a significant detection at the expected position of other lines if the peak is Hα, we conclude that the majority of these "unknown" objects are actually [O III] emitters.

Table 3
MCMC Results

Line	Parameter	Value	Uncertainty
[O III]	α	1.88	$^{+0.0376}_{-0.0414}$
	β	0.0600	$^{+0.296}_{-0.299}$
	log ϕ (Mpc^{-3})	−2.36	$^{+0.0326}_{-0.0434}$
Hα	α	1.98	$^{+0.0482}_{-0.0608}$
	β	3.25	$^{+0.522}_{-0.426}$
	log ϕ (Mpc^{-3})	−3.17	$^{+0.0333}_{-0.0406}$

Note. Values are the median of the distributions shown in Figure 13 for $L_0 = 10^{42}$ erg s^{-1} and $z_{0,\mathrm{H}\alpha} = 1.23$ and $z_{0,[\mathrm{O\,III}]} = 1.67$. The uncertainties are the shortest 68% confidence intervals from these same histograms. The quoted comoving number density ϕ is simply N (the intrinsic number of objects in the field) divided by the volume of the survey in cubic Mpc ($\sim 2.7 \times 10^6$ for [O III] and $\sim 1.7 \times 10^6$ for Hα).

this sample are Hα emitters. Note that the expected positions of the [S II] lines ($\lambda\lambda$6717, 6731) are 5126 and 5137 Å on the wavelength scale of Figure 12 and are not clearly detected, further implying that a significant fraction of these emission lines are not Hα.

Therefore, our stacked spectra imply that the majority of these objects are [O III] emitters. We subsequently include these objects as such in the primary sample, putting them at their [O III] redshift and utilizing the [O III] equivalent width selection criteria.

As such, we have 470 "unknown" objects with single emission lines satisfying the [O III] selection criteria, which we include with the primary [O III] sample of 442 for a total of 912. Since we can only make the statistical statement that most of these are [O III] emitters, we must assume that the density estimates for [O III] emitters in the next section are slightly overestimated.

5.3. Number Density Evolution

To estimate for the evolution in the number density of such high-EW objects, we first need to construct a parameterized functional form. For simplicity, we assume a power-law distribution in line luminosities and a power-law dependence in $(1 + z)$. This functional form, for luminosities in the range $L,\ L + dL$ and redshifts in the range $z,\ z + dz$, is

$$\Phi(L, z|\alpha, \beta) = \left(\frac{L}{L_0}\right)^{-\alpha}\left(\frac{1+z}{1+z_0}\right)^{\beta}, \quad (6)$$

where L_0 and z_0 are fiducial values, here taken to be the median of the [O III] and Hα luminosities ($L_0 = 10^{42}$ erg s^{-1}) and the median redshift for the two emission lines ($z_{0,\mathrm{H}\alpha} = 1.23$ and $z_{0,[\mathrm{O\,III}]} = 1.67$). Details of the calculations are given in Appendix B, but in general we can obtain estimates for α and β as well as the intrinsic number density of sources in our survey volume, ϕ (the normalization; i.e., the total number density of sources that could be observed taking into account the incompleteness per unit volume; see Appendix B), per comoving volume element of the survey using a standard Markov Chain Monte Carlo algorithm. We incorporate the knowledge of our selection function (a numerical combination of the completeness functions described in Sections 4.1 and 4.4 and shown in Figure 7, expressed in terms of line luminosity and redshift) as well. Results of this analysis are shown in Figure 13 and in Table 3.

After calculating the respective volumes of the survey given the observed area of 723.3 square arcminutes, we can estimate the comoving number density of high-EW [O III] and Hα emitters. These results are shown in Figure 14 at a fiducial luminosity of $10^{41.5}$ erg s^{-1}. We clearly observe a decrease of the comoving number density toward the present epoch from our 3D-*HST* sample. Although the distribution for the redshift evolution β for the Hα sample is wide, the value of ϕ is well-constrained from the MCMC analysis, and hence the overall uncertainty in the number density evolution, shown by the dashed black lines in Figure 14, is only about 0.1 dex at the low-redshift end. In general, the individual distributions of β in for Hα and [O III] in Figure 13 are consistent with a value greater than zero, implying a secure positive evolution in the comoving number density of high-EW objects. Across the redshift range probed in this study, this evolution is on the order of $\sim$0.8 dex. Note that this analysis neglects the impact of large-scale clustering, which is expected to be moderate for low-mass systems (Boerner et al. 1989). Likewise, many authors fit line luminosity functions as Schechter functions, which also include an exponential cutoff at high luminosities. Since we do not a priori know the luminosity function shape at high-EW, we choose the simpler case of a pure power law (see the $0.9 < z < 1.5$ [O II] sample from Pirzkal et al. 2013). The narrow distributions for α in both the Hα and [O III] samples presented here justify this choice.

Ideally we would have low-redshift samples selected in the same manner as our higher-redshift 3D-*HST* sample; unfortunately

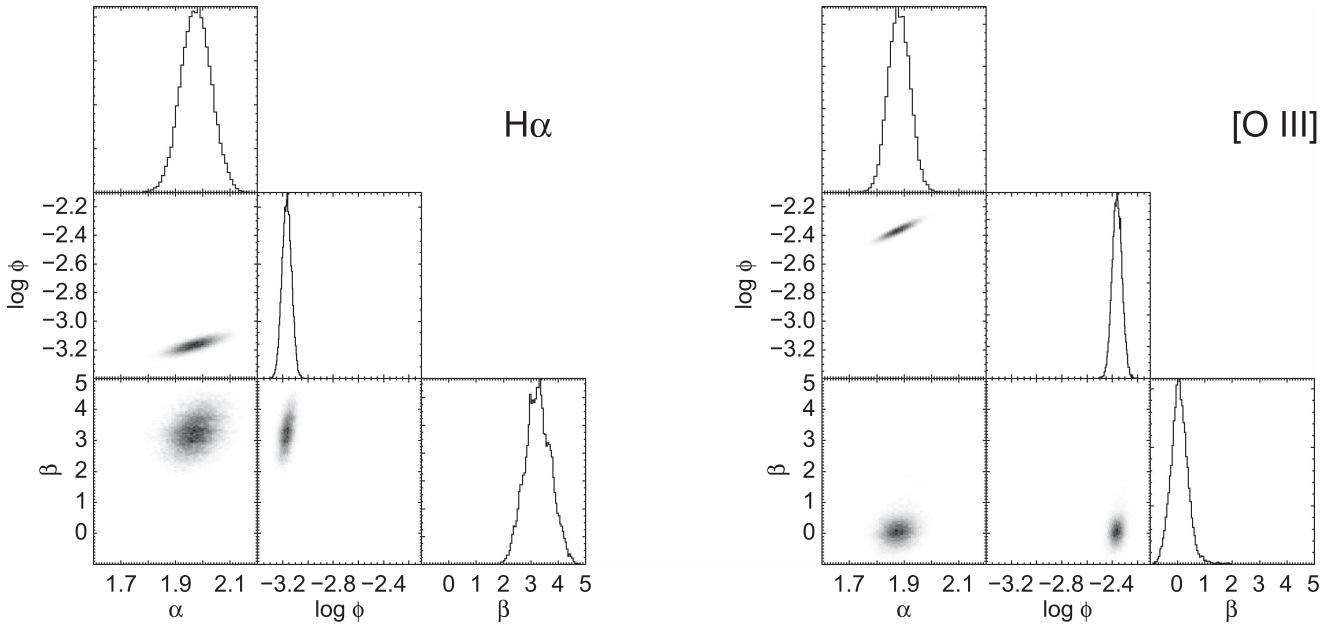

Figure 13. Posterior probability distributions of the parameters α and β from Equation (6), as well as the comoving number density ϕ for the Hα and [O III] samples.

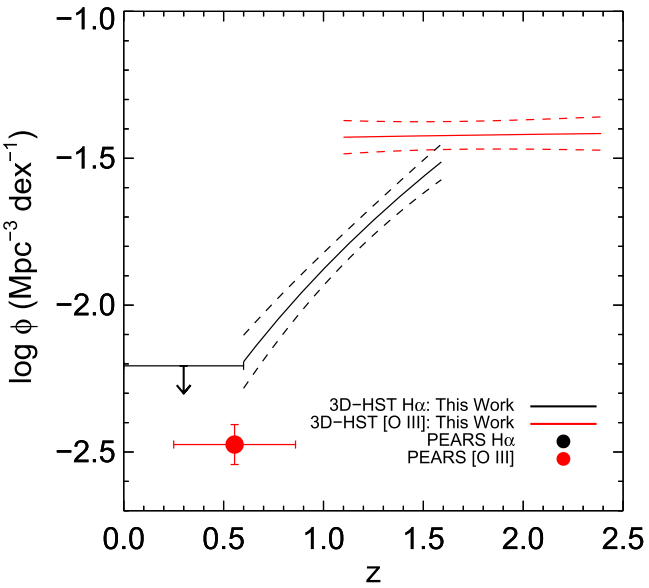

Figure 14. Comoving number densities per dex in luminosity, compared at $L = 10^{41.5}$ erg s^{-1}, as a function of redshift for objects with restframe [O III] (red) and/or Hα (black) EWs in excess of 424/500 Å from *PEARS* (Pirzkal et al. 2013) and this study. The dashed lines represent the ±1-σ uncertainties in the number densities from the width of the MCMC probability distributions for β and N. Error bars in redshift represent the actual redshift range in each bin and not uncertainties in the redshift determination. As the Hα density from *PEARS* is not well-constrained, the upper-limit is plotted.

existing large spectroscopic samples of EELGs, such as those of Amorín et al. (2014a, 2014b), are incomplete and do not have well-defined selection functions. For comparison, we use the results from *PEARS* (Pirzkal et al. 2013) with the same equivalent width limits applied to Hα and [O III] as in the 3D-*HST* sample. While the *PEARS* sample is also derived from grism data, the luminosity limits are sufficiently different from the 3D-*HST* limits presented here, so it is difficult to make a meaningful comparison on an equivalent width-selected sample. Namely, *PEARS* becomes incomplete at luminosities of $10^{41.5}$ erg s^{-1} for [O III] and Hα. In their main sample, there are 6 Hα lines and 25 [O III] lines that meet our EW limits with a quoted quality value greater than 2.5. In order to estimate the number density of these objects, we must correct the counts for (flux) incompleteness using their published completeness curves. As both samples are small, we expect Poisson errors in the number counts to dominate the errors, and hence we do not attempt to perform the same MCMC analysis with all parameters free. Instead, we fix β to zero and adopt the α value for Hα from the 3D-*HST* data, fitting only for the normalization. Figure 14 shows consistency between the [O III] emitters from PEARS and the Hα emitters from this work, given that we do not fit the PEARS sample with a redshift evolution. In the case of Hα, the sample is so small that the result is not well-constrained and we only plot the upper-limit. If we extrapolate our measured Hα number density evolution down to the redshifts of the PEARS Hα sample and take into account the different survey volumes for these respective redshift ranges (3D-*HST* = 56 × PEARS), then we would predict five high-EW Hα emitters at $L = L_0$, based on the number counts from 3D-*HST*, modulo differences in the completeness functions for the two surveys. This expectation value is consistent with the measured counts from the PEARS survey.

We therefore deduce that there is a positive evolution in the number of high-EW objects with redshift, out until at least $z \sim 2.4$.

6. Summary

We present here a new method for detecting emission lines in slitless spectroscopic data. We estimate the likelihood that a given position in the 2D spectrum contains an emission line by cross correlating the position with a kernel corresponding to the

direct image and transform this into the probability that the position corresponds to an emission feature. This method simultaneously includes prior information on line positions from photometric redshift estimates, which also allow us to determine the redshift of the galaxy even when only a single line is detected. The photometric redshifts are determined using a set of galaxy templates that are appropriate for high-EW objects, which are otherwise poorly fit. Robust tests of the method using real and simulated data reveal low levels of contamination and yield a well-defined selection function, which depends on the continuum magnitude of the source as well as the emission line wavelength and flux.

Applying this method to the full 3D-*HST* data set, we obtain a sample of 22,786 galaxies with definite redshifts, either from multiple line detections or single line detections combined with photometric redshift information. The median line flux of the confirmed objects is 2.7×10^{-17} erg s^{-1} cm^{-2}. This method can be considered complimentary to the one presented in Momcheva et al. (2016), given the relative differences in the complexities of the methods and their abilities to find emission lines in different regimes of continuum strength. These redshifts will be included in a future 3D-*HST* data release.

Of this sample, we have 782 high-EW [O III] and/or Hα emitters, where the EW limits are 500 and 424 Å, respectively, due to an intrinsic flux difference between the two species in these objects. Many objects in the survey have detected emission lines but either have a very poorly constrained photometric redshift (i.e., a very high reduced-χ^2 value) or no photometric redshift at all (i.e., it was not detected in enough photometric bands to be fit). A stacked spectrum for these objects reveal that a majority of them are plausibly [O III] emitters based on the observed [O III]/Hβ line ratio in the stack, and we thus include an additional 470 objects into the [O III] sample. We therefore have a sample of 912 high-EW [O III] emitters and 340 Hα emitters.

We parameterize the number density evolution function, assumed to be a power law in both luminosity and redshift, and probe the posterior probability distributions using a Markov Chain Monte Carlo algorithm. Our sample shows an increase in the number of these objects with redshift by a factor of 6 from $z \sim 0.6$–2.4. These results strongly suggest a factor of 30 or more evolution between $z \sim 2$ and present, even though direct comparisons with lower-redshift studies are difficult due to their small volumes and different line luminosity limits.

The observed positive trend in number density with redshift is implied by previous EELG studies, such as Kakazu et al. (2007) and van der Wel et al. (2011), who estimate that [O III] EW $\gtrsim$ 500 Å galaxies are two orders of magnitude more common at $z \sim 1.7$ than at $z = 0$, which is in rough agreement with the results found here. Similarly, Maseda et al. (2014) argue that their results, combined with precise alignments of the two strong galaxy-galaxy lensing systems discovered in CANDELS/3D-*HST* (Brammer et al. 2012a; van der Wel et al. 2013), show that EELGs must be common at $z > 1$. At even higher redshifts, galaxies with these extreme emission line EWs are abundant and perhaps even ubiquitous (at $z > 6$; e.g., Smit et al. 2014).

This method, while specifically applied to *HST* grism spectroscopy, is more generally applicable to any spectroscopy with spatial as well as spectral information. Its automated nature can be utilized to construct samples of emission line galaxies in large surveys, and it can also be used to determine the significance of an emission line "detection" for individual objects. Planned future grism surveys, such as *Euclid* and *WFIRST*, will require an automated line search to analyze the huge volume of data produced. Grisms also feature prominently on the *James Webb Space Telescope*, with both *NIRISS* and *NIRCam* providing multiple slitless grism spectroscopic modes. Given the variety of photometry that will likely be obtained in parallel, a method such as this one that can combine the spectroscopic and photometric information in a statistical way will be a powerful tool in making the best use of future *JWST* slitless grism spectroscopic surveys.

We would like to thank Greg Rudnick, Fabian Walter, and David Hogg for interesting discussions about statistics. We would also like to thank Pieter van Dokkum and the rest of the 3D-*HST* collaboration for their work on the survey and input at various stages of this project. M.V.M. was a member of the International Max Planck Research School for Astronomy and Cosmic Physics at the University of Heidelberg, IMPRS-HD, Germany. B.F.L. acknowledges support from the NSF Astronomy and Astrophysics Fellowship grant AST-1202963.

Facility: HST.

Appendix A
Fidelity of Photometric Searches

The photometric selection technique of van der Wel et al. (2011) utilizes the I_{F814W}-, J_{F125W}-, and H_{F160W}-bands to preferentially select systems dominated by strong emission lines. By looking for a flux excess in J compared to the continuum as measured in I and H, they claim to select [O III] emitters at $1.6 < z < 1.8$, with perhaps minor contamination by Hα emitters at $z \sim 1$.

As we now have more complete photometry from 3D-*HST* and CANDELS since the study of van der Wel et al. (2011), we can apply the same photometric cuts to a larger sample. Previously, van der Wel et al. (2011) found 69 objects in 279 arcmin^2. Here, using the same cuts, we discover 312 objects in the full 896 arcmin^2 of the 3D-*HST* survey: 94 in AEGIS, 48 in COSMOS, 67 in GOODS-N (using the F775W filter in place of the F814W filter), 51 in GOODS-S, and 52 in UDS.

We compare this photometric sample with our spectroscopic sample to test the fidelity of the photometric search. For the following analysis, we ignore objects whenever severe contamination would prevent a line identification and objects without full spectral coverage bluewards of 14000 Å: we are left then with a total of 186 objects, of which 147 (79%) have a strong emission line in the J-band. Many of the objects without a detected emission line are intrinsically faint, and thus their emission line could simply be fainter than the noise level in the grism frames. We thus verify the *iJH*-selection as an efficient way to select emission line galaxies.

Another photometric selection is given in Cardamone et al. (2009) for lower-redshift emission line galaxies, the so-called "green pea" galaxies. While the same selections could yield a sizable sample in our data set, we would not detect the

strongest emission lines (Hα or [O III]) in the NIR for them, given their low redshifts.

Cooke (2009) also developed a selection technique to select emission line galaxies from broadband photometric data, specifically searching for $z \sim 3$ Lyα emitters at optical wavelengths. Of a sample of 17 galaxies that were selected using photometric cuts, 8 (47%) were confirmed to have Lyα emission, even though the average EW of the emission is a factor of $\sim$10 lower than the [O III] emission in the $z \sim 1.7$ EELGs.

Appendix B
Bayesian Luminosity Function

As described in the text, we would like to determine the evolution in the comoving number density of the high-EW emission line sample. This is a simplified case where all redshifts and luminosities are precisely known, as well as the selection function.

We can parameterize the distribution of sources in the range $L,\ L + dL;\ z,\ z + dz$ as the combination of a power law in luminosity and in redshift according to

$$\Phi(L, z|\alpha, \beta) = \left(\frac{L}{L_0}\right)^{-\alpha}\left(\frac{1+z}{1+z_0}\right)^{\beta}, \tag{7}$$

where L_0 and z_0 are fiducial values (the medians of the input observations). The probability density of L and z, then, is

$$P(L, z|\alpha, \beta, \phi_0) = \phi\ \Phi(L, z|\alpha, \beta)\ \frac{dV}{dz}(z), \tag{8}$$

where ϕ is the total number density of sources N/V (Mpc^{-3}) that could be observed, and dV/dz is the comoving volume element of the survey. We can consider ϕ as the (inverse) normalization constant since $\int\int P(L, z)dLdz \equiv 1$, defining $1/\phi_0 = N$.

For the entire sample of N objects, the probability of L and z is simply the product of the individual probabilities:

$$P(L, z|\alpha, \beta, \phi_0) \propto \prod_{i=i}^{N} \frac{1}{N}\frac{dV}{dz}(z_i)\left(\frac{L_i}{L_0}\right)^{-\alpha}\left(\frac{1+z_i}{1+z_0}\right)^{\beta}. \tag{9}$$

However, we do not observe the full sample due to incompleteness in, for example, flux. We do understand our selection function S and have a subsample of n objects; the observations are a binomial process of n drawing from an intrinsic distribution containing N objects. Hence we can write

$$P(N|n, \alpha, \beta) = P(N)C_n^N(P(\text{objects in sample}|\alpha, \beta))^n \times (P(\text{objects not in sample}|\alpha, \beta))^{N-n}, \tag{10}$$

which is equal to

$$P(N|n, \alpha, \beta) = C_{n-1}^{N-1}\left(\int\int S(L, z)P(L, z|\alpha, \beta)dLdz\right)^n \times \left(1 - \int\int S(L, z)P(L, z|\alpha, \beta)dLdz\right)^{N-n}, \tag{11}$$

where n is the number of observations in our sample and we assume a flat prior on $\log N$.

The posterior on the parameters α and β given the observed data set is simply the product of the n observed probabilities:

$$P(\alpha, \beta|\{L_{\rm obs}, z_{\rm obs}\}) = P(\alpha, \beta)\prod_{i=1}^{n} P_{\rm obs}(L_i, z_i|\alpha, \beta) \tag{12}$$

or

$$P(\alpha, \beta|\{L_{\rm obs}, z_{\rm obs}\}) = \prod_{i=1}^{n} \frac{P(L_i, z_i|\alpha, \beta)}{\int\int S(L, z)P(L, z|\alpha, \beta)dLdz}, \tag{13}$$

which simplifies to

$$P(\alpha, \beta|\{L_{\rm obs}, z_{\rm obs}\}) = \left(\int\int S(L, z)P(L, z|\alpha, \beta)dLdz\right)^{-n} \times \prod_{i=1}^{n} P(L_i, z_i|\alpha, \beta). \tag{14}$$

We would like to know the posterior probability of the model parameters given our n observed data points. From Bayes's theorem,

$$P(\alpha, \beta, N|\{L_{\rm obs}, z_{\rm obs}\}) \propto P(N|n, \alpha, \beta) \times P(\alpha, \beta|\{L_{\rm obs}, z_{\rm obs}\}). \tag{15}$$

Since the first term in Equation (14) will cancel with the second term in Equation (11), we obtain a simplified posterior probability of

$$P(\alpha, \beta, N|\{L_{\rm obs}, z_{\rm obs}\}) \propto C_{n-1}^{N-1} \times\left(1 - \int\int \frac{1}{N}\frac{dV}{dz}(z)\Phi(L, z|\alpha, \beta)S(L, z)dLdz\right)^{N-n} \times\prod_{i=1}^{n} P(L_i, z_i|\alpha, \beta). \tag{16}$$

From here, a standard MCMC analysis can determine the distributions for the model parameters.

Appendix C
Table of High-EW [O III] and Hα Emitters

Table 4 lists the confirmed high-EW Hα and/or [O III] emitters and Table 5 lists the plausible high-EW [O III] emitters.

Table 4
High-EW [O III] and Hα Emitters

ID	R.A.	Decl.	$z_{\rm grism}$	Hα Flux	Hα EW	[O III] Flux	[O III] EW
AEGIS-1312	215.10797	52.931831	1.90	⋯	⋯	8.12 ± 0.513	935 ± 142
AEGIS-2157	215.00920	52.866520	1.17	4.71 ± 0.501	1070 ± 246	7.39 ± 2.51	5670 ± 10800
AEGIS-2497	215.01721	52.873791	2.02	⋯	⋯	4.01 ± 0.719	637 ± 233
AEGIS-2633	215.08171	52.919991	1.43	3.19 ± 0.824	1020 ± 605	3.95 ± 1.19	493 ± 228
AEGIS-2686	214.82976	52.741333	1.74	⋯	⋯	5.53 ± 0.535	1970 ± 846
AEGIS-3680	214.82545	52.742840	2.21	⋯	⋯	2.29 ± 0.511	508 ± 221
AEGIS-3894	214.94737	52.830559	1.14	12.0 ± 0.509	2150 ± 415	⋯	⋯
AEGIS-4874	215.09644	52.940517	1.46	1.40 ± 0.373	3070 ± 4410	1.43 ± 0.0921	758 ± 360
AEGIS-4900	214.76906	52.708069	1.39	2.10 ± 0.274	452 ± 119	2.13 ± 0.427	369 ± 111
AEGIS-5000	214.87688	52.785248	1.23	2.44 ± 0.599	174 ± 50.5	8.78 ± 1.25	563 ± 119
AEGIS-6493	214.98486	52.868324	1.88	⋯	⋯	4.44 ± 0.586	847 ± 259
AEGIS-6848	215.05035	52.916252	1.29	3.02 ± 0.445	633 ± 163	1.01 ± 0.0603	216 ± 41.4
AEGIS-7182	214.79866	52.738842	2.01	⋯	⋯	4.66 ± 0.592	606 ± 181
AEGIS-7207	214.81740	52.752342	1.19	2.49 ± 0.584	444 ± 163	6.04 ± 2.19	2050 ± 2050
AEGIS-7222	214.96318	52.856152	1.40	2.30 ± 0.274	787 ± 204	2.80 ± 0.430	347 ± 77.4
AEGIS-7695	215.07890	52.939789	1.25	3.41 ± 0.711	971 ± 423	3.32 ± 0.223	551 ± 106
AEGIS-7997	214.98071	52.871750	1.17	2.87 ± 0.805	443 ± 174	5.98 ± 0.415	1390 ± 364
AEGIS-8302	215.07730	52.940784	0.781	12.0 ± 1.10	806 ± 118	⋯	⋯
AEGIS-8775	214.98763	52.880367	1.47	1.03 ± 0.0139	427 ± 114	5.73 ± 0.984	2270 ± 1490
AEGIS-8811	214.87466	52.800041	1.24	4.94 ± 0.542	417 ± 68.1	8.83 ± 1.12	573 ± 111
AEGIS-8869	214.83560	52.772583	1.57	3.27 ± 0.122	439 ± 48.2	10.0 ± 0.726	657 ± 87.3
AEGIS-9075	214.85789	52.789570	1.23	2.79 ± 0.298	539 ± 102	6.29 ± 0.623	1050 ± 234
AEGIS-9115	214.79759	52.746696	1.15	2.96 ± 0.478	435 ± 104	⋯	⋯
AEGIS-9291	215.07124	52.941769	1.35	1.46 ± 0.325	378 ± 121	3.69 ± 0.558	722 ± 210
AEGIS-9639	214.77678	52.734154	2.17	⋯	⋯	6.24 ± 0.427	772 ± 141
AEGIS-9650	215.06482	52.938808	1.16	3.93 ± 0.499	1230 ± 377	⋯	⋯
AEGIS-9888	215.04428	52.925461	1.33	1.08 ± 0.305	290 ± 107	3.02 ± 0.583	998 ± 442
AEGIS-10259	214.86079	52.796261	1.18	10.7 ± 0.680	661 ± 75.2	⋯	⋯
AEGIS-11312	214.95482	52.868332	0.678	5.21 ± 1.56	6730 ± 11299	⋯	⋯
AEGIS-11888	214.75044	52.724934	2.03	⋯	⋯	5.13 ± 0.400	763 ± 155
AEGIS-13311	214.74451	52.726570	1.39	1.46 ± 0.252	491 ± 154	3.00 ± 0.412	481 ± 114
AEGIS-13545	214.93854	52.865761	1.22	2.53 ± 0.437	1230 ± 516	0.0646 ± 0.0152	22.8 ± 8.22
AEGIS-13884	214.76881	52.746201	1.23	2.75 ± 0.467	256 ± 56.4	8.16 ± 1.01	596 ± 112
AEGIS-14122	214.77609	52.752327	1.26	1.11 ± 0.0237	176 ± 26.6	5.30 ± 1.08	976 ± 375
AEGIS-14217	214.73640	52.724525	1.14	2.67 ± 0.332	2790 ± 2900	⋯	⋯
AEGIS-14711	214.86214	52.815834	1.23	6.48 ± 0.533	349 ± 38.4	15.8 ± 1.10	688 ± 76.9
AEGIS-14821	214.71358	52.710327	1.22	4.09 ± 0.421	231 ± 29.8	11.8 ± 0.936	628 ± 77.7
AEGIS-14921	214.86432	52.818508	1.64	⋯	⋯	4.06 ± 0.350	554 ± 139
AEGIS-15168	214.81459	52.783966	1.31	0.997 ± 0.262	863 ± 493	0.497 ± 0.00677	228 ± 84.7
AEGIS-15233	214.90135	52.846004	1.46	⋯	⋯	2.95 ± 0.364	2480 ± 1930
AEGIS-15543	214.92963	52.867229	1.50	0.576 ± 0.0153	132 ± 32.0	6.45 ± 1.53	1470 ± 979
AEGIS-15987	214.99921	52.918369	1.24	0.239 ± 0.00375	159 ± 54.1	3.17 ± 0.711	3750 ± 4790
AEGIS-16341	215.01637	52.931763	1.25	4.19 ± 0.467	568 ± 107	9.31 ± 0.998	893 ± 179
AEGIS-16488	214.83972	52.807346	1.36	3.28 ± 0.305	1200 ± 306	5.28 ± 0.504	944 ± 231
AEGIS-16564	214.78851	52.771122	1.23	1.66 ± 0.419	1710 ± 1210	1.34 ± 0.0181	1280 ± 858
AEGIS-16941	215.01091	52.930676	1.26	1.93 ± 0.326	504 ± 134	3.28 ± 0.644	594 ± 190
AEGIS-17024	214.98708	52.914066	2.09	⋯	⋯	10.0 ± 0.469	607 ± 57.8
AEGIS-17074	214.71315	52.719231	1.28	1.23 ± 0.306	534 ± 241	1.94 ± 0.569	634 ± 318
AEGIS-18034	214.96558	52.903069	1.45	0.787 ± 0.174	267 ± 86.7	0.897 ± 0.259	732 ± 668
AEGIS-18265	214.85098	52.822655	1.20	2.47 ± 0.303	1060 ± 291	⋯	⋯
AEGIS-19113	214.76064	52.761715	1.37	2.58 ± 0.650	938 ± 525	2.25 ± 0.0595	334 ± 65.2
AEGIS-19790	215.04973	52.969734	1.42	1.89 ± 0.0260	1330 ± 648	6.84 ± 1.40	3250 ± 3140
AEGIS-20187	214.94522	52.897339	1.57	3.20 ± 0.105	1110 ± 318	3.10 ± 0.749	609 ± 280
AEGIS-20293	214.68001	52.708599	1.07	5.42 ± 0.518	1500 ± 424	⋯	⋯
AEGIS-21469	215.04330	52.971664	1.55	2.62 ± 0.646	708 ± 320	3.30 ± 0.764	430 ± 150
AEGIS-22858	214.97955	52.932171	1.40	3.07 ± 0.352	436 ± 83.0	7.00 ± 0.561	558 ± 75.0
AEGIS-22997	214.70302	52.735809	1.82	⋯	⋯	4.13 ± 0.530	592 ± 154
AEGIS-23050	215.03064	52.969044	1.78	⋯	⋯	6.85 ± 0.860	524 ± 109
AEGIS-23700	214.87386	52.860619	1.34	0.852 ± 0.222	561 ± 250	1.22 ± 0.206	2100 ± 2520
AEGIS-23737	214.74921	52.771885	1.40	2.66 ± 0.641	748 ± 355	5.22 ± 0.990	686 ± 231
AEGIS-24361	214.78552	52.799988	1.48	4.04 ± 0.408	658 ± 139	10.7 ± 0.578	969 ± 123
AEGIS-24492	215.00143	52.953899	2.11	⋯	⋯	1.45 ± 0.362	666 ± 332
AEGIS-24687	214.72911	52.760990	1.20	2.26 ± 0.329	1610 ± 874	1.24 ± 0.0236	728 ± 313
AEGIS-24958	214.76779	52.789707	1.17	2.12 ± 0.304	516 ± 117	⋯	⋯
AEGIS-25077	214.82806	52.833149	1.81	⋯	⋯	4.55 ± 0.636	1840000 ± 734000000

Table 4
(Continued)

ID	R.A.	Decl.	$z_{\rm grism}$	Hα Flux	Hα EW	[O III] Flux	[O III] EW
AEGIS-25180	214.92149	52.899986	1.40	1.80 ± 0.456	896 ± 460	2.13 ± 0.563	459 ± 186
AEGIS-25351	214.72325	52.759426	1.91	⋯	⋯	4.13 ± 0.640	1540 ± 1010
AEGIS-25840	214.96841	52.936050	1.91	⋯	⋯	1.04 ± 0.253	557 ± 265
AEGIS-25917	214.69214	52.739319	1.32	1.35 ± 0.160	162 ± 30.9	5.24 ± 1.14	518 ± 172
AEGIS-26011	214.82341	52.833763	0.750	4.24 ± 0.884	689 ± 226	⋯	⋯
AEGIS-26297	214.75540	52.786373	1.47	0.403 ± 0.0285	655 ± 485	0.764 ± 0.185	388 ± 213
AEGIS-26370	214.71875	52.760300	1.44	4.95 ± 0.550	575 ± 123	12.0 ± 0.821	845 ± 120
AEGIS-28611	214.90605	52.902313	1.47	2.47 ± 0.482	285 ± 74.0	9.19 ± 0.700	865 ± 133
AEGIS-29785	214.96523	52.949238	1.23	2.25 ± 0.585	990 ± 538	⋯	⋯
AEGIS-29868	214.96529	52.949398	1.24	⋯	⋯	7.48 ± 0.867	815 ± 176
AEGIS-29967	214.97754	52.958485	1.16	4.11 ± 0.498	572 ± 117	11.6 ± 2.97	4930 ± 6220
AEGIS-31566	214.68716	52.758156	2.31	⋯	⋯	5.23 ± 0.410	512 ± 83.3
AEGIS-32040	214.74860	52.803951	1.85	⋯	⋯	3.21 ± 0.567	911 ± 391
AEGIS-32058	214.77040	52.819122	1.20	2.58 ± 0.682	478 ± 188	8.34 ± 1.97	3050 ± 2640
AEGIS-32094	214.95238	52.949051	1.53	2.42 ± 0.450	659 ± 243	2.63 ± 0.579	269 ± 78.3
AEGIS-32185	214.97789	52.967285	1.39	5.25 ± 0.533	508 ± 80.9	8.98 ± 0.796	479 ± 63.6
AEGIS-32596	214.98651	52.974846	1.57	6.84 ± 1.09	2150 ± 1310	5.77 ± 0.891	406 ± 91.5
AEGIS-32822	214.66818	52.748898	1.37	5.17 ± 0.581	298 ± 48.7	15.6 ± 0.963	540 ± 53.8
AEGIS-33367	214.75905	52.816193	1.30	4.71 ± 0.725	480 ± 111	1.80 ± 0.0661	126 ± 9.82
AEGIS-33448	214.82669	52.865208	1.05	4.68 ± 0.900	1180 ± 545	⋯	⋯
AEGIS-33805	214.84558	52.879910	1.54	1.93 ± 0.189	291 ± 47.3	4.82 ± 0.638	537 ± 117
AEGIS-33957	214.95328	52.956917	1.51	3.21 ± 0.806	448 ± 169	7.67 ± 1.06	732 ± 183
AEGIS-33993	214.94792	52.953083	1.50	4.18 ± 0.675	571 ± 172	0.0435 ± 0.0192	5.98 ± 2.82
AEGIS-34683	214.83994	52.879478	1.53	1.56 ± 0.261	348 ± 91.3	3.99 ± 0.659	698 ± 215
AEGIS-35159	214.92696	52.942932	1.41	4.47 ± 0.505	1020 ± 258	1.13 ± 0.0398	144 ± 16.8
AEGIS-36205	214.67642	52.768612	2.39	⋯	⋯	16.0 ± 2.58	866 ± 301
AEGIS-36383	214.80411	52.860836	1.23	2.25 ± 0.450	246 ± 60.9	9.63 ± 0.931	1450 ± 344
AEGIS-36608	214.72124	52.802738	2.14	⋯	⋯	5.08 ± 0.403	941 ± 222
AEGIS-37675	214.84850	52.897629	1.24	2.30 ± 0.445	517 ± 163	3.21 ± 0.933	1370 ± 945
AEGIS-38115	214.65778	52.762886	0.721	9.53 ± 1.34	535 ± 102	⋯	⋯
AEGIS-38808	214.91620	52.949707	1.18	2.65 ± 0.378	1140 ± 404	⋯	⋯
AEGIS-39004	214.82455	52.885426	1.40	1.29 ± 0.0187	334 ± 65.6	5.37 ± 1.30	1460 ± 910
AEGIS-40606	214.82756	52.896812	1.82	⋯	⋯	6.57 ± 0.514	1760 ± 731
COSMOS-2135	150.10744	2.2007082	0.889	6.46 ± 1.48	1860 ± 1120	⋯	⋯
COSMOS-2200	150.10893	2.2013004	1.88	⋯	⋯	3.05 ± 0.644	1080 ± 596
COSMOS-2945	150.07848	2.2084236	2.16	⋯	⋯	2.61 ± 0.460	1700 ± 1040
COSMOS-3134	150.12135	2.2103746	0.767	3.68 ± 0.503	2470 ± 1790	⋯	⋯
COSMOS-3256	150.15916	2.2114725	1.23	2.09 ± 0.745	195 ± 84.9	6.87 ± 1.60	577 ± 208
COSMOS-3497	150.11224	2.2136466	1.87	⋯	⋯	6.12 ± 0.766	994 ± 311
COSMOS-3518	150.11235	2.2137351	1.90	⋯	⋯	9.07 ± 1.68	1380 ± 741
COSMOS-3529	150.08028	2.2139792	1.89	⋯	⋯	5.91 ± 0.778	1070 ± 343
COSMOS-3545	150.17690	2.2140050	0.983	2.70 ± 0.678	989 ± 517	⋯	⋯
COSMOS-3568	150.17159	2.2142694	1.86	⋯	⋯	5.97 ± 1.23	3560 ± 4350
COSMOS-3746	150.07547	2.2158711	1.22	⋯	⋯	10.0 ± 2.29	11600 ± 27799
COSMOS-3783	150.18625	2.2161422	1.82	⋯	⋯	4.57 ± 0.498	1270 ± 411
COSMOS-3818	150.18697	2.2164545	1.23	3.35 ± 0.820	721 ± 349	5.67 ± 1.34	1460 ± 855
COSMOS-4099	150.14835	2.2189941	2.33	⋯	⋯	2.20 ± 0.596	683 ± 394
COSMOS-4115	150.06847	2.2193368	1.92	⋯	⋯	4.79 ± 1.08	1530 ± 1030
COSMOS-4205	150.13994	2.2202120	1.84	⋯	⋯	14.1 ± 0.680	692 ± 71.3
COSMOS-4507	150.07137	2.2232266	1.72	⋯	⋯	3.89 ± 1.04	830 ± 524
COSMOS-4524	150.15224	2.2236185	1.83	⋯	⋯	12.4 ± 0.919	877 ± 155
COSMOS-4556	150.09294	2.2236500	2.02	⋯	⋯	5.31 ± 0.693	1840 ± 816
COSMOS-4672	150.08124	2.2249193	1.23	3.94 ± 0.631	650 ± 177	0.183 ± 0.0255	23.6 ± 4.51
COSMOS-5956	150.08717	2.2382691	0.828	1.19 ± 0.331	598 ± 344	⋯	⋯
COSMOS-6011	150.18889	2.2393849	2.03	⋯	⋯	5.99 ± 0.491	575 ± 95.1
COSMOS-6232	150.10603	2.2410550	2.16	⋯	⋯	9.40 ± 0.750	980 ± 226
COSMOS-6367	150.12151	2.2425027	2.24	⋯	⋯	1.79 ± 0.395	799 ± 409
COSMOS-6623	150.17624	2.2452819	2.02	⋯	⋯	3.44 ± 0.496	775 ± 266
COSMOS-6632	150.09747	2.2454619	1.46	3.74 ± 0.531	266 ± 48.4	10.3 ± 0.802	526 ± 63.3
COSMOS-7333	150.16078	2.2529967	1.84	⋯	⋯	2.35 ± 0.628	666 ± 369
COSMOS-7404	150.14490	2.2541955	1.31	6.04 ± 1.51	705 ± 321	5.08 ± 0.127	384 ± 48.9
COSMOS-7491	150.15977	2.2549064	0.761	4.26 ± 1.24	11299 ± 35800	⋯	⋯
COSMOS-7509	150.09680	2.2551012	1.86	⋯	⋯	3.94 ± 0.992	1430 ± 1100
COSMOS-7668	150.18517	2.2569325	0.970	2.24 ± 0.632	842 ± 461	⋯	⋯
COSMOS-7694	150.14656	2.2573443	1.44	1.54 ± 0.324	597 ± 219	2.29 ± 0.485	720 ± 326

Table 4
(Continued)

ID	R.A.	Decl.	$z_{\rm grism}$	Hα Flux	Hα EW	[O III] Flux	[O III] EW
COSMOS-7695	150.18262	2.2573502	0.843	2.20 ± 0.548	1090 ± 612	⋯	⋯
COSMOS-7879	150.09261	2.2598045	1.27	3.15 ± 0.840	346 ± 124	8.01 ± 1.55	597 ± 177
COSMOS-8057	150.09709	2.2615211	1.50	1.49 ± 0.425	493 ± 238	0.466 ± 0.0172	51.3 ± 5.53
COSMOS-8072	150.19272	2.2615883	2.09	⋯	⋯	2.22 ± 0.587	2900 ± 4420
COSMOS-8169	150.08434	2.2625942	2.19	⋯	⋯	3.79 ± 0.860	1010 ± 555
COSMOS-8244	150.18437	2.2634900	1.17	4.08 ± 0.732	1230 ± 548	⋯	⋯
COSMOS-8290	150.06812	2.2639935	1.82	⋯	⋯	1.75 ± 0.479	1180 ± 909
COSMOS-8374	150.17148	2.2645972	0.746	5.50 ± 1.56	2490 ± 2130	⋯	⋯
COSMOS-8383	150.18721	2.2647901	2.09	⋯	⋯	9.29 ± 0.501	590 ± 63.9
COSMOS-8463	150.15570	2.2654181	1.30	2.60 ± 0.597	630 ± 264	⋯	⋯
COSMOS-8577	150.17534	2.2663887	1.23	1.71 ± 0.453	544 ± 238	0.598 ± 0.0142	131 ± 30.0
COSMOS-8616	150.19496	2.2670042	1.40	2.38 ± 0.591	292 ± 98.9	9.44 ± 0.887	736 ± 128
COSMOS-8645	150.11336	2.2675264	1.17	9.23 ± 1.25	486 ± 97.9	7.44 ± 1.41	354 ± 88.0
COSMOS-8673	150.08836	2.2674656	1.86	⋯	⋯	4.49 ± 0.878	1240 ± 713
COSMOS-8758	150.10434	2.2683890	1.22	1.10 ± 0.0594	149 ± 24.3	6.11 ± 1.24	997 ± 400
COSMOS-8920	150.11943	2.2697804	1.23	2.09 ± 0.552	1110 ± 801	⋯	⋯
COSMOS-8996	150.11273	2.2706454	2.23	⋯	⋯	1.95 ± 0.486	1260 ± 982
COSMOS-9316	150.17102	2.2743361	1.42	5.23 ± 0.921	242 ± 54.6	12.9 ± 1.39	510 ± 84.6
COSMOS-9537	150.16751	2.2763560	1.80	⋯	⋯	4.03 ± 0.645	883 ± 414
COSMOS-9556	150.09009	2.2765446	1.14	2.54 ± 0.553	2240 ± 1700	⋯	⋯
COSMOS-9569	150.17285	2.2766931	1.81	⋯	⋯	9.34 ± 0.562	1330 ± 304
COSMOS-10030	150.10364	2.2816844	0.680	4.60 ± 1.39	2190 ± 1710	⋯	⋯
COSMOS-10807	150.08727	2.2896297	1.86	⋯	⋯	12.6 ± 0.795	975 ± 158
COSMOS-10808	150.15945	2.2899418	0.754	11.1 ± 1.13	473 ± 64.8	⋯	⋯
COSMOS-11091	150.05618	2.2923021	1.19	4.47 ± 0.687	524 ± 121	7.34 ± 2.75	869 ± 550
COSMOS-11458	150.13809	2.2957556	2.20	⋯	⋯	2.39 ± 0.410	1140 ± 694
COSMOS-11546	150.11226	2.2968461	1.20	3.20 ± 0.703	349 ± 104	8.97 ± 2.25	1150 ± 562
COSMOS-11628	150.16013	2.2975037	1.06	2.88 ± 0.586	1190 ± 598	⋯	⋯
COSMOS-11698	150.10307	2.2981279	1.26	3.01 ± 0.747	944 ± 490	1.19 ± 0.0412	127 ± 17.5
COSMOS-11703	150.16243	2.2981818	1.95	⋯	⋯	3.37 ± 0.739	774 ± 389
COSMOS-12088	150.19534	2.3017480	1.50	0.820 ± 0.0229	212 ± 28.0	3.98 ± 0.541	641 ± 170
COSMOS-12308	150.13826	2.3041039	2.19	⋯	⋯	2.15 ± 0.528	597 ± 277
COSMOS-12408	150.12053	2.3049338	1.54	2.58 ± 0.595	634 ± 254	2.14 ± 0.729	183 ± 74.5
COSMOS-12454	150.09680	2.3053823	2.01	⋯	⋯	2.05 ± 0.558	833 ± 529
COSMOS-12770	150.16336	2.3086884	1.18	2.26 ± 0.541	248 ± 73.1	7.24 ± 2.11	1760 ± 1260
COSMOS-12924	150.13911	2.3106835	1.42	3.12 ± 0.808	614 ± 269	⋯	⋯
COSMOS-13767	150.16084	2.3190613	1.47	1.95 ± 0.0528	424 ± 60.1	4.09 ± 0.929	512 ± 179
COSMOS-13832	150.08900	2.3199255	1.79	⋯	⋯	8.72 ± 0.815	520 ± 85.7
COSMOS-13844	150.11563	2.3198395	1.25	2.21 ± 0.413	9870 ± 25099	1.47 ± 0.0247	595 ± 211
COSMOS-13874	150.18930	2.3201780	1.36	3.40 ± 0.893	1050 ± 620	2.81 ± 0.0303	428 ± 98.0
COSMOS-13896	150.16360	2.3204167	1.34	1.88 ± 0.485	303 ± 103	4.84 ± 0.867	528 ± 143
COSMOS-13900	150.11673	2.3204768	1.01	6.11 ± 1.27	869 ± 343	⋯	⋯
COSMOS-14063	150.08963	2.3221247	0.738	6.61 ± 0.788	818 ± 166	⋯	⋯
COSMOS-14491	150.16289	2.3267648	1.91	⋯	⋯	1.64 ± 0.451	1460 ± 1320
COSMOS-14534	150.15958	2.3273230	2.05	⋯	⋯	4.09 ± 0.728	794 ± 297
COSMOS-14880	150.15112	2.3310845	2.06	⋯	⋯	4.93 ± 0.484	674 ± 169
COSMOS-15098	150.09506	2.3334012	2.08	⋯	⋯	3.03 ± 0.642	2350 ± 2190
COSMOS-15451	150.18127	2.3372550	1.24	2.40 ± 0.409	415 ± 103	6.09 ± 0.824	630 ± 140
COSMOS-15844	150.06555	2.3411415	1.98	⋯	⋯	7.99 ± 0.629	687 ± 112
COSMOS-15994	150.13884	2.3423376	1.94	⋯	⋯	7.34 ± 1.01	617 ± 164
COSMOS-16138	150.11099	2.3439393	1.48	0.0377 ± 0.00342	18.4 ± 6.03	5.15 ± 0.568	16600 ± 59800
COSMOS-16286	150.17699	2.3453918	1.44	1.19 ± 0.0722	114 ± 12.2	7.21 ± 1.23	586 ± 159
COSMOS-16556	150.09303	2.3479519	1.53	4.74 ± 0.695	989 ± 326	⋯	⋯
COSMOS-16733	150.07191	2.3497012	1.26	1.63 ± 0.368	168 ± 45.4	6.05 ± 1.28	611 ± 201
COSMOS-16747	150.14316	2.3498077	1.85	⋯	⋯	4.50 ± 0.901	3270 ± 3340
COSMOS-17277	150.14861	2.3552442	1.86	⋯	⋯	6.47 ± 0.733	684 ± 151
COSMOS-17295	150.18318	2.3553715	1.52	3.71 ± 0.704	746 ± 267	6.73 ± 0.918	691 ± 170
COSMOS-17839	150.15677	2.3607778	1.41	3.89 ± 0.754	286 ± 71.7	11.6 ± 1.14	538 ± 81.4
COSMOS-18149	150.17973	2.3636551	1.79	⋯	⋯	7.64 ± 1.33	665 ± 221
COSMOS-18380	150.17947	2.3662162	1.24	4.42 ± 0.421	353 ± 47.8	12.4 ± 0.871	749 ± 93.8
COSMOS-19148	150.11382	2.3735833	1.50	3.72 ± 0.690	327 ± 85.6	9.21 ± 0.947	597 ± 106
COSMOS-19552	150.17607	2.3774271	1.80	⋯	⋯	5.41 ± 0.569	1850 ± 704
COSMOS-19704	150.13863	2.3791740	1.24	7.48 ± 0.687	655 ± 102	1.23 ± 0.0597	91.3 ± 7.87
COSMOS-19735	150.16785	2.3794894	1.54	6.65 ± 0.624	746 ± 141	11.6 ± 0.745	689 ± 85.1
COSMOS-20027	150.13293	2.3825772	1.21	2.84 ± 0.625	267 ± 75.5	12.6 ± 1.58	1170 ± 303

Table 4
(Continued)

ID	R.A.	Decl.	$z_{\rm grism}$	Hα Flux	Hα EW	[O III] Flux	[O III] EW
COSMOS-20082	150.15094	2.3830087	1.25	4.12 ± 1.04	2190 ± 1940	1.30 ± 0.0280	152 ± 22.2
COSMOS-20137	150.13454	2.3835721	1.21	2.77 ± 0.637	1170 ± 559	2.31 ± 0.0350	621 ± 121
COSMOS-20352	150.11499	2.3857372	1.51	2.73 ± 0.729	1130 ± 736	2.43 ± 0.143	358 ± 61.9
COSMOS-20580	150.11919	2.3881054	1.37	2.11 ± 0.476	448 ± 179	⋯	⋯
COSMOS-21784	150.06802	2.4007618	0.722	2.49 ± 0.731	498 ± 202	⋯	⋯
COSMOS-21818	150.14134	2.4011462	1.40	1.11 ± 0.00881	439 ± 76.8	3.95 ± 0.959	2170 ± 1850
COSMOS-22435	150.10278	2.4074514	1.96	⋯	⋯	2.21 ± 0.569	606 ± 280
COSMOS-22729	150.11542	2.4107754	1.15	7.03 ± 0.840	851 ± 185	⋯	⋯
COSMOS-23873	150.16214	2.4234042	0.787	6.46 ± 1.38	1160 ± 463	⋯	⋯
COSMOS-23970	150.14566	2.4244876	1.23	3.92 ± 0.563	884 ± 242	⋯	⋯
COSMOS-24134	150.08701	2.4266548	1.88	⋯	⋯	2.73 ± 0.766	1500 ± 1210
COSMOS-24292	150.09418	2.4285386	1.20	1.62 ± 0.445	662 ± 335	1.57 ± 0.0174	600 ± 261
COSMOS-24633	150.09578	2.4325151	2.16	⋯	⋯	3.47 ± 0.488	517 ± 137
COSMOS-24717	150.09215	2.4333668	1.92	⋯	⋯	1.39 ± 0.418	2590 ± 3990
COSMOS-24719	150.13957	2.4333744	2.34	⋯	⋯	3.17 ± 0.863	1500 ± 1420
COSMOS-25593	150.13577	2.4433217	1.83	⋯	⋯	5.36 ± 0.935	1300 ± 628
COSMOS-25623	150.08922	2.4437132	1.13	5.43 ± 0.629	982 ± 353	⋯	⋯
COSMOS-25625	150.05818	2.4438756	1.57	6.34 ± 2.04	366 ± 162	20.0 ± 0.905	617 ± 49.6
COSMOS-25761	150.14668	2.4455385	0.697	10.7 ± 2.59	601 ± 201	⋯	⋯
COSMOS-25789	150.14482	2.4457758	2.05	⋯	⋯	8.09 ± 0.748	1040 ± 256
COSMOS-25980	150.07338	2.4479604	1.21	⋯	⋯	4.68 ± 1.27	1220 ± 698
GOODS-N-189	189.13556	62.107368	1.44	2.92 ± 0.447	453 ± 134	5.09 ± 0.670	448 ± 87.5
GOODS-N-634	189.12000	62.116581	1.96	⋯	⋯	4.17 ± 0.445	505 ± 109
GOODS-N-977	189.11124	62.123753	2.30	⋯	⋯	10.8 ± 0.528	664 ± 101
GOODS-N-1131	189.15956	62.126724	0.973	3.61 ± 0.889	536 ± 195	⋯	⋯
GOODS-N-1150	189.09818	62.127140	1.94	⋯	⋯	4.51 ± 0.527	511 ± 134
GOODS-N-1814	189.15044	62.136440	1.36	1.55 ± 0.342	442 ± 168	1.80 ± 0.624	183 ± 74.5
GOODS-N-2575	189.08377	62.144329	0.979	2.49 ± 0.630	499 ± 186	⋯	⋯
GOODS-N-2741	189.21249	62.145847	1.20	2.33 ± 0.507	481 ± 164	2.77 ± 0.112	405 ± 38.8
GOODS-N-2773	189.15611	62.146049	0.949	3.55 ± 0.506	513 ± 108	⋯	⋯
GOODS-N-2839	189.11607	62.146523	2.16	⋯	⋯	4.98 ± 0.508	1130 ± 381
GOODS-N-2915	189.15256	62.147591	0.840	9.91 ± 2.59	589 ± 225	⋯	⋯
GOODS-N-3239	189.24747	62.149544	1.97	⋯	⋯	4.46 ± 0.744	1140 ± 551
GOODS-N-3249	189.17017	62.149899	1.43	⋯	⋯	10.7 ± 0.872	614 ± 82.2
GOODS-N-3786	189.19249	62.154202	2.00	⋯	⋯	7.13 ± 0.553	524 ± 78.6
GOODS-N-4052	189.06155	62.155930	0.712	5.87 ± 1.03	482 ± 112	⋯	⋯
GOODS-N-4123	189.17056	62.156692	1.55	5.64 ± 1.37	824 ± 410	3.45 ± 0.228	170 ± 17.7
GOODS-N-4211	189.17401	62.157352	1.16	5.57 ± 0.527	779 ± 156	⋯	⋯
GOODS-N-4305	189.05817	62.157784	1.43	2.30 ± 0.396	588 ± 188	⋯	⋯
GOODS-N-4384	189.04903	62.158424	1.28	10.4 ± 0.512	687 ± 74.4	4.46 ± 0.904	262 ± 65.2
GOODS-N-4465	189.15208	62.158981	2.10	⋯	⋯	3.59 ± 0.500	639 ± 214
GOODS-N-4649	189.12640	62.160233	1.35	2.26 ± 0.318	724 ± 270	⋯	⋯
GOODS-N-4655	189.26390	62.160522	1.22	⋯	⋯	11.1 ± 1.23	1120 ± 236
GOODS-N-4732	189.22795	62.161102	1.97	⋯	⋯	10.6 ± 0.432	567 ± 43.3
GOODS-N-4921	189.07478	62.162357	0.675	11.3 ± 2.64	909 ± 333	⋯	⋯
GOODS-N-5056	189.19531	62.163254	1.44	⋯	⋯	6.28 ± 0.522	1200 ± 231
GOODS-N-5166	189.10648	62.164013	1.57	5.36 ± 1.58	563 ± 268	4.30 ± 0.787	233 ± 53.3
GOODS-N-5615	189.06891	62.167637	0.666	12.8 ± 2.53	2350 ± 1150	⋯	⋯
GOODS-N-5700	189.01819	62.167728	0.763	4.35 ± 0.888	979 ± 341	⋯	⋯
GOODS-N-6037	189.04846	62.170361	1.30	⋯	⋯	17.8 ± 4.02	2800 ± 2300
GOODS-N-6098	189.19991	62.170631	1.22	⋯	⋯	12.2 ± 0.670	1530 ± 207
GOODS-N-6109	189.00623	62.170750	0.700	14.7 ± 1.77	1650 ± 422	⋯	⋯
GOODS-N-6125	189.02686	62.170723	0.892	5.00 ± 0.938	843 ± 269	⋯	⋯
GOODS-N-6168	189.05121	62.171005	0.732	5.87 ± 1.04	481 ± 113	⋯	⋯
GOODS-N-6497	189.01062	62.173252	0.667	13.8 ± 2.46	1010 ± 293	⋯	⋯
GOODS-N-6543	189.10628	62.173500	2.18	⋯	⋯	5.48 ± 0.520	733 ± 237
GOODS-N-6743	189.12680	62.174755	1.80	⋯	⋯	5.44 ± 0.552	653 ± 138
GOODS-N-6972	189.15002	62.176186	1.86	⋯	⋯	4.30 ± 0.554	862 ± 268
GOODS-N-6980	189.08017	62.176205	1.46	3.79 ± 0.619	635 ± 242	⋯	⋯
GOODS-N-7089	189.24272	62.176971	0.968	6.50 ± 0.640	1510 ± 334	⋯	⋯
GOODS-N-7108	189.05052	62.177078	1.22	⋯	⋯	7.85 ± 1.69	1450 ± 722
GOODS-N-7300	189.18837	62.178383	1.59	⋯	⋯	7.12 ± 0.749	706 ± 128
GOODS-N-7376	189.02509	62.178772	1.35	⋯	⋯	4.54 ± 0.897	887 ± 336
GOODS-N-7654	189.03224	62.180363	0.697	6.38 ± 1.15	1050 ± 324	⋯	⋯

Table 4
(Continued)

ID	R.A.	Decl.	$z_{\rm grism}$	Hα Flux	Hα EW	[O III] Flux	[O III] EW
GOODS-N-7721	189.10764	62.180519	1.97	⋯	⋯	23.4 ± 0.396	957 ± 57.8
GOODS-N-8211	189.01411	62.183311	2.08	⋯	⋯	7.31 ± 0.367	602 ± 72.0
GOODS-N-8866	189.25443	62.186607	1.56	3.92 ± 0.915	579 ± 219	⋯	⋯
GOODS-N-8919	189.03156	62.186768	0.706	5.20 ± 1.11	453 ± 125	⋯	⋯
GOODS-N-9019	189.14874	62.187393	1.67	⋯	⋯	6.46 ± 0.996	758 ± 219
GOODS-N-9168	189.09004	62.188133	1.62	⋯	⋯	9.81 ± 0.403	694 ± 72.4
GOODS-N-9360	189.20587	62.189178	1.24	8.85 ± 0.318	805 ± 60.1	13.7 ± 0.637	725 ± 55.0
GOODS-N-9455	189.00340	62.189629	0.800	3.98 ± 0.961	598 ± 210	⋯	⋯
GOODS-N-9652	189.05803	62.190853	2.00	⋯	⋯	3.33 ± 0.298	509 ± 115
GOODS-N-9758	189.20973	62.191479	0.876	9.50 ± 2.58	1810 ± 1150	⋯	⋯
GOODS-N-10172	189.23032	62.192963	1.18	4.09 ± 0.729	199 ± 42.1	19.7 ± 3.07	1520 ± 517
GOODS-N-10629	189.10774	62.195400	1.15	3.95 ± 0.518	551 ± 130	⋯	⋯
GOODS-N-10962	189.02185	62.196697	1.14	10.7 ± 0.605	470 ± 41.6	20.8 ± 2.74	1330 ± 358
GOODS-N-11779	189.13881	62.200848	1.07	5.26 ± 0.782	983 ± 269	⋯	⋯
GOODS-N-11919	189.23051	62.201527	0.969	2.96 ± 0.560	438 ± 110	⋯	⋯
GOODS-N-12293	189.27179	62.203438	0.786	3.42 ± 0.937	806 ± 341	⋯	⋯
GOODS-N-12391	189.29128	62.203987	0.957	2.21 ± 0.570	438 ± 149	⋯	⋯
GOODS-N-12582	189.29034	62.204628	1.99	⋯	⋯	5.77 ± 0.696	2280 ± 1320
GOODS-N-14074	188.96355	62.211662	1.36	4.75 ± 0.860	966 ± 402	2.35 ± 0.0408	665 ± 148
GOODS-N-14683	189.36327	62.214188	1.80	⋯	⋯	8.78 ± 1.26	511 ± 126
GOODS-N-16527	189.37206	62.224125	1.92	⋯	⋯	3.74 ± 0.524	623 ± 160
GOODS-N-17071	189.27060	62.226666	1.52	3.08 ± 0.545	481 ± 134	4.95 ± 0.722	384 ± 76.3
GOODS-N-17457	189.37981	62.228512	1.02	6.66 ± 0.525	472 ± 51.2	⋯	⋯
GOODS-N-17523	189.02022	62.228901	1.37	1.36 ± 0.0606	143 ± 16.4	5.97 ± 0.965	723 ± 213
GOODS-N-17866	189.10750	62.230721	1.43	2.09 ± 0.477	515 ± 188	0.994 ± 0.0404	129 ± 9.57
GOODS-N-18058	189.04193	62.231552	1.27	2.32 ± 0.524	1290 ± 987	6.06 ± 1.01	2350 ± 1300
GOODS-N-18360	189.04367	62.232933	1.67	⋯	⋯	8.76 ± 0.467	749 ± 82.5
GOODS-N-18858	189.38535	62.234940	1.42	6.70 ± 0.455	428 ± 44.4	13.4 ± 0.729	508 ± 40.6
GOODS-N-18906	189.15027	62.235474	2.32	⋯	⋯	3.25 ± 0.687	614 ± 251
GOODS-N-18909	189.15092	62.235527	0.726	4.02 ± 0.954	917 ± 345	⋯	⋯
GOODS-N-19371	189.19638	62.237774	0.817	2.89 ± 0.446	509 ± 107	⋯	⋯
GOODS-N-19404	189.19017	62.237854	1.19	⋯	⋯	7.19 ± 1.76	3030 ± 2520
GOODS-N-19492	189.06244	62.238068	1.38	2.41 ± 0.435	530 ± 156	0.328 ± 0.0216	33.2 ± 2.74
GOODS-N-19629	189.25555	62.238750	2.14	⋯	⋯	2.69 ± 0.492	539 ± 185
GOODS-N-19876	189.31827	62.239670	1.23	⋯	⋯	6.78 ± 1.82	536 ± 207
GOODS-N-19911	189.22023	62.239819	1.89	⋯	⋯	10.5 ± 0.509	516 ± 45.3
GOODS-N-20021	189.32745	62.240658	1.52	4.18 ± 0.526	834 ± 214	10.8 ± 0.728	1240 ± 188
GOODS-N-20261	189.34995	62.242092	1.79	⋯	⋯	2.67 ± 0.466	522 ± 170
GOODS-N-20561	189.30356	62.243130	1.14	4.08 ± 0.977	195 ± 53.1	16.6 ± 0.781	1210 ± 126
GOODS-N-21438	189.15112	62.247879	0.709	4.43 ± 1.06	864 ± 318	⋯	⋯
GOODS-N-21712	189.31079	62.249405	1.88	⋯	⋯	4.34 ± 0.433	544 ± 96.1
GOODS-N-21956	189.10594	62.250389	1.35	3.58 ± 0.208	426 ± 45.7	8.89 ± 0.378	513 ± 33.3
GOODS-N-22066	189.14209	62.250973	0.939	3.46 ± 0.805	450 ± 138	⋯	⋯
GOODS-N-22263	189.32385	62.251705	1.49	⋯	⋯	6.09 ± 0.685	682 ± 129
GOODS-N-22503	189.19141	62.252914	0.966	6.03 ± 0.524	1020 ± 163	⋯	⋯
GOODS-N-23343	189.15251	62.256817	0.748	18.8 ± 0.697	707 ± 38.3	⋯	⋯
GOODS-N-23410	189.06909	62.256844	1.28	2.17 ± 0.254	344 ± 63.5	5.18 ± 0.477	537 ± 76.0
GOODS-N-23477	189.12759	62.257584	0.685	5.75 ± 1.76	687 ± 297	⋯	⋯
GOODS-N-24063	189.35611	62.260422	1.33	6.59 ± 0.507	1180 ± 230	0.391 ± 0.0558	40.3 ± 6.46
GOODS-N-24359	189.11014	62.261848	1.24	⋯	⋯	4.84 ± 1.04	742 ± 257
GOODS-N-24866	189.19896	62.264336	1.45	2.46 ± 0.540	592 ± 240	6.20 ± 0.785	830 ± 192
GOODS-N-25028	189.36273	62.264938	1.33	2.40 ± 0.315	467 ± 102	1.70 ± 0.387	142 ± 36.8
GOODS-N-25063	189.19714	62.264912	1.45	3.90 ± 0.612	843 ± 292	⋯	⋯
GOODS-N-25229	189.35667	62.265862	1.26	2.49 ± 0.381	374 ± 85.4	5.59 ± 0.703	549 ± 105
GOODS-N-25584	189.23338	62.267483	0.769	3.28 ± 0.765	729 ± 254	⋯	⋯
GOODS-N-25737	189.26631	62.268116	0.671	10.3 ± 2.52	697 ± 242	⋯	⋯
GOODS-N-25980	189.22928	62.269501	1.81	⋯	⋯	6.93 ± 0.495	633 ± 85.3
GOODS-N-26328	189.32814	62.270851	1.86	⋯	⋯	10.2 ± 0.509	512 ± 44.8
GOODS-N-26834	189.23204	62.273380	2.05	⋯	⋯	3.30 ± 0.553	517 ± 157
GOODS-N-26922	189.28343	62.273766	1.15	3.70 ± 0.923	162 ± 46.1	17.4 ± 1.95	939 ± 183
GOODS-N-27339	189.13806	62.275928	2.00	⋯	⋯	5.07 ± 0.651	837 ± 227
GOODS-N-27648	189.26627	62.277630	2.00	⋯	⋯	3.75 ± 0.509	662 ± 169
GOODS-N-28473	189.16154	62.281944	1.68	⋯	⋯	5.67 ± 0.615	609 ± 110
GOODS-N-29616	189.30022	62.288284	2.20	⋯	⋯	4.98 ± 0.513	714 ± 159

Table 4
(Continued)

ID	R.A.	Decl.	$z_{\rm grism}$	Hα Flux	Hα EW	[O III] Flux	[O III] EW
GOODS-N-29828	189.15926	62.289669	0.801	5.31 ± 0.874	453 ± 97.3	⋯	⋯
GOODS-N-29837	189.29887	62.289387	2.05	⋯	⋯	4.94 ± 0.730	751 ± 225
GOODS-N-30178	189.31511	62.291229	0.777	4.38 ± 0.949	514 ± 151	⋯	⋯
GOODS-N-30274	189.18298	62.291988	1.80	⋯	⋯	7.29 ± 1.03	728 ± 209
GOODS-N-30649	189.29634	62.294151	1.99	⋯	⋯	9.47 ± 0.510	654 ± 70.4
GOODS-N-31437	189.33098	62.298653	1.95	⋯	⋯	5.07 ± 0.767	664 ± 231
GOODS-N-32565	189.21706	62.305851	1.77	⋯	⋯	6.62 ± 0.832	586 ± 120
GOODS-N-34223	189.38673	62.317879	1.99	⋯	⋯	2.21 ± 0.477	690 ± 372
GOODS-N-34467	189.35033	62.319881	1.32	0.426 ± 0.0127	68.3 ± 8.86	3.60 ± 0.783	623 ± 222
GOODS-N-34690	189.37816	62.321606	1.31	2.89 ± 0.313	445 ± 90.0	3.83 ± 0.620	249 ± 49.9
GOODS-N-35021	189.22655	62.324757	0.879	4.44 ± 1.14	575 ± 206	⋯	⋯
GOODS-N-35938	189.25066	62.332748	1.88	⋯	⋯	6.34 ± 0.516	649 ± 109
GOODS-N-36244	189.30696	62.335781	1.81	⋯	⋯	3.31 ± 0.549	678 ± 224
GOODS-N-36464	189.28221	62.338219	2.10	⋯	⋯	7.94 ± 0.406	699 ± 93.8
GOODS-N-36597	189.33533	62.339737	1.20	0.925 ± 0.0609	116 ± 14.5	8.54 ± 1.25	2400 ± 1130
GOODS-N-36614	189.28395	62.340065	1.79	⋯	⋯	9.12 ± 0.710	551 ± 77.0
GOODS-N-36639	189.32224	62.340244	1.93	⋯	⋯	7.26 ± 0.420	660 ± 85.9
GOODS-N-36852	189.34686	62.342907	1.61	⋯	⋯	6.59 ± 0.664	933 ± 212
GOODS-N-36886	189.38025	62.343498	1.68	⋯	⋯	10.6 ± 0.624	613 ± 67.4
GOODS-N-37280	189.32249	62.349689	1.52	3.86 ± 0.607	1280 ± 584	4.55 ± 0.811	710 ± 224
GOODS-N-37562	189.30240	62.356068	1.96	⋯	⋯	5.18 ± 0.837	524 ± 161
GOODS-N-37684	189.34985	62.359169	2.16	⋯	⋯	6.26 ± 0.580	669 ± 174
GOODS-N-37750	189.32063	62.362038	1.23	3.92 ± 0.377	490 ± 78.9	9.12 ± 0.747	802 ± 119
GOODS-N-37787	189.32593	62.363380	1.23	2.97 ± 0.468	344 ± 77.8	7.00 ± 0.985	560 ± 119
GOODS-N-37825	189.31441	62.364208	1.82	⋯	⋯	6.09 ± 0.647	891 ± 257
GOODS-N-38085	189.32568	62.374794	1.53	6.96 ± 0.548	604 ± 106	15.9 ± 0.724	606 ± 50.9
GOODS-S-837	53.145458	−27.931650	1.25	3.17 ± 0.782	1390 ± 975	1.32 ± 0.0301	248 ± 91.8
GOODS-S-1200	53.172619	−27.926132	1.18	6.88 ± 0.754	642 ± 135	17.9 ± 3.35	8060 ± 13000
GOODS-S-1280	53.085243	−27.924820	1.34	⋯	⋯	8.62 ± 1.60	1460 ± 1080
GOODS-S-1307	53.165665	−27.924423	2.02	⋯	⋯	1.24 ± 0.331	2390 ± 4170
GOODS-S-1428	53.166126	−27.922604	2.14	⋯	⋯	3.15 ± 0.779	2520 ± 3890
GOODS-S-2126	53.151928	−27.913519	1.29	4.45 ± 0.638	586 ± 156	5.93 ± 1.19	395 ± 114
GOODS-S-2349	53.195194	−27.910748	1.24	4.05 ± 0.797	1300 ± 657	⋯	⋯
GOODS-S-2385	53.173775	−27.910181	2.12	⋯	⋯	6.10 ± 0.999	554 ± 188
GOODS-S-2458	53.144299	−27.909624	1.29	2.58 ± 0.609	479 ± 178	⋯	⋯
GOODS-S-3036	53.184345	−27.904181	1.80	⋯	⋯	17.0 ± 0.698	1330 ± 204
GOODS-S-3470	53.156258	−27.900677	1.09	2.88 ± 0.595	465 ± 160	⋯	⋯
GOODS-S-3503	53.183769	−27.900318	1.13	6.90 ± 1.11	2950 ± 2580	⋯	⋯
GOODS-S-3605	53.081875	−27.899399	1.36	1.40 ± 0.315	531 ± 226	2.60 ± 0.471	385 ± 133
GOODS-S-3691	53.206116	−27.898491	1.84	⋯	⋯	12.2 ± 0.675	1860 ± 427
GOODS-S-3754	53.089710	−27.898136	1.39	2.93 ± 0.670	610 ± 280	⋯	⋯
GOODS-S-4224	53.097111	−27.894272	1.15	2.70 ± 0.619	781 ± 326	⋯	⋯
GOODS-S-4243	53.149162	−27.894236	0.680	8.10 ± 1.96	21900 ± 99700	⋯	⋯
GOODS-S-4277	53.225338	−27.893930	0.830	1.44 ± 0.413	893 ± 645	⋯	⋯
GOODS-S-4447	53.206772	−27.892788	0.907	3.87 ± 0.872	514 ± 266	⋯	⋯
GOODS-S-4577	53.095219	−27.891741	1.89	⋯	⋯	8.22 ± 0.581	1330 ± 273
GOODS-S-4664	53.242924	−27.891121	0.984	3.11 ± 0.845	12800 ± 84100	⋯	⋯
GOODS-S-4695	53.172462	−27.890898	0.830	2.28 ± 0.597	2400 ± 3240	⋯	⋯
GOODS-S-5008	53.098797	−27.888613	1.96	⋯	⋯	4.31 ± 0.757	752 ± 326
GOODS-S-5170	53.071636	−27.887356	1.89	⋯	⋯	7.70 ± 0.988	1400 ± 871
GOODS-S-5522	53.181984	−27.884968	0.670	18.4 ± 1.76	15900 ± 21800	⋯	⋯
GOODS-S-5693	53.122444	−27.883869	1.22	1.49 ± 0.0272	207 ± 19.1	6.74 ± 1.30	855 ± 306
GOODS-S-5819	53.195831	−27.882776	1.80	⋯	⋯	16.3 ± 0.698	1070 ± 147
GOODS-S-6131	53.190098	−27.880674	1.62	⋯	⋯	3.34 ± 0.523	930 ± 440
GOODS-S-6512	53.148899	−27.879049	1.16	4.99 ± 0.977	763 ± 277	⋯	⋯
GOODS-S-6563	53.211002	−27.878271	1.80	⋯	⋯	2.21 ± 0.526	847 ± 676
GOODS-S-6565	53.119820	−27.878271	1.54	⋯	⋯	5.32 ± 0.771	1380 ± 729
GOODS-S-6948	53.210079	−27.876158	1.44	1.75 ± 0.455	681 ± 334	⋯	⋯
GOODS-S-7178	53.112942	−27.874975	1.46	2.51 ± 0.591	917 ± 499	⋯	⋯
GOODS-S-7251	53.113102	−27.874657	1.16	9.01 ± 1.18	2970 ± 1710	11.3 ± 0.479	14000 ± 33100
GOODS-S-7575	53.222092	−27.873365	1.88	⋯	⋯	16.9 ± 0.754	1030 ± 132
GOODS-S-8924	53.139664	−27.867180	1.14	3.96 ± 1.07	1940 ± 1600	⋯	⋯
GOODS-S-9833	53.113636	−27.863239	1.22	2.77 ± 0.414	795 ± 221	3.59 ± 0.953	562 ± 227
GOODS-S-9988	53.188335	−27.862572	1.39	2.69 ± 0.154	1220 ± 645	6.62 ± 1.42	1480 ± 1090

Table 4
(Continued)

ID	R.A.	Decl.	$z_{\rm grism}$	Hα Flux	Hα EW	[O III] Flux	[O III] EW
GOODS-S-10170	53.071465	−27.861874	1.55	3.94 ± 0.714	439 ± 116	2.97 ± 0.836	190 ± 63.9
GOODS-S-10890	53.088978	−27.859093	1.31	6.43 ± 1.51	1090 ± 567	1.76 ± 0.0331	195 ± 48.0
GOODS-S-11190	53.049732	−27.857393	1.53	⋯	⋯	2.97 ± 0.583	3520 ± 5530
GOODS-S-11198	53.114288	−27.857388	1.46	2.78 ± 0.627	4830 ± 7170	0.193 ± 0.00908	69.7 ± 27.7
GOODS-S-11384	53.185322	−27.856487	1.25	2.37 ± 0.516	493 ± 168	2.60 ± 0.469	272 ± 79.2
GOODS-S-11411	53.111324	−27.856447	1.51	⋯	⋯	4.86 ± 0.998	1460 ± 837
GOODS-S-11814	53.155647	−27.854868	1.64	⋯	⋯	2.70 ± 0.665	909 ± 502
GOODS-S-11947	53.195477	−27.854307	1.26	3.97 ± 0.573	1830 ± 927	1.27 ± 0.0278	8540 ± 147000
GOODS-S-12321	53.054779	−27.852760	1.29	0.942 ± 0.0665	299 ± 46.1	2.84 ± 0.764	720 ± 354
GOODS-S-12416	53.149143	−27.852320	1.08	2.22 ± 0.469	1380 ± 859	⋯	⋯
GOODS-S-12533	53.164406	−27.851902	1.32	1.88 ± 0.502	616 ± 284	0.641 ± 0.0213	98.4 ± 16.2
GOODS-S-12862	53.182472	−27.850586	1.52	1.88 ± 0.506	2420 ± 3290	⋯	⋯
GOODS-S-12913	53.080334	−27.850573	1.62	⋯	⋯	9.04 ± 0.736	624 ± 91.2
GOODS-S-13422	53.180275	−27.848263	1.24	1.74 ± 0.397	833 ± 378	1.26 ± 0.0295	202 ± 41.6
GOODS-S-13542	53.131561	−27.848051	0.879	6.62 ± 1.88	3670 ± 4290	⋯	⋯
GOODS-S-13681	53.139824	−27.847273	1.39	1.34 ± 0.288	459 ± 177	1.51 ± 0.443	263 ± 111
GOODS-S-13724	53.276436	−27.847153	1.37	2.21 ± 0.574	1160 ± 653	⋯	⋯
GOODS-S-13848	53.074135	−27.847355	1.55	10.9 ± 2.12	519 ± 156	⋯	⋯
GOODS-S-13971	53.194202	−27.846256	1.60	⋯	⋯	5.97 ± 1.60	4280 ± 11700
GOODS-S-14290	53.200741	−27.844654	0.735	6.43 ± 1.68	7220 ± 15500	⋯	⋯
GOODS-S-14712	53.124001	−27.842756	0.938	2.86 ± 0.698	2620 ± 2590	⋯	⋯
GOODS-S-14762	53.184814	−27.842615	2.14	⋯	⋯	2.13 ± 0.585	645 ± 354
GOODS-S-14794	53.215893	−27.842464	0.976	2.83 ± 0.554	705 ± 263	⋯	⋯
GOODS-S-14889	53.100739	−27.842028	1.42	1.30 ± 0.327	686 ± 319	⋯	⋯
GOODS-S-15049	53.103371	−27.841627	2.03	⋯	⋯	8.43 ± 0.555	1050 ± 170
GOODS-S-15276	53.204987	−27.840679	1.23	5.75 ± 0.566	375 ± 50.7	18.4 ± 1.20	968 ± 124
GOODS-S-15291	53.148418	−27.840612	1.13	8.55 ± 0.746	645 ± 103	⋯	⋯
GOODS-S-15334	53.125191	−27.840452	2.00	⋯	⋯	6.47 ± 1.67	2490 ± 2720
GOODS-S-15424	53.223213	−27.840080	1.92	⋯	⋯	14.4 ± 0.666	1310 ± 194
GOODS-S-15523	53.138069	−27.839523	1.56	2.68 ± 0.0501	448 ± 47.1	6.04 ± 1.04	420 ± 105
GOODS-S-15665	53.125278	−27.838997	1.10	3.51 ± 0.772	1040 ± 521	⋯	⋯
GOODS-S-16052	53.143864	−27.837248	1.37	2.34 ± 0.572	1430 ± 877	⋯	⋯
GOODS-S-16102	53.125561	−27.836992	0.997	2.42 ± 0.575	3600 ± 5440	⋯	⋯
GOODS-S-16240	53.185169	−27.836500	2.01	⋯	⋯	3.78 ± 0.671	1120 ± 509
GOODS-S-16287	53.079006	−27.836510	0.902	2.14 ± 0.584	630 ± 297	⋯	⋯
GOODS-S-16354	53.059391	−27.836082	1.37	2.28 ± 0.439	288 ± 72.1	7.66 ± 0.677	639 ± 98.8
GOODS-S-16375	53.124832	−27.835806	0.877	2.48 ± 0.758	2390 ± 2520	⋯	⋯
GOODS-S-16426	53.145569	−27.835545	1.39	3.01 ± 0.534	1010 ± 367	0.640 ± 0.0107	203 ± 62.5
GOODS-S-16953	53.075905	−27.833208	0.744	1.12 ± 0.262	522 ± 212	⋯	⋯
GOODS-S-17123	53.142136	−27.832689	2.15	⋯	⋯	10.3 ± 0.597	803 ± 99.1
GOODS-S-17176	53.178444	−27.832317	1.52	3.18 ± 0.705	1540 ± 918	1.60 ± 0.0399	221 ± 27.5
GOODS-S-18045	53.177853	−27.827993	1.52	0.786 ± 0.0160	283 ± 66.6	2.00 ± 0.548	1360 ± 1290
GOODS-S-18336	53.139023	−27.826862	1.88	⋯	⋯	4.97 ± 0.510	509 ± 88.2
GOODS-S-18614	53.168438	−27.825298	1.31	⋯	⋯	3.84 ± 0.938	6530 ± 14000
GOODS-S-19449	53.069408	−27.821138	1.60	9.92 ± 1.73	815 ± 261	5.36 ± 0.885	181 ± 35.8
GOODS-S-19766	53.128792	−27.819513	1.18	1.64 ± 0.368	886 ± 427	1.96 ± 0.0265	854 ± 401
GOODS-S-19850	53.145493	−27.819019	1.90	⋯	⋯	2.67 ± 0.460	1060 ± 429
GOODS-S-19856	53.055019	−27.818970	1.19	1.00 ± 0.266	1990 ± 2340	⋯	⋯
GOODS-S-19863	53.144180	−27.819082	1.44	6.51 ± 1.35	4630 ± 6140	⋯	⋯
GOODS-S-20002	53.064465	−27.818233	0.676	4.72 ± 1.20	71700 ± 1130000	⋯	⋯
GOODS-S-20011	53.077019	−27.818350	0.837	3.78 ± 1.07	1180 ± 688	⋯	⋯
GOODS-S-20320	53.077751	−27.816778	1.35	3.44 ± 0.743	773 ± 302	⋯	⋯
GOODS-S-20360	53.175785	−27.816561	2.08	⋯	⋯	7.26 ± 0.543	812 ± 129
GOODS-S-20614	53.148045	−27.815449	1.12	2.13 ± 0.597	135 ± 43.0	13.3 ± 0.889	1810 ± 401
GOODS-S-21024	53.077606	−27.812796	1.72	⋯	⋯	8.54 ± 0.533	920 ± 151
GOODS-S-21386	53.053501	−27.810917	0.731	5.52 ± 1.56	1460 ± 908	⋯	⋯
GOODS-S-21446	53.160847	−27.810450	1.29	3.10 ± 0.660	1640 ± 975	⋯	⋯
GOODS-S-21485	53.151291	−27.810291	1.12	2.35 ± 0.473	561 ± 198	⋯	⋯
GOODS-S-21634	53.187328	−27.809486	1.76	⋯	⋯	3.62 ± 0.749	607 ± 220
GOODS-S-21839	53.035423	−27.808380	2.01	⋯	⋯	7.79 ± 0.375	554 ± 50.8
GOODS-S-22153	53.173111	−27.806791	2.07	⋯	⋯	4.36 ± 0.512	862 ± 223
GOODS-S-22217	53.049274	−27.806379	2.07	⋯	⋯	3.62 ± 0.551	894 ± 301
GOODS-S-22418	53.077320	−27.805359	1.32	0.634 ± 0.0142	151 ± 18.5	3.58 ± 0.571	679 ± 203
GOODS-S-22518	53.150715	−27.804852	1.33	2.63 ± 0.512	1600 ± 834	⋯	⋯

Table 4
(Continued)

ID	R.A.	Decl.	$z_{\rm grism}$	Hα Flux	Hα EW	[O III] Flux	[O III] EW
GOODS-S-22706	53.061478	−27.804739	1.34	9.24 ± 0.933	1000 ± 224	0.112 ± 0.0499	8.16 ± 3.75
GOODS-S-22759	53.099091	−27.803829	1.89	⋯	⋯	9.32 ± 0.596	1130 ± 184
GOODS-S-22927	53.068264	−27.802792	1.45	0.111 ± 0.00210	80.5 ± 15.9	1.29 ± 0.347	924 ± 758
GOODS-S-23083	53.201866	−27.801991	1.52	0.631 ± 0.0102	314 ± 73.1	3.75 ± 0.721	2260 ± 1990
GOODS-S-23185	53.148609	−27.801540	1.39	4.19 ± 0.838	1230 ± 573	0.771 ± 0.0268	149 ± 33.2
GOODS-S-23375	53.153698	−27.801035	1.31	3.27 ± 0.431	1870 ± 764	⋯	⋯
GOODS-S-23400	53.120480	−27.800640	1.18	3.64 ± 0.528	379 ± 73.7	10.6 ± 2.36	1540 ± 776
GOODS-S-23563	53.065708	−27.799576	1.45	1.63 ± 0.403	1750 ± 1270	⋯	⋯
GOODS-S-23819	53.161110	−27.798798	1.24	2.94 ± 0.633	632 ± 218	3.51 ± 0.619	461 ± 123
GOODS-S-24185	53.084415	−27.797331	1.89	⋯	⋯	4.76 ± 0.719	766 ± 251
GOODS-S-24355	53.168804	−27.796940	1.99	⋯	⋯	9.15 ± 0.815	909 ± 181
GOODS-S-24420	53.136589	−27.795877	1.34	1.90 ± 0.230	533 ± 115	2.95 ± 0.403	313 ± 61.9
GOODS-S-24441	53.066948	−27.795803	1.51	2.97 ± 0.434	665 ± 176	5.63 ± 0.591	658 ± 135
GOODS-S-24523	53.163528	−27.795513	1.27	1.13 ± 0.244	554 ± 208	0.973 ± 0.0314	312 ± 77.5
GOODS-S-24699	53.143520	−27.795219	2.03	⋯	⋯	13.0 ± 0.563	854 ± 81.1
GOODS-S-25015	53.059223	−27.793444	1.17	5.11 ± 0.661	682 ± 148	8.62 ± 0.976	1340 ± 373
GOODS-S-25104	53.048405	−27.792900	1.36	1.55 ± 0.392	820 ± 416	⋯	⋯
GOODS-S-25443	53.164600	−27.791498	1.23	1.26 ± 0.319	976 ± 539	⋯	⋯
GOODS-S-25457	53.194885	−27.791533	1.39	0.781 ± 0.0150	115 ± 10.5	6.71 ± 1.11	2000 ± 1110
GOODS-S-25476	53.191322	−27.791725	2.15	⋯	⋯	5.64 ± 0.860	650 ± 189
GOODS-S-25515	53.164467	−27.791409	1.11	1.14 ± 0.313	499 ± 257	⋯	⋯
GOODS-S-25664	53.066807	−27.790512	0.767	4.47 ± 1.05	46700 ± 497000	⋯	⋯
GOODS-S-25906	53.190125	−27.789604	1.23	3.94 ± 0.543	980 ± 281	⋯	⋯
GOODS-S-26271	53.148613	−27.788639	1.22	1.11 ± 0.0688	217 ± 28.2	5.56 ± 1.01	1310 ± 540
GOODS-S-26820	53.139160	−27.786161	1.29	2.31 ± 0.426	625 ± 190	0.279 ± 0.0168	61.8 ± 11.4
GOODS-S-27151	53.169338	−27.784979	1.23	2.81 ± 0.427	1780 ± 773	1.15 ± 0.0311	703 ± 295
GOODS-S-27354	53.067852	−27.784081	1.22	5.99 ± 0.585	577 ± 86.2	5.97 ± 1.25	393 ± 110
GOODS-S-27805	53.162445	−27.782408	1.41	3.52 ± 0.556	736 ± 201	⋯	⋯
GOODS-S-28085	53.153877	−27.781647	1.22	⋯	⋯	4.37 ± 1.08	1110 ± 549
GOODS-S-28093	53.167458	−27.781830	1.34	3.36 ± 0.569	580 ± 157	0.783 ± 0.0238	114 ± 14.1
GOODS-S-28951	53.072197	−27.778198	2.30	⋯	⋯	2.91 ± 0.696	761 ± 444
GOODS-S-29258	53.073353	−27.776871	2.31	⋯	⋯	2.39 ± 0.702	764 ± 513
GOODS-S-29721	53.139233	−27.774845	1.17	2.95 ± 0.451	828 ± 227	⋯	⋯
GOODS-S-30252	53.084778	−27.772577	2.07	⋯	⋯	3.86 ± 1.04	1380 ± 1050
GOODS-S-30692	53.099098	−27.771067	1.94	⋯	⋯	8.37 ± 0.676	1020 ± 211
GOODS-S-31087	53.063488	−27.769209	0.716	4.85 ± 1.16	640 ± 229	⋯	⋯
GOODS-S-31523	53.046303	−27.767313	1.54	6.37 ± 0.776	429 ± 78.0	13.6 ± 0.930	504 ± 57.4
GOODS-S-32209	53.067493	−27.763996	1.85	⋯	⋯	2.84 ± 0.733	950 ± 639
GOODS-S-32384	53.098091	−27.763073	1.23	3.64 ± 0.633	770 ± 261	⋯	⋯
GOODS-S-32407	53.098335	−27.762840	1.92	⋯	⋯	5.16 ± 0.515	1920 ± 753
GOODS-S-33251	53.049965	−27.758417	1.21	3.07 ± 0.665	498 ± 166	⋯	⋯
GOODS-S-33425	53.052319	−27.757015	2.33	⋯	⋯	4.06 ± 0.522	915 ± 268
GOODS-S-33487	53.199833	−27.756844	1.20	2.27 ± 0.515	279 ± 80.6	4.24 ± 0.316	520 ± 93.7
GOODS-S-35710	53.152443	−27.745783	1.26	4.74 ± 0.664	32300 ± 164000	0.343 ± 0.0181	60.1 ± 12.0
GOODS-S-38590	53.197628	−27.730164	1.21	2.67 ± 0.399	230 ± 42.9	11.4 ± 1.13	1070 ± 240
GOODS-S-38815	53.123707	−27.728868	1.27	1.90 ± 0.407	878 ± 350	0.600 ± 0.0123	253 ± 77.1
GOODS-S-38875	53.146263	−27.728584	1.26	2.34 ± 0.460	564 ± 176	⋯	⋯
GOODS-S-39455	53.167259	−27.725777	1.16	2.22 ± 0.384	946 ± 315	⋯	⋯
GOODS-S-40130	53.149517	−27.722540	1.95	⋯	⋯	0.575 ± 0.165	507 ± 286
GOODS-S-40773	53.034565	−27.719316	1.30	⋯	⋯	2.70 ± 0.617	513 ± 187
GOODS-S-41868	53.076801	−27.714430	1.17	11.5 ± 0.615	2570 ± 488	10.3 ± 1.07	3890 ± 1960
GOODS-S-41939	53.158768	−27.714027	1.59	5.45 ± 0.308	647 ± 74.7	2.91 ± 0.696	149 ± 41.3
GOODS-S-42634	53.122681	−27.710855	2.10	⋯	⋯	3.09 ± 0.545	757 ± 300
GOODS-S-42680	53.096508	−27.711098	0.678	7.42 ± 1.76	495 ± 155	⋯	⋯
GOODS-S-44306	53.126945	−27.703011	1.39	4.53 ± 0.972	655 ± 250	⋯	⋯
GOODS-S-44676	53.084862	−27.701469	1.82	⋯	⋯	16.7 ± 0.566	1150 ± 106
GOODS-S-45517	53.165897	−27.697260	1.55	⋯	⋯	3.40 ± 0.866	1860 ± 1820
GOODS-S-45613	53.163010	−27.697145	1.31	5.44 ± 0.379	580 ± 71.9	12.8 ± 0.706	872 ± 108
GOODS-S-45891	53.159233	−27.695976	1.86	⋯	⋯	5.64 ± 0.799	1230 ± 490
GOODS-S-46290	53.249107	−27.693930	2.17	⋯	⋯	6.28 ± 0.515	778 ± 136
GOODS-S-47162	53.250690	−27.689890	1.18	3.52 ± 0.585	882 ± 267	7.53 ± 1.72	6620 ± 10200
GOODS-S-48148	53.162949	−27.684923	1.28	4.87 ± 0.811	458 ± 112	3.34 ± 0.229	199 ± 24.2
GOODS-S-49563	53.164776	−27.675711	1.22	3.90 ± 0.389	591 ± 101	7.86 ± 0.903	1090 ± 273
GOODS-S-49640	53.142208	−27.674990	0.719	2.30 ± 0.424	1900 ± 1390	⋯	⋯

Table 4
(Continued)

ID	R.A.	Decl.	$z_{\rm grism}$	Hα Flux	Hα EW	[O III] Flux	[O III] EW
UDS-1366	34.353588	−5.2725129	1.04	11.1 ± 0.620	574 ± 57.0	⋯	⋯
UDS-3335	34.355267	−5.2652259	1.03	5.22 ± 0.710	585 ± 143	⋯	⋯
UDS-3401	34.342609	−5.2648201	1.13	3.02 ± 0.698	1710 ± 2080	⋯	⋯
UDS-4112	34.240303	−5.2623968	1.35	1.18 ± 0.260	1290 ± 866	1.65 ± 0.449	344 ± 150
UDS-4287	34.351265	−5.2620931	0.862	11.8 ± 1.21	897 ± 178	⋯	⋯
UDS-4415	34.298279	−5.2614808	1.49	4.52 ± 0.529	398 ± 70.1	11.2 ± 0.733	600 ± 75.5
UDS-4484	34.296291	−5.2615819	0.697	8.71 ± 2.27	701 ± 271	⋯	⋯
UDS-4702	34.437412	−5.2606029	1.32	0.716 ± 0.0156	119 ± 15.5	4.83 ± 1.06	1010 ± 491
UDS-5078	34.357811	−5.2592731	1.71	⋯	⋯	4.71 ± 0.653	801 ± 278
UDS-5178	34.356472	−5.2590151	1.85	⋯	⋯	6.17 ± 0.569	580 ± 97.2
UDS-5253	34.484184	−5.2588329	1.47	3.88 ± 0.564	444 ± 108	10.2 ± 0.825	735 ± 128
UDS-5457	34.441109	−5.2581692	0.956	2.34 ± 0.592	639 ± 317	⋯	⋯
UDS-5635	34.364017	−5.2577338	0.962	6.96 ± 0.745	592 ± 104	⋯	⋯
UDS-5789	34.448101	−5.2573032	1.97	⋯	⋯	7.49 ± 1.06	1480 ± 828
UDS-5976	34.409725	−5.2565150	1.54	7.65 ± 0.863	1180 ± 357	6.26 ± 1.07	365 ± 93.6
UDS-5995	34.345886	−5.2563911	1.81	⋯	⋯	5.84 ± 0.702	560 ± 160
UDS-6411	34.334530	−5.2548800	0.987	3.54 ± 0.911	5000 ± 9380	⋯	⋯
UDS-6609	34.252907	−5.2542558	1.66	⋯	⋯	1.78 ± 0.374	1740 ± 2730
UDS-6684	34.346451	−5.2540078	1.42	0.606 ± 0.00885	507 ± 275	2.63 ± 0.677	2170 ± 2270
UDS-6803	34.329422	−5.2537651	1.66	⋯	⋯	6.67 ± 1.02	616 ± 177
UDS-7054	34.489674	−5.2527270	2.01	⋯	⋯	7.64 ± 0.642	1460 ± 522
UDS-7216	34.370613	−5.2521129	1.44	1.23 ± 0.135	266 ± 49.9	3.05 ± 0.659	517 ± 197
UDS-7227	34.453926	−5.2521920	2.12	⋯	⋯	5.33 ± 0.652	856 ± 244
UDS-7338	34.442104	−5.2517762	1.34	1.10 ± 0.310	367 ± 160	3.69 ± 0.559	863 ± 331
UDS-7508	34.480202	−5.2512112	1.52	3.06 ± 0.468	476 ± 118	6.45 ± 0.622	629 ± 131
UDS-7529	34.314007	−5.2510490	1.72	⋯	⋯	4.01 ± 0.584	560 ± 172
UDS-7658	34.355919	−5.2505612	0.878	4.16 ± 1.13	2040 ± 2060	⋯	⋯
UDS-8237	34.475731	−5.2484999	1.34	2.80 ± 0.500	724 ± 246	0.338 ± 0.0249	37.0 ± 5.48
UDS-8542	34.291782	−5.2473202	2.09	⋯	⋯	2.83 ± 0.718	7630 ± 23500
UDS-8551	34.291065	−5.2473402	1.80	⋯	⋯	3.45 ± 0.600	527 ± 208
UDS-8623	34.397060	−5.2470069	2.35	⋯	⋯	2.38 ± 0.580	996 ± 620
UDS-8771	34.388950	−5.2465239	1.62	⋯	⋯	3.05 ± 0.785	661 ± 366
UDS-8873	34.438358	−5.2463331	1.21	3.22 ± 0.453	378 ± 76.5	7.70 ± 1.23	748 ± 208
UDS-9536	34.249508	−5.2442002	1.52	4.60 ± 0.694	472 ± 114	8.49 ± 0.921	518 ± 102
UDS-9596	34.360989	−5.2436790	2.02	⋯	⋯	3.76 ± 0.617	747 ± 280
UDS-9640	34.340427	−5.2436442	1.86	⋯	⋯	3.75 ± 0.581	621 ± 184
UDS-9770	34.307419	−5.2430372	2.16	⋯	⋯	2.81 ± 0.457	505 ± 148
UDS-10010	34.252083	−5.2425199	1.85	⋯	⋯	9.03 ± 0.926	573 ± 109
UDS-10040	34.365025	−5.2426720	1.06	5.23 ± 1.04	667 ± 249	⋯	⋯
UDS-10358	34.397701	−5.2411828	1.93	⋯	⋯	7.91 ± 0.671	530 ± 86.9
UDS-10497	34.389332	−5.2406492	1.17	7.09 ± 0.632	1890 ± 597	⋯	⋯
UDS-10516	34.366505	−5.2405701	1.53	⋯	⋯	8.06 ± 0.627	1220 ± 320
UDS-10531	34.300388	−5.2405348	1.59	1.65 ± 0.0486	633 ± 171	3.83 ± 0.872	1350 ± 950
UDS-10686	34.422009	−5.2401352	2.07	⋯	⋯	5.86 ± 0.559	768 ± 164
UDS-10798	34.352158	−5.2397728	1.39	2.28 ± 0.486	265 ± 75.8	7.86 ± 0.812	546 ± 102
UDS-10996	34.456600	−5.2392650	1.53	6.24 ± 0.554	456 ± 64.6	9.06 ± 0.715	498 ± 69.4
UDS-11010	34.311279	−5.2389569	1.67	⋯	⋯	11.6 ± 0.759	2580 ± 902
UDS-11220	34.254829	−5.2384338	0.805	4.97 ± 1.14	622 ± 245	⋯	⋯
UDS-11323	34.309448	−5.2379818	1.81	⋯	⋯	3.71 ± 0.707	539 ± 179
UDS-11394	34.384090	−5.2378469	2.20	⋯	⋯	8.13 ± 0.596	670 ± 139
UDS-11617	34.328140	−5.2368980	1.36	1.41 ± 0.356	1080 ± 740	2.09 ± 0.410	732 ± 422
UDS-11622	34.468914	−5.2368870	1.53	⋯	⋯	2.11 ± 0.0519	2390 ± 5010
UDS-11653	34.255917	−5.2369242	1.15	2.48 ± 0.568	378 ± 119	8.57 ± 0.395	2110 ± 619
UDS-11782	34.260956	−5.2363749	1.02	3.43 ± 0.588	1000 ± 435	⋯	⋯
UDS-11947	34.486671	−5.2358060	1.19	0.0510 ± 0.000640	30.4 ± 8.67	0.847 ± 0.226	799 ± 1060
UDS-12058	34.260975	−5.2357769	1.53	4.76 ± 0.817	405 ± 109	11.0 ± 1.02	531 ± 89.0
UDS-12750	34.476509	−5.2332578	1.70	⋯	⋯	5.26 ± 1.11	882 ± 471
UDS-12863	34.280373	−5.2327399	1.53	1.61 ± 0.0696	260 ± 41.0	5.82 ± 0.896	733 ± 245
UDS-12980	34.482590	−5.2324300	1.42	4.50 ± 0.502	462 ± 80.8	9.23 ± 0.771	679 ± 113
UDS-12983	34.449387	−5.2324510	1.75	⋯	⋯	6.18 ± 1.35	2110 ± 2190
UDS-13027	34.318146	−5.2322888	1.66	⋯	⋯	12.7 ± 0.842	661 ± 88.6
UDS-13112	34.241680	−5.2318902	0.829	3.98 ± 0.993	1030 ± 506	⋯	⋯
UDS-13166	34.332851	−5.2317281	1.36	3.13 ± 0.685	571 ± 217	⋯	⋯
UDS-13734	34.405849	−5.2297311	1.84	⋯	⋯	2.39 ± 0.575	893 ± 548

Table 4
(Continued)

ID	R.A.	Decl.	$z_{\rm grism}$	Hα Flux	Hα EW	[O III] Flux	[O III] EW
UDS-13893	34.319138	−5.2292719	1.77	⋯	⋯	3.63 ± 0.679	545 ± 188
UDS-14507	34.279331	−5.2270608	1.74	⋯	⋯	5.84 ± 1.21	858 ± 430
UDS-14519	34.433552	−5.2270021	1.38	0.275 ± 0.00247	187 ± 75.4	1.82 ± 0.316	1650 ± 2250
UDS-14551	34.480339	−5.2269030	1.16	3.05 ± 0.611	7690 ± 14300	⋯	⋯
UDS-14948	34.246735	−5.2255821	1.85	⋯	⋯	3.87 ± 0.679	604 ± 190
UDS-14979	34.433552	−5.2254720	1.10	4.01 ± 0.710	875 ± 364	⋯	⋯
UDS-15301	34.250927	−5.2244458	1.72	⋯	⋯	9.18 ± 0.696	505 ± 75.1
UDS-15632	34.477806	−5.2233038	1.69	⋯	⋯	6.51 ± 0.917	1370 ± 653
UDS-15697	34.272663	−5.2231021	1.01	1.98 ± 0.549	976 ± 674	⋯	⋯
UDS-16065	34.414307	−5.2218289	0.918	2.12 ± 0.425	914 ± 471	⋯	⋯
UDS-16254	34.490692	−5.2212710	1.82	⋯	⋯	2.27 ± 0.568	542 ± 237
UDS-16448	34.382668	−5.2206449	0.879	6.75 ± 0.720	1490 ± 451	⋯	⋯
UDS-16538	34.426506	−5.2202792	1.69	⋯	⋯	6.70 ± 1.22	523 ± 177
UDS-16979	34.449486	−5.2189789	1.47	⋯	⋯	7.72 ± 0.908	841 ± 232
UDS-17021	34.273628	−5.2187238	1.82	⋯	⋯	2.66 ± 0.631	945 ± 497
UDS-17043	34.267166	−5.2186499	0.852	2.14 ± 0.588	471 ± 194	⋯	⋯
UDS-17117	34.466820	−5.2184539	1.47	1.68 ± 0.0714	852 ± 398	3.70 ± 0.913	1210 ± 956
UDS-17175	34.338642	−5.2182879	1.06	2.32 ± 0.552	547 ± 259	⋯	⋯
UDS-17378	34.377110	−5.2175970	1.86	⋯	⋯	3.03 ± 0.751	580 ± 256
UDS-17821	34.350067	−5.2161341	2.16	⋯	⋯	2.76 ± 0.570	1030 ± 544
UDS-17891	34.441456	−5.2159491	1.27	⋯	⋯	6.93 ± 1.42	776 ± 283
UDS-18378	34.417839	−5.2142420	2.31	⋯	⋯	2.96 ± 0.692	602 ± 268
UDS-18399	34.482910	−5.2141900	1.78	⋯	⋯	13.4 ± 0.849	743 ± 110
UDS-18487	34.321365	−5.2138591	2.02	⋯	⋯	2.47 ± 0.371	638 ± 199
UDS-18489	34.246582	−5.2142162	0.820	8.02 ± 1.49	479 ± 124	⋯	⋯
UDS-19025	34.344074	−5.2122149	1.02	5.20 ± 0.767	785 ± 237	⋯	⋯
UDS-19379	34.384724	−5.2110820	1.29	0.855 ± 0.0193	261 ± 50.3	3.90 ± 0.957	937 ± 486
UDS-19488	34.258385	−5.2106109	1.44	0.773 ± 0.0164	255 ± 57.6	2.98 ± 0.706	1200 ± 845
UDS-19673	34.384911	−5.2099891	1.36	3.69 ± 0.487	704 ± 191	⋯	⋯
UDS-19756	34.411926	−5.2096300	1.46	⋯	⋯	7.51 ± 1.42	2980 ± 3310
UDS-19901	34.331684	−5.2091999	2.03	⋯	⋯	4.42 ± 0.493	981 ± 313
UDS-19916	34.367950	−5.2090540	2.11	⋯	⋯	3.60 ± 0.636	742 ± 312
UDS-20001	34.399971	−5.2087350	1.62	⋯	⋯	4.52 ± 0.703	1130 ± 516
UDS-20084	34.234360	−5.2084160	1.32	1.35 ± 0.352	3540 ± 5800	0.899 ± 0.00847	732 ± 809
UDS-20398	34.331394	−5.2075319	1.41	4.01 ± 0.544	350 ± 68.3	11.0 ± 0.845	800 ± 128
UDS-20495	34.394260	−5.2071290	2.00	⋯	⋯	3.98 ± 0.693	552 ± 184
UDS-20570	34.377995	−5.2069979	1.36	0.896 ± 0.0307	89.5 ± 12.7	5.65 ± 1.30	602 ± 242
UDS-20635	34.395344	−5.2067070	1.51	4.96 ± 0.830	619 ± 195	0.361 ± 0.0200	49.5 ± 15.5
UDS-20661	34.477825	−5.2063909	1.16	1.58 ± 0.423	1020 ± 589	⋯	⋯
UDS-20779	34.432873	−5.2060928	1.85	⋯	⋯	6.66 ± 0.556	600 ± 96.4
UDS-21035	34.415604	−5.2051382	1.28	1.27 ± 0.329	923 ± 680	1.36 ± 0.0303	797 ± 648
UDS-21065	34.443684	−5.2050161	1.65	⋯	⋯	7.13 ± 1.02	898 ± 340
UDS-21241	34.331646	−5.2045002	1.90	⋯	⋯	1.85 ± 0.459	778 ± 499
UDS-21248	34.377171	−5.2045178	0.856	5.60 ± 1.38	1390 ± 825	⋯	⋯
UDS-21454	34.408455	−5.2037601	1.36	2.53 ± 0.469	722 ± 251	2.57 ± 0.818	360 ± 163
UDS-21493	34.430519	−5.2036090	1.63	⋯	⋯	4.14 ± 0.765	834 ± 355
UDS-21544	34.233280	−5.2033939	1.34	2.16 ± 0.482	1380 ± 824	2.72 ± 0.286	991 ± 523
UDS-21693	34.269058	−5.2029681	1.38	1.58 ± 0.368	511 ± 230	⋯	⋯
UDS-22401	34.450665	−5.2006020	2.07	⋯	⋯	1.38 ± 0.353	626 ± 327
UDS-22490	34.486767	−5.2002850	1.23	1.55 ± 0.424	197 ± 66.8	1.81 ± 0.0666	606 ± 311
UDS-22582	34.450706	−5.1999741	1.46	1.97 ± 0.330	900 ± 365	2.34 ± 0.493	399 ± 148
UDS-22854	34.320648	−5.1991849	0.920	8.68 ± 1.21	910 ± 249	⋯	⋯
UDS-23058	34.332878	−5.1985159	0.913	9.82 ± 0.820	928 ± 160	⋯	⋯
UDS-23246	34.273159	−5.1980100	1.42	2.98 ± 0.719	397 ± 146	9.69 ± 1.22	973 ± 294
UDS-23462	34.318947	−5.1971092	1.93	⋯	⋯	3.26 ± 0.760	1550 ± 1210
UDS-23736	34.257263	−5.1962409	1.35	2.51 ± 0.492	473 ± 161	0.0999 ± 0.0155	15.2 ± 4.12
UDS-24156	34.483181	−5.1946840	2.01	⋯	⋯	3.44 ± 0.688	1420 ± 953
UDS-24660	34.447311	−5.1931400	1.60	⋯	⋯	3.67 ± 0.742	529 ± 200
UDS-25216	34.400497	−5.1912079	0.904	3.28 ± 0.830	900 ± 450	⋯	⋯
UDS-25482	34.325401	−5.1903219	0.905	2.93 ± 0.764	1630 ± 1180	⋯	⋯
UDS-26182	34.367222	−5.1881309	1.49	5.38 ± 0.593	752 ± 164	10.0 ± 0.937	584 ± 97.1
UDS-26299	34.377548	−5.1875601	1.27	0.676 ± 0.0175	86.0 ± 12.0	5.25 ± 1.16	1110 ± 577
UDS-26455	34.236366	−5.1870771	1.54	⋯	⋯	3.75 ± 0.778	838 ± 383
UDS-26778	34.483891	−5.1859989	0.990	3.23 ± 0.674	663 ± 255	⋯	⋯
UDS-27040	34.434547	−5.1850610	2.19	⋯	⋯	9.88 ± 0.487	599 ± 71.1

Table 4
(Continued)

ID	R.A.	Decl.	z_{grism}	Hα Flux	Hα EW	[O III] Flux	[O III] EW
UDS-27380	34.273766	−5.1838331	1.79	⋯	⋯	9.57 ± 0.811	666 ± 124
UDS-27556	34.347805	−5.1835289	1.98	⋯	⋯	8.70 ± 0.705	588 ± 91.3
UDS-27572	34.478226	−5.1831889	2.31	⋯	⋯	2.24 ± 0.431	1050 ± 569
UDS-27648	34.441082	−5.1832800	1.65	⋯	⋯	5.97 ± 1.16	684 ± 270
UDS-28429	34.468678	−5.1803698	1.62	⋯	⋯	3.24 ± 0.757	534 ± 268
UDS-28438	34.416744	−5.1804309	1.73	⋯	⋯	6.41 ± 0.885	809 ± 264
UDS-28699	34.361294	−5.1794491	1.43	3.52 ± 0.850	880 ± 493	⋯	⋯
UDS-28889	34.338703	−5.1788631	1.40	5.69 ± 0.548	1100 ± 257	14.8 ± 0.864	1900 ± 424
UDS-28915	34.455471	−5.1788192	1.28	2.22 ± 0.400	254 ± 58.9	6.63 ± 0.758	594 ± 121
UDS-29046	34.292496	−5.1783762	1.45	7.39 ± 0.708	781 ± 155	15.3 ± 1.02	757 ± 103
UDS-29260	34.590645	−5.1777501	1.20	3.99 ± 0.672	344 ± 83.2	10.6 ± 2.21	647 ± 217
UDS-29441	34.329006	−5.1769872	1.63	⋯	⋯	2.76 ± 0.552	563 ± 243
UDS-29452	34.324875	−5.1770229	1.57	⋯	⋯	6.55 ± 1.10	536 ± 156
UDS-29624	34.252850	−5.1763620	1.66	⋯	⋯	6.29 ± 0.745	653 ± 162
UDS-29843	34.453415	−5.1759601	1.41	0.612 ± 0.0258	62.6 ± 7.66	7.26 ± 1.28	860 ± 328
UDS-30205	34.450710	−5.1745639	1.81	⋯	⋯	3.90 ± 0.746	579 ± 201
UDS-30446	34.300304	−5.1737261	1.17	4.33 ± 0.718	753 ± 231	⋯	⋯
UDS-30554	34.349991	−5.1734719	0.706	8.83 ± 2.56	1670 ± 1130	⋯	⋯
UDS-31241	34.420250	−5.1712122	1.53	1.62 ± 0.0623	299 ± 51.6	6.26 ± 0.820	1040 ± 368
UDS-31610	34.419853	−5.1700168	1.91	⋯	⋯	3.15 ± 0.511	652 ± 223
UDS-31741	34.331799	−5.1696792	1.87	⋯	⋯	6.99 ± 0.436	895 ± 147
UDS-31774	34.327744	−5.1694942	1.93	⋯	⋯	3.51 ± 0.455	727 ± 204
UDS-31838	34.455120	−5.1692929	1.45	0.895 ± 0.00993	646 ± 343	⋯	⋯
UDS-31978	34.369289	−5.1688471	2.03	⋯	⋯	3.90 ± 0.633	568 ± 170
UDS-32817	34.367294	−5.1659789	1.44	2.05 ± 0.578	399 ± 167	5.40 ± 0.849	552 ± 152
UDS-32874	34.314701	−5.1657710	1.42	2.24 ± 0.348	607 ± 184	4.31 ± 1.05	535 ± 217
UDS-33577	34.261475	−5.1632762	1.15	3.37 ± 0.550	19600 ± 73900	⋯	⋯
UDS-33612	34.410946	−5.1632128	1.63	⋯	⋯	11.8 ± 1.69	897 ± 310
UDS-33665	34.410954	−5.1630940	1.65	⋯	⋯	9.89 ± 1.26	528 ± 123
UDS-33916	34.392994	−5.1622438	1.81	⋯	⋯	6.38 ± 0.966	610 ± 179
UDS-34037	34.323193	−5.1619348	1.18	⋯	⋯	15.5 ± 3.13	24300 ± 109000
UDS-34056	34.326794	−5.1616878	1.69	⋯	⋯	3.67 ± 0.697	597 ± 224
UDS-34332	34.580730	−5.1608148	1.11	1.81 ± 0.453	859 ± 426	⋯	⋯
UDS-34394	34.309872	−5.1607022	1.54	2.96 ± 0.692	528 ± 219	7.14 ± 0.841	900 ± 271
UDS-34566	34.285503	−5.1600642	0.893	5.72 ± 1.20	518 ± 164	⋯	⋯
UDS-34694	34.298069	−5.1596580	1.42	4.93 ± 0.689	1180 ± 434	⋯	⋯
UDS-34788	34.366478	−5.1591878	1.39	⋯	⋯	3.26 ± 0.780	865 ± 475
UDS-34789	34.399185	−5.1593881	1.49	0.550 ± 0.0167	82.6 ± 10.4	3.91 ± 0.966	617 ± 279
UDS-35202	34.376583	−5.1576829	1.82	⋯	⋯	5.18 ± 0.514	1710 ± 845
UDS-35357	34.354942	−5.1571488	1.86	⋯	⋯	1.84 ± 0.504	1350 ± 1050
UDS-35634	34.297489	−5.1562128	2.26	⋯	⋯	3.08 ± 0.682	1380 ± 1110
UDS-35645	34.330196	−5.1561799	1.03	5.36 ± 0.581	656 ± 142	⋯	⋯
UDS-36071	34.391644	−5.1546612	1.85	⋯	⋯	3.43 ± 0.665	1120 ± 613
UDS-36186	34.350861	−5.1543331	1.82	⋯	⋯	6.68 ± 0.676	792 ± 177
UDS-36374	34.581318	−5.1535578	1.76	⋯	⋯	5.25 ± 0.700	501 ± 126
UDS-36656	34.333088	−5.1527538	1.15	4.15 ± 0.739	426 ± 112	⋯	⋯
UDS-36678	34.412140	−5.1525779	0.946	5.94 ± 1.77	39900 ± 503000	⋯	⋯
UDS-36706	34.383137	−5.1524811	1.28	1.43 ± 0.0209	2240 ± 1660	⋯	⋯
UDS-36804	34.353790	−5.1522531	1.42	⋯	⋯	8.92 ± 1.15	995 ± 302
UDS-38182	34.353466	−5.1473489	1.44	0.410 ± 0.0212	64.6 ± 8.58	5.67 ± 1.37	887 ± 432
UDS-38212	34.325237	−5.1470728	1.54	3.09 ± 0.541	535 ± 176	6.14 ± 1.29	504 ± 174
UDS-38344	34.331123	−5.1467509	1.97	⋯	⋯	10.3 ± 0.546	737 ± 84.3
UDS-38550	34.335613	−5.1458831	0.901	3.93 ± 1.01	1240 ± 845	⋯	⋯
UDS-38634	34.345181	−5.1455841	1.56	2.10 ± 0.611	691 ± 362	2.07 ± 0.462	376 ± 147
UDS-39273	34.248646	−5.1431599	1.43	2.35 ± 0.689	717 ± 369	4.72 ± 1.05	960 ± 498
UDS-39324	34.386852	−5.1430278	1.65	⋯	⋯	2.64 ± 0.733	1810 ± 2240
UDS-40202	34.364071	−5.1397529	1.07	3.38 ± 0.827	531 ± 204	⋯	⋯
UDS-40377	34.246796	−5.1391230	1.67	⋯	⋯	6.59 ± 0.696	732 ± 183
UDS-40449	34.255833	−5.1388960	1.84	⋯	⋯	4.09 ± 0.650	1030 ± 380
UDS-41271	34.247959	−5.1363411	1.35	⋯	⋯	2.43 ± 0.584	1330 ± 1220

Note. ID numbers come from Skelton et al. (2014); all EW values are quoted in the restframe (Å); fluxes are in units of 10^{-17} erg s^{-1} cm^{-2}.

Table 5
Plausible High-EW [O III] Emitters

ID	R.A.	Decl.	Observed Wavelength (Å)	Line Flux	Line EW
AEGIS-2591	214.82121	52.734825	14870	3.36 ± 0.779	732 ± 374
AEGIS-4571	214.76666	52.704880	13010	3.05 ± 0.782	1670 ± 1470
AEGIS-5587	215.08670	52.936558	15780	3.93 ± 0.440	680 ± 177
AEGIS-6006	214.81204	52.743362	15000	3.83 ± 0.572	2420 ± 1670
AEGIS-6011	214.76630	52.710670	11630	2.60 ± 0.643	1270 ± 884
AEGIS-6257	214.99388	52.873756	16160	1.58 ± 0.421	704 ± 443
AEGIS-6434	214.99304	52.873871	13990	3.17 ± 0.815	939 ± 671
AEGIS-6539	215.07777	52.934299	14830	3.27 ± 0.674	1650 ± 1340
AEGIS-6767	214.96376	52.854675	13870	2.15 ± 0.544	3490 ± 6520
AEGIS-6879	215.03569	52.906033	12040	3.45 ± 0.865	912 ± 473
AEGIS-8174	215.03490	52.911091	13320	1.66 ± 0.434	559 ± 323
AEGIS-8382	214.90004	52.816338	12240	4.56 ± 0.725	25200 ± 144000
AEGIS-8655	214.78299	52.734146	16650	1.62 ± 0.353	563 ± 268
AEGIS-9076	215.02058	52.905025	11279	4.15 ± 1.02	1280 ± 732
AEGIS-9091	214.96394	52.865013	14260	1.80 ± 0.469	1830 ± 1830
AEGIS-9214	214.99026	52.884216	13950	1.58 ± 0.418	1580 ± 2260
AEGIS-10381	215.08174	52.954208	15060	0.815 ± 0.213	928 ± 653
AEGIS-12492	214.94946	52.869167	13890	1.98 ± 0.479	600 ± 271
AEGIS-12739	214.89198	52.829151	12100	3.83 ± 0.874	501 ± 183
AEGIS-13072	214.86176	52.809200	16570	1.92 ± 0.383	7590 ± 24100
AEGIS-13133	214.95912	52.878731	12370	3.03 ± 0.717	4080 ± 6650
AEGIS-14616	214.95506	52.881905	14450	1.42 ± 0.322	1250 ± 928
AEGIS-15043	214.95546	52.883713	15060	4.91 ± 0.639	527 ± 119
AEGIS-15615	214.92952	52.867352	12750	10.8 ± 2.13	12400 ± 41800
AEGIS-15767	215.04005	52.946175	13070	4.27 ± 0.768	703 ± 240
AEGIS-15874	214.92139	52.862732	13660	2.31 ± 0.399	885 ± 416
AEGIS-16103	215.06589	52.966091	15690	2.26 ± 0.571	522 ± 247
AEGIS-16476	214.81667	52.790764	11480	5.03 ± 0.572	552 ± 108
AEGIS-16541	214.82396	52.796326	12320	1.20 ± 0.307	5950 ± 28200
AEGIS-17256	215.02727	52.943531	10990	4.29 ± 1.02	157000 ± 6300000
AEGIS-18966	215.05078	52.967091	12010	2.34 ± 0.618	14000 ± 82800
AEGIS-19466	214.95070	52.898403	14100	2.34 ± 0.445	2560 ± 2550
AEGIS-20606	215.01050	52.945072	15000	3.79 ± 0.668	932 ± 366
AEGIS-21349	215.03943	52.968464	12160	5.15 ± 0.848	2880000 ± 2150000000
AEGIS-21381	214.80721	52.803780	14440	1.50 ± 0.225	5690 ± 11100
AEGIS-21386	215.03511	52.965542	13770	3.28 ± 0.839	1200 ± 822
AEGIS-21460	214.77489	52.781078	15750	1.89 ± 0.336	2430 ± 2870
AEGIS-21578	214.70604	52.732269	14680	1.34 ± 0.270	695 ± 326
AEGIS-21892	214.79283	52.795631	14530	2.52 ± 0.512	1040 ± 542
AEGIS-21911	214.92023	52.886337	15380	1.66 ± 0.418	610 ± 343
AEGIS-22001	214.71802	52.742523	13779	1.11 ± 0.290	642 ± 495
AEGIS-22792	214.91608	52.887028	11339	2.16 ± 0.566	1120 ± 711
AEGIS-23112	215.02165	52.963001	12160	2.16 ± 0.570	5950 ± 18700
AEGIS-23215	215.03101	52.969910	13700	3.67 ± 0.890	1500 ± 1220
AEGIS-23490	214.96118	52.921707	15240	2.89 ± 0.690	951 ± 572
AEGIS-24380	214.68259	52.726536	16040	2.26 ± 0.536	1240 ± 1030
AEGIS-24651	214.95714	52.923172	14900	1.73 ± 0.393	846 ± 448
AEGIS-26086	214.81529	52.828270	14260	1.43 ± 0.337	575 ± 240
AEGIS-26131	214.78325	52.805618	11570	8.00 ± 1.57	763 ± 294
AEGIS-26196	214.86792	52.866184	15310	1.10 ± 0.293	1210 ± 995
AEGIS-26314	214.92303	52.905739	12860	3.27 ± 0.703	1820 ± 1690
AEGIS-26417	215.01060	52.968082	13770	4.64 ± 0.616	1160 ± 442
AEGIS-26722	214.72409	52.765526	15109	3.14 ± 0.431	1830 ± 1370
AEGIS-26885	214.97740	52.946369	13410	2.26 ± 0.494	1120 ± 725
AEGIS-26949	214.83017	52.842125	14560	2.62 ± 0.461	1160 ± 502
AEGIS-26973	214.91129	52.899853	15320	2.37 ± 0.592	6710 ± 17100
AEGIS-27249	214.93016	52.914036	14730	2.49 ± 0.532	545 ± 211
AEGIS-27404	214.90790	52.899078	11850	6.70 ± 1.70	1880 ± 1520
AEGIS-27674	215.01747	52.977829	12080	4.78 ± 1.31	8830 ± 26900
AEGIS-28130	214.75885	52.795849	12540	3.74 ± 0.757	15100 ± 64800
AEGIS-28305	214.78836	52.817608	16450	1.35 ± 0.348	628 ± 322
AEGIS-28641	214.72311	52.772202	15480	1.78 ± 0.439	1610 ± 1560
AEGIS-28865	214.78380	52.816536	14520	2.63 ± 0.544	2600 ± 2800
AEGIS-29054	215.02423	52.987961	11090	1.59 ± 0.394	1700 ± 1480

Table 5
(Continued)

ID	R.A.	Decl.	Observed Wavelength (Å)	Line Flux	Line EW
AEGIS-29359	215.00870	52.978176	15850	2.39 ± 0.625	1190 ± 962
AEGIS-29513	215.00894	52.978916	15440	4.25 ± 1.08	1460 ± 1200
AEGIS-30218	214.74583	52.794861	15490	1.95 ± 0.472	15000 ± 93900
AEGIS-30580	214.97784	52.961166	11410	3.04 ± 0.625	12700 ± 49300
AEGIS-31136	214.81473	52.847519	12850	5.81 ± 1.14	713 ± 268
AEGIS-31186	214.80594	52.841614	11459	5.85 ± 1.40	2740 ± 2440
AEGIS-31445	214.97542	52.962925	14160	2.73 ± 0.429	501 ± 133
AEGIS-31696	214.70062	52.768436	14130	3.47 ± 0.502	10300 ± 24600
AEGIS-32037	214.66882	52.746845	13720	3.86 ± 0.847	889 ± 479
AEGIS-33016	214.87094	52.894753	14250	3.85 ± 0.412	843 ± 204
AEGIS-34210	214.85767	52.890228	15660	3.94 ± 0.763	21600 ± 171000
AEGIS-34307	214.74451	52.809940	15160	1.18 ± 0.288	588 ± 294
AEGIS-34313	214.95526	52.959812	13879	1.43 ± 0.393	556 ± 318
AEGIS-34904	214.74979	52.816189	13360	1.41 ± 0.380	865 ± 629
AEGIS-35962	214.90584	52.931343	11339	5.11 ± 1.29	4310 ± 6620
AEGIS-36065	214.75366	52.823532	15530	2.52 ± 0.662	752 ± 429
AEGIS-36805	215.00267	53.003426	13790	3.04 ± 0.731	2900 ± 4530
AEGIS-37430	214.72035	52.805382	13819	3.07 ± 0.785	1060 ± 771
AEGIS-37836	214.79253	52.858398	11870	5.50 ± 1.14	5960 ± 10200
AEGIS-38457	214.97322	52.988567	15169	1.07 ± 0.265	773 ± 444
AEGIS-38639	214.71240	52.803825	14540	1.48 ± 0.401	1110 ± 801
AEGIS-39296	214.70782	52.803379	15120	2.63 ± 0.664	1950 ± 2029
AEGIS-39415	214.75151	52.835136	13250	6.33 ± 1.69	2610 ± 3040
AEGIS-40302	214.92603	52.964081	13120	2.31 ± 0.613	981 ± 756
AEGIS-40573	214.74345	52.836651	14550	2.72 ± 0.529	758 ± 329
COSMOS-3488	150.13533	2.2135367	15069	0.880 ± 0.224	596 ± 341
COSMOS-3623	150.08623	2.2148292	15750	10.4 ± 0.636	619 ± 79.2
COSMOS-4184	150.12868	2.2197511	13430	2.38 ± 0.591	8410 ± 34300
COSMOS-5115	150.16490	2.2294831	12270	3.07 ± 0.700	4560 ± 8029
COSMOS-5441	150.16075	2.2330527	14790	2.28 ± 0.525	10600 ± 43700
COSMOS-5846	150.09070	2.2372763	14400	4.64 ± 1.18	2320 ± 2600
COSMOS-6059	150.08870	2.2391183	13980	1.53 ± 0.373	1300 ± 1890
COSMOS-6227	150.09727	2.2408817	11399	1.86 ± 0.444	632 ± 295
COSMOS-6656	150.11053	2.2457266	14210	8.94 ± 0.677	979 ± 174
COSMOS-7403	150.10789	2.2539482	12370	2.61 ± 0.735	2850 ± 4160
COSMOS-8102	150.09238	2.2619281	14620	2.71 ± 0.570	635 ± 276
COSMOS-8253	150.14404	2.2636330	12600	3.02 ± 0.840	911 ± 539
COSMOS-9396	150.17590	2.2747848	16020	1.69 ± 0.230	2250 ± 2090
COSMOS-12965	150.15599	2.3110466	14230	2.98 ± 0.801	2780 ± 3900
COSMOS-15969	150.18779	2.3421500	12810	4.77 ± 1.08	4100 ± 6500
COSMOS-16398	150.08755	2.3463194	13530	2.50 ± 0.622	1660 ± 1630
COSMOS-16873	150.12032	2.3509953	14240	2.44 ± 0.357	2450 ± 1830
COSMOS-18972	150.16946	2.3718252	15790	1.36 ± 0.278	511 ± 201
COSMOS-19337	150.12595	2.3752594	13700	1.91 ± 0.347	524 ± 250
COSMOS-20010	150.07558	2.3823094	12580	2.51 ± 0.537	866 ± 439
COSMOS-20800	150.17123	2.3907106	15320	2.86 ± 0.601	847 ± 430
COSMOS-21672	150.09764	2.3997040	16470	2.17 ± 0.503	1920 ± 2130
COSMOS-25912	150.06102	2.4472728	15690	3.08 ± 0.590	1250 ± 811
GOODS-N-3299	189.16490	62.150021	11310	3.72 ± 0.628	776 ± 244
GOODS-N-3374	189.05640	62.150524	16090	3.96 ± 0.663	666 ± 273
GOODS-N-3927	189.11139	62.154934	16050	3.50 ± 0.936	584 ± 321
GOODS-N-4021	189.23238	62.155647	12810	3.11 ± 0.711	575 ± 208
GOODS-N-4241	189.03639	62.157307	10940	10.2 ± 2.21	2260 ± 1390
GOODS-N-4516	189.10188	62.159382	16500	2.78 ± 0.405	510 ± 163
GOODS-N-4879	189.05602	62.161877	11760	6.57 ± 1.25	603 ± 184
GOODS-N-4932	189.04645	62.162182	16410	7.94 ± 0.876	12000 ± 37500
GOODS-N-4938	189.05481	62.162289	10890	17.4 ± 2.63	29300 ± 112000
GOODS-N-5339	189.03757	62.165493	10850	16.9 ± 3.21	825 ± 258
GOODS-N-5458	189.06667	62.166168	10860	19.0 ± 2.19	8750 ± 8250
GOODS-N-5783	189.07335	62.168430	11430	4.16 ± 0.651	1780 ± 810
GOODS-N-5864	189.17674	62.169003	14530	2.79 ± 0.581	649 ± 318
GOODS-N-5899	189.02925	62.169132	16660	3.94 ± 0.667	1550 ± 1030
GOODS-N-6591	189.04190	62.173679	14090	3.85 ± 0.580	821 ± 271
GOODS-N-6785	189.06837	62.174931	12070	6.70 ± 0.868	1390 ± 577

Table 5
(Continued)

ID	R.A.	Decl.	Observed Wavelength (Å)	Line Flux	Line EW
GOODS-N-6803	189.06308	62.175079	11930	4.86 ± 0.906	1340 ± 696
GOODS-N-7001	189.01628	62.176250	11480	3.58 ± 0.618	698 ± 212
GOODS-N-7206	189.06047	62.177654	11430	4.67 ± 1.00	3190 ± 3400
GOODS-N-7370	189.03123	62.178467	11700	7.15 ± 1.36	559 ± 163
GOODS-N-7374	189.21507	62.178894	11980	3.80 ± 0.991	1640 ± 1110
GOODS-N-7804	189.00580	62.181068	11610	5.22 ± 0.954	1180 ± 486
GOODS-N-8424	189.04825	62.184502	11470	3.16 ± 0.732	751 ± 327
GOODS-N-8775	189.04411	62.186214	11030	3.98 ± 0.956	1140 ± 585
GOODS-N-9804	189.00787	62.191498	14980	3.86 ± 0.762	1020 ± 556
GOODS-N-10028	189.20233	62.192635	12470	4.07 ± 1.03	575 ± 224
GOODS-N-11596	189.26529	62.199852	11690	4.25 ± 0.997	1130 ± 532
GOODS-N-13609	189.22510	62.209740	14660	2.97 ± 0.679	940 ± 551
GOODS-N-14577	189.29930	62.213917	14400	2.83 ± 0.657	549 ± 244
GOODS-N-15043	188.99237	62.216179	14180	2.38 ± 0.496	635 ± 262
GOODS-N-15733	189.10405	62.219849	12569	5.44 ± 1.38	1600 ± 1040
GOODS-N-15753	189.30885	62.219978	14370	6.92 ± 0.918	1200 ± 432
GOODS-N-16711	189.37814	62.224888	14580	7.74 ± 0.676	577 ± 96.7
GOODS-N-17551	189.19939	62.228920	16430	4.51 ± 0.725	783 ± 319
GOODS-N-18147	189.38429	62.231976	15330	3.58 ± 0.469	557 ± 136
GOODS-N-20175	189.25299	62.241631	14870	3.36 ± 0.525	633 ± 191
GOODS-N-21035	189.23860	62.245640	15220	3.12 ± 0.816	514 ± 224
GOODS-N-22099	189.26669	62.250881	11090	4.31 ± 1.19	560 ± 225
GOODS-N-22194	189.16501	62.251522	12520	3.68 ± 0.542	569 ± 131
GOODS-N-23176	189.22412	62.256035	15060	6.42 ± 0.772	580 ± 138
GOODS-N-23400	189.29601	62.257252	15290	3.37 ± 0.432	551 ± 126
GOODS-N-23617	189.25714	62.258244	16550	3.63 ± 0.878	1440 ± 1250
GOODS-N-25129	189.24142	62.265308	16900	5.32 ± 1.41	2360 ± 2760
GOODS-N-25555	189.24471	62.267456	12040	2.99 ± 0.631	737 ± 264
GOODS-N-25928	189.25554	62.269218	11419	4.87 ± 1.21	847 ± 366
GOODS-N-28962	189.20071	62.284702	14070	5.85 ± 0.531	1770 ± 617
GOODS-N-29382	189.27193	62.286884	15410	4.89 ± 1.35	1520 ± 1320
GOODS-N-29670	189.23718	62.288376	11930	4.59 ± 0.673	879 ± 236
GOODS-N-30027	189.31236	62.290489	16780	7.39 ± 1.46	1200 ± 736
GOODS-N-30414	189.17955	62.292835	11730	5.37 ± 1.11	1090 ± 444
GOODS-N-31702	189.34167	62.300137	15480	4.50 ± 0.850	2170 ± 2029
GOODS-N-32755	189.29001	62.307255	13919	3.80 ± 0.772	590 ± 234
GOODS-N-35025	189.38252	62.324425	15760	4.76 ± 0.477	599 ± 132
GOODS-S-857	53.099827	−27.931149	14070	1.61 ± 0.411	2170 ± 2700
GOODS-S-2149	53.213116	−27.913292	10870	11.5 ± 3.06	1570 ± 1010
GOODS-S-2206	53.094612	−27.912619	13790	2.05 ± 0.563	38100 ± 1370000
GOODS-S-2564	53.147030	−27.908655	16130	1.47 ± 0.379	966 ± 1070
GOODS-S-2850	53.131664	−27.905975	14490	2.20 ± 0.497	1700 ± 1350
GOODS-S-3134	53.200184	−27.903448	15100	3.26 ± 0.826	2930 ± 5140
GOODS-S-3797	53.167576	−27.897810	12800	2.18 ± 0.574	3970 ± 12500
GOODS-S-3834	53.251415	−27.897375	15069	1.55 ± 0.418	600 ± 409
GOODS-S-3901	53.082958	−27.897009	14670	3.31 ± 0.879	1540 ± 1550
GOODS-S-4075	53.204121	−27.895588	11510	1.79 ± 0.465	1670 ± 2440
GOODS-S-4111	53.104446	−27.895266	15089	2.96 ± 0.710	4600 ± 10100
GOODS-S-4399	53.131924	−27.893078	13990	1.53 ± 0.403	1080 ± 1370
GOODS-S-4548	53.232903	−27.891897	14890	2.01 ± 0.485	994 ± 778
GOODS-S-4742	53.128403	−27.890518	14330	0.958 ± 0.228	754 ± 569
GOODS-S-5168	53.091652	−27.887386	14480	3.69 ± 0.742	579 ± 221
GOODS-S-5510	53.203171	−27.884966	11200	3.55 ± 0.858	1770 ± 1890
GOODS-S-5857	53.112328	−27.882446	12540	3.90 ± 1.18	14200 ± 150000
GOODS-S-6057	53.199680	−27.881132	11250	4.71 ± 1.38	1120 ± 866
GOODS-S-6101	53.158710	−27.880861	13100	2.87 ± 0.763	2740 ± 4810
GOODS-S-6145	53.160732	−27.880577	13130	0.767 ± 0.216	1510 ± 3940
GOODS-S-6156	53.154045	−27.880486	12589	2.67 ± 0.737	4820 ± 14900
GOODS-S-6407	53.139179	−27.879194	12900	8.89 ± 2.30	4390 ± 7480
GOODS-S-6728	53.131393	−27.877291	13750	3.45 ± 0.828	46300 ± 1560000
GOODS-S-6828	53.207573	−27.876778	16510	3.69 ± 0.784	5240 ± 10500
GOODS-S-6973	53.209045	−27.876013	15830	1.53 ± 0.417	1080 ± 840
GOODS-S-7031	53.116123	−27.875740	15280	5.21 ± 1.10	29700 ± 378000
GOODS-S-7069	53.205917	−27.875645	12880	5.94 ± 0.958	2310 ± 2060

Table 5
(Continued)

ID	R.A.	Decl.	Observed Wavelength (Å)	Line Flux	Line EW
GOODS-S-7107	53.082130	−27.875345	13030	3.12 ± 0.765	12600 ± 67000
GOODS-S-7441	53.087933	−27.873741	14710	2.21 ± 0.552	963 ± 559
GOODS-S-7865	53.097286	−27.871799	12700	1.57 ± 0.428	775 ± 612
GOODS-S-7876	53.133766	−27.871752	13830	1.72 ± 0.505	5320 ± 21600
GOODS-S-8104	53.118374	−27.870626	13500	2.71 ± 0.682	4550 ± 15800
GOODS-S-8562	53.140793	−27.868483	13450	1.46 ± 0.373	534 ± 329
GOODS-S-8620	53.137993	−27.868246	14670	6.23 ± 1.27	3540 ± 4070
GOODS-S-8865	53.169193	−27.867493	14400	3.91 ± 0.970	1230 ± 777
GOODS-S-8943	53.140610	−27.866894	15140	3.75 ± 0.834	7090 ± 15500
GOODS-S-9002	53.144650	−27.866688	13630	0.660 ± 0.190	618 ± 891
GOODS-S-9247	53.070988	−27.865776	16660	3.67 ± 0.836	803 ± 429
GOODS-S-9810	53.279396	−27.863226	16270	1.44 ± 0.387	1130 ± 854
GOODS-S-10724	53.158199	−27.859350	15700	1.56 ± 0.416	5000 ± 16100
GOODS-S-11552	53.076530	−27.855795	15240	2.81 ± 0.635	1510 ± 1060
GOODS-S-11668	53.114681	−27.855362	16420	2.59 ± 0.438	6050 ± 11500
GOODS-S-11739	53.112591	−27.855101	12110	2.85 ± 0.617	2350 ± 3310
GOODS-S-12017	53.094070	−27.853968	11020	3.09 ± 0.754	21500 ± 164000
GOODS-S-12149	53.082424	−27.853424	13230	1.52 ± 0.403	4070 ± 11399
GOODS-S-12521	53.158833	−27.851877	14090	2.11 ± 0.566	3270 ± 4640
GOODS-S-12904	53.179115	−27.850409	13250	1.75 ± 0.464	1650 ± 2930
GOODS-S-12925	53.064571	−27.850277	15670	1.10 ± 0.289	519 ± 271
GOODS-S-13082	53.299656	−27.849686	11319	5.48 ± 1.44	1380 ± 874
GOODS-S-13149	53.052792	−27.849421	12470	1.42 ± 0.390	574 ± 372
GOODS-S-14796	53.193237	−27.842394	14140	0.515 ± 0.142	524 ± 326
GOODS-S-15174	53.123592	−27.840939	12680	1.74 ± 0.328	1090 ± 708
GOODS-S-15264	53.220699	−27.840458	13220	1.67 ± 0.441	206999 ± 40800000
GOODS-S-16275	53.131065	−27.836279	12990	1.84 ± 0.414	4800 ± 13400
GOODS-S-16381	53.075287	−27.835852	13720	3.46 ± 1.02	1050 ± 776
GOODS-S-17010	53.192379	−27.832956	15140	4.42 ± 0.833	1360 ± 737
GOODS-S-17400	53.185280	−27.831366	11790	4.90 ± 1.45	3260 ± 4340
GOODS-S-17578	53.113850	−27.830294	15290	1.17 ± 0.265	928 ± 527
GOODS-S-17783	53.109192	−27.829281	14690	3.76 ± 0.855	3860 ± 5650
GOODS-S-17882	53.150982	−27.828842	13530	2.21 ± 0.536	3780 ± 8530
GOODS-S-18271	53.127495	−27.826986	13220	0.789 ± 0.207	598 ± 539
GOODS-S-18531	53.131763	−27.825735	15620	0.943 ± 0.219	1110 ± 753
GOODS-S-18708	53.209820	−27.824814	11950	2.37 ± 0.679	2810 ± 5470
GOODS-S-18853	53.099239	−27.824104	12529	5.47 ± 1.37	3390 ± 4280
GOODS-S-19198	53.111374	−27.822281	14550	1.16 ± 0.281	4910 ± 11100
GOODS-S-19264	53.052528	−27.821917	13000	2.07 ± 0.461	4950 ± 15600
GOODS-S-19515	53.152832	−27.820738	14020	1.42 ± 0.371	1160 ± 1670
GOODS-S-19556	53.050831	−27.820572	12840	2.33 ± 0.582	1490 ± 1390
GOODS-S-19750	53.048344	−27.819523	13420	1.97 ± 0.497	1130 ± 1000
GOODS-S-20001	53.110741	−27.818211	16090	1.50 ± 0.396	810 ± 472
GOODS-S-20040	53.213696	−27.818169	14570	8.12 ± 0.779	1330 ± 336
GOODS-S-20117	53.126629	−27.817881	13680	7.64 ± 1.67	4320 ± 8360
GOODS-S-20270	53.180748	−27.816919	13970	4.44 ± 1.04	997 ± 610
GOODS-S-20324	53.090145	−27.816603	10920	0.647 ± 0.168	581 ± 461
GOODS-S-20497	53.206066	−27.815632	13440	1.32 ± 0.354	1360 ± 1940
GOODS-S-20653	53.164665	−27.814882	12620	5.80 ± 1.26	1940 ± 2690
GOODS-S-21249	53.085155	−27.811466	13730	1.27 ± 0.355	4059 ± 14200
GOODS-S-21602	53.100868	−27.809593	13010	2.14 ± 0.465	1460 ± 1210
GOODS-S-21751	53.185093	−27.808712	15470	1.25 ± 0.278	561 ± 237
GOODS-S-21973	53.045662	−27.807533	11190	1.23 ± 0.321	664 ± 433
GOODS-S-22144	53.121700	−27.806778	15000	1.46 ± 0.372	2380 ± 3400
GOODS-S-22454	53.054745	−27.805061	11790	1.45 ± 0.343	9390 ± 56800
GOODS-S-22510	53.165020	−27.805305	15910	1.91 ± 0.408	849 ± 488
GOODS-S-22626	53.186375	−27.804276	11319	1.59 ± 0.390	928 ± 672
GOODS-S-22693	53.074966	−27.804140	15320	2.36 ± 0.513	1530 ± 1080
GOODS-S-25233	53.065609	−27.792440	15800	3.03 ± 0.557	805 ± 309
GOODS-S-25848	53.145302	−27.789997	14230	1.95 ± 0.406	20400 ± 159000
GOODS-S-25945	53.129395	−27.789284	14330	0.839 ± 0.220	541 ± 257
GOODS-S-26579	53.138428	−27.787008	16200	1.24 ± 0.318	1240 ± 1060
GOODS-S-27006	53.115276	−27.785353	14980	4.26 ± 0.953	4080 ± 6030
GOODS-S-28130	53.134460	−27.781309	11200	3.64 ± 0.953	1070 ± 633

Table 5
(Continued)

ID	R.A.	Decl.	Observed Wavelength (Å)	Line Flux	Line EW
GOODS-S-28278	53.153412	−27.781034	14180	8.43 ± 0.704	1520 ± 367
GOODS-S-28358	53.060810	−27.780312	15560	1.34 ± 0.272	1860 ± 1930
GOODS-S-28535	53.187008	−27.779913	13290	1.88 ± 0.447	1260 ± 1050
GOODS-S-28948	53.118717	−27.778034	14480	0.979 ± 0.279	1130 ± 974
GOODS-S-30091	53.109383	−27.773294	14480	3.57 ± 0.476	2330 ± 1370
GOODS-S-30472	53.073921	−27.771667	12110	2.18 ± 0.580	1790 ± 1940
GOODS-S-30900	53.085228	−27.769903	15490	1.55 ± 0.371	7380 ± 20700
GOODS-S-31002	53.144653	−27.769415	13970	3.14 ± 0.730	3350 ± 6990
GOODS-S-31400	53.033901	−27.767548	16680	5.87 ± 1.69	8880 ± 35200
GOODS-S-31835	53.059002	−27.765631	12390	2.82 ± 0.677	2140 ± 3110
GOODS-S-31845	53.028072	−27.765587	12870	3.21 ± 0.608	2020 ± 1630
GOODS-S-32272	53.030697	−27.763508	13530	0.521 ± 0.142	533 ± 590
GOODS-S-33170	53.100166	−27.758532	13919	0.647 ± 0.171	863 ± 1770
GOODS-S-33473	53.113029	−27.756750	14970	2.66 ± 0.389	1010 ± 383
GOODS-S-33771	53.035622	−27.755228	15200	1.75 ± 0.508	2060 ± 2220
GOODS-S-34072	53.146656	−27.753853	15340	0.928 ± 0.247	1550 ± 1950
GOODS-S-34351	53.020096	−27.752531	15340	2.85 ± 0.712	615 ± 281
GOODS-S-34407	53.102562	−27.752132	14060	1.16 ± 0.273	537 ± 239
GOODS-S-34676	53.023720	−27.750677	15149	1.53 ± 0.352	538 ± 222
GOODS-S-34934	53.023567	−27.749598	15320	2.99 ± 0.722	1200 ± 750
GOODS-S-35156	53.129391	−27.748552	14010	1.65 ± 0.443	582 ± 384
GOODS-S-35513	53.160294	−27.746675	16530	2.82 ± 0.657	1450 ± 1150
GOODS-S-35714	53.081291	−27.745722	15129	1.86 ± 0.457	529 ± 241
GOODS-S-36073	53.038231	−27.743839	16540	2.80 ± 0.665	588 ± 260
GOODS-S-36656	53.130169	−27.740917	16700	4.60 ± 1.10	10900 ± 48500
GOODS-S-36739	53.132965	−27.740108	13390	1.80 ± 0.527	1050 ± 873
GOODS-S-36890	53.062534	−27.739180	13790	1.47 ± 0.400	7910 ± 51800
GOODS-S-37211	53.136803	−27.737320	16590	2.88 ± 0.410	5820 ± 10100
GOODS-S-37233	53.202164	−27.737148	15680	1.93 ± 0.341	595 ± 208
GOODS-S-37616	53.197071	−27.735155	15730	2.54 ± 0.670	1260 ± 1150
GOODS-S-37773	53.080383	−27.734272	15220	1.30 ± 0.283	869 ± 603
GOODS-S-37865	53.135727	−27.733997	10900	5.95 ± 1.56	8420 ± 20800
GOODS-S-38508	53.071354	−27.730522	12270	0.818 ± 0.203	636 ± 565
GOODS-S-38614	53.079086	−27.729860	16070	1.72 ± 0.412	792 ± 501
GOODS-S-38999	53.088158	−27.727924	15270	4.53 ± 0.588	2520 ± 1460
GOODS-S-39020	53.154190	−27.727722	12080	1.56 ± 0.422	1480 ± 1510
GOODS-S-39093	53.180206	−27.727386	15450	1.95 ± 0.302	3780 ± 5270
GOODS-S-39891	53.058483	−27.723749	12460	1.75 ± 0.475	4490 ± 13200
GOODS-S-39944	53.062878	−27.723473	14370	1.10 ± 0.291	836 ± 484
GOODS-S-39995	53.085678	−27.723227	11650	5.05 ± 1.15	2120 ± 1790
GOODS-S-40010	53.021114	−27.723181	15650	5.57 ± 1.09	2520 ± 2100
GOODS-S-40752	53.073952	−27.719454	15890	1.58 ± 0.368	3760 ± 6350
GOODS-S-40926	53.077583	−27.718615	15140	0.884 ± 0.250	1860 ± 2100
GOODS-S-41237	53.156258	−27.717184	12790	4.77 ± 1.27	6010 ± 13000
GOODS-S-41527	53.171104	−27.715782	16210	1.04 ± 0.296	1890 ± 2250
GOODS-S-41624	53.156487	−27.715296	15109	1.34 ± 0.279	589 ± 231
GOODS-S-42020	53.154911	−27.713547	16740	3.94 ± 0.927	4400 ± 8020
GOODS-S-42028	53.011955	−27.713436	14380	1.91 ± 0.498	1060 ± 642
GOODS-S-42377	53.156101	−27.711914	15670	2.50 ± 0.749	907 ± 604
GOODS-S-42588	53.119099	−27.711081	11690	1.70 ± 0.445	1980 ± 2460
GOODS-S-44189	53.150974	−27.703297	13830	2.55 ± 0.668	1980 ± 2140
GOODS-S-45395	53.114685	−27.697918	14080	2.90 ± 0.765	1250 ± 912
GOODS-S-45709	53.089172	−27.696491	13070	1.09 ± 0.264	817 ± 768
GOODS-S-46507	53.134598	−27.693270	11900	2.22 ± 0.547	1070 ± 842
GOODS-S-46799	53.136749	−27.691959	15360	1.11 ± 0.306	802 ± 573
GOODS-S-48034	53.143993	−27.686104	15300	3.19 ± 0.864	3210 ± 4990
GOODS-S-48242	53.108574	−27.684887	13070	2.84 ± 0.646	1730 ± 1560
UDS-3944	34.356743	−5.2631712	16359	4.77 ± 0.904	695 ± 305
UDS-4172	34.381718	−5.2622500	13930	1.52 ± 0.416	1460 ± 3030
UDS-4420	34.411602	−5.2613540	13300	1.43 ± 0.329	546 ± 379
UDS-4468	34.463631	−5.2612281	15220	4.57 ± 1.10	2700 ± 3640
UDS-4515	34.371998	−5.2610588	14320	0.536 ± 0.130	586 ± 452
UDS-4590	34.259110	−5.2608008	12720	4.29 ± 0.910	1620 ± 1330
UDS-4714	34.384975	−5.2604699	11840	3.08 ± 0.782	1750 ± 1940

Table 5
(Continued)

ID	R.A.	Decl.	Observed Wavelength (Å)	Line Flux	Line EW
UDS-4961	34.482208	−5.2596869	15149	2.25 ± 0.300	1130 ± 816
UDS-5984	34.481194	−5.2564459	15920	2.22 ± 0.487	1140 ± 771
UDS-6077	34.282188	−5.2560658	12850	5.46 ± 1.34	2110 ± 2210
UDS-6147	34.264660	−5.2557688	15270	3.17 ± 0.718	1390 ± 987
UDS-6233	34.397949	−5.2554841	11120	3.78 ± 1.04	2100 ± 2370
UDS-6654	34.326962	−5.2541118	15780	2.85 ± 0.667	724 ± 348
UDS-7078	34.300163	−5.2525988	12230	2.28 ± 0.465	679 ± 349
UDS-7176	34.273342	−5.2522488	14590	3.73 ± 0.725	1830 ± 1230
UDS-7612	34.473457	−5.2508569	10950	10.2 ± 2.09	2400 ± 1600
UDS-7657	34.363434	−5.2505512	16050	1.61 ± 0.420	543 ± 289
UDS-7710	34.373959	−5.2503719	13220	1.13 ± 0.316	808 ± 785
UDS-8261	34.310520	−5.2483158	12270	2.81 ± 0.701	977 ± 677
UDS-8670	34.436985	−5.2468529	16600	1.93 ± 0.391	717 ± 376
UDS-8983	34.397579	−5.2458019	13710	4.05 ± 0.877	2090 ± 2100
UDS-9254	34.419018	−5.2448812	14330	3.27 ± 0.643	592 ± 236
UDS-9285	34.483704	−5.2447600	13140	3.19 ± 0.820	2670 ± 4230
UDS-9681	34.238365	−5.2433600	13130	3.80 ± 0.897	1840 ± 1860
UDS-9762	34.277752	−5.2430530	13550	3.04 ± 0.785	542 ± 282
UDS-9764	34.441158	−5.2431631	12970	5.16 ± 1.36	7170 ± 21300
UDS-9987	34.322662	−5.2423291	14500	2.54 ± 0.657	547 ± 251
UDS-10130	34.304348	−5.2418809	12250	1.94 ± 0.478	1670 ± 2220
UDS-10192	34.465969	−5.2418342	13180	3.24 ± 0.735	946 ± 548
UDS-10551	34.352684	−5.2404628	13150	8.19 ± 1.88	3090 ± 4280
UDS-10634	34.255905	−5.2402310	14460	2.43 ± 0.603	584 ± 262
UDS-11655	34.331963	−5.2367978	13210	4.20 ± 0.850	2570 ± 2940
UDS-11838	34.313549	−5.2361832	12850	2.67 ± 0.721	105000 ± 5150000
UDS-12030	34.403843	−5.2355752	16800	1.68 ± 0.243	697 ± 262
UDS-12373	34.387806	−5.2344308	13759	2.97 ± 0.738	2270 ± 4100
UDS-12519	34.409492	−5.2339659	16330	2.17 ± 0.555	3040 ± 5090
UDS-12527	34.318436	−5.2339358	14390	3.97 ± 0.655	802 ± 319
UDS-12570	34.342007	−5.2338119	15029	2.15 ± 0.562	1140 ± 822
UDS-13227	34.255383	−5.2314129	14680	1.22 ± 0.334	726 ± 510
UDS-13346	34.458286	−5.2309790	14790	3.97 ± 0.441	891 ± 277
UDS-13540	34.418243	−5.2304130	12340	3.69 ± 0.888	598 ± 270
UDS-13839	34.254360	−5.2294059	16830	2.53 ± 0.664	3890 ± 7050
UDS-13934	34.489922	−5.2290649	13520	2.59 ± 0.673	1600 ± 1960
UDS-14030	34.243992	−5.2287049	16090	1.79 ± 0.455	2310 ± 3090
UDS-14711	34.324570	−5.2264128	13040	2.59 ± 0.641	1520 ± 1580
UDS-14788	34.244946	−5.2261381	13830	1.84 ± 0.502	2630 ± 6560
UDS-15150	34.241528	−5.2248201	15410	2.22 ± 0.489	2510 ± 3620
UDS-15793	34.284569	−5.2227812	15300	1.43 ± 0.345	2540 ± 3590
UDS-16138	34.241039	−5.2216148	14310	2.30 ± 0.377	666 ± 222
UDS-16698	34.271542	−5.2197790	15980	2.35 ± 0.632	6180 ± 17200
UDS-16796	34.395519	−5.2194901	12740	4.65 ± 1.07	2210 ± 2920
UDS-17039	34.239960	−5.2186360	15129	1.40 ± 0.325	651 ± 354
UDS-17349	34.249008	−5.2176342	11990	1.77 ± 0.456	2550 ± 4920
UDS-17451	34.275620	−5.2173061	13970	3.44 ± 0.850	1020 ± 911
UDS-17455	34.445862	−5.2172990	12730	3.11 ± 0.841	30000 ± 453000
UDS-18119	34.381920	−5.2150989	13870	1.17 ± 0.304	737 ± 804
UDS-18138	34.469048	−5.2150412	13970	2.24 ± 0.504	1140 ± 1400
UDS-18207	34.275715	−5.2148018	15400	1.42 ± 0.359	669 ± 354
UDS-18209	34.325489	−5.2147951	13530	4.49 ± 1.02	2080 ± 2690
UDS-18590	34.456730	−5.2134881	14540	2.40 ± 0.625	679 ± 370
UDS-18744	34.462769	−5.2129769	10980	8.11 ± 2.11	4650 ± 6610
UDS-18934	34.374104	−5.2128448	14330	5.10 ± 0.835	659 ± 224
UDS-19124	34.324009	−5.2118592	15720	3.77 ± 0.643	1550 ± 1080
UDS-19205	34.430996	−5.2115769	13990	3.46 ± 0.513	1290 ± 1140
UDS-19291	34.245831	−5.2113118	15330	2.17 ± 0.494	15500 ± 102000
UDS-19335	34.260773	−5.2111988	12210	2.24 ± 0.527	646 ± 345
UDS-19635	34.269253	−5.2100992	12260	1.20 ± 0.326	1300 ± 1950
UDS-19857	34.239243	−5.2092709	13400	3.14 ± 0.861	5910 ± 24600
UDS-20385	34.252178	−5.2074342	16600	3.44 ± 0.891	1710 ± 1530
UDS-20651	34.448982	−5.2064390	12450	1.80 ± 0.471	1420 ± 1710
UDS-21042	34.361858	−5.2051449	14040	3.27 ± 0.617	1490 ± 1200

Table 5
(Continued)

ID	R.A.	Decl.	Observed Wavelength (Å)	Line Flux	Line EW
UDS-21149	34.281872	−5.2047229	12310	4.81 ± 1.16	7890 ± 27300
UDS-21168	34.360336	−5.2047081	15720	4.97 ± 1.23	6240 ± 16600
UDS-21514	34.397366	−5.2035170	16090	2.48 ± 0.573	784 ± 481
UDS-21584	34.358963	−5.2033010	14460	2.52 ± 0.536	8740 ± 25700
UDS-21705	34.428501	−5.2029219	16220	2.08 ± 0.483	1640 ± 1460
UDS-21754	34.432354	−5.2027760	13460	2.01 ± 0.539	690 ± 444
UDS-21993	34.378662	−5.2019458	15580	2.39 ± 0.583	1020 ± 691
UDS-22163	34.273380	−5.2013412	13610	3.04 ± 0.837	719 ± 428
UDS-22434	34.403641	−5.2004881	13270	4.00 ± 1.07	1630 ± 1640
UDS-22750	34.469639	−5.1993928	12030	4.63 ± 1.11	3770 ± 5830
UDS-22853	34.272697	−5.1990681	13430	5.58 ± 0.744	1220 ± 797
UDS-23286	34.427734	−5.1977329	12290	2.02 ± 0.532	7590 ± 41700
UDS-23880	34.429932	−5.1956048	12840	3.51 ± 0.927	2790 ± 4490
UDS-23966	34.270290	−5.1953211	12200	5.75 ± 1.46	41300 ± 572000
UDS-24366	34.464279	−5.1940060	12400	4.13 ± 0.989	3440 ± 5500
UDS-24734	34.344379	−5.1928968	14440	2.01 ± 0.471	4660 ± 12600
UDS-24914	34.292206	−5.1921420	12970	4.05 ± 1.08	656 ± 434
UDS-24916	34.386250	−5.1921592	14490	2.35 ± 0.504	90200 ± 3810000
UDS-24941	34.447327	−5.1920629	14300	2.67 ± 0.533	1840 ± 1600
UDS-25083	34.278004	−5.1916781	16610	3.92 ± 0.921	1000 ± 578
UDS-25117	34.432549	−5.1915650	13400	7.56 ± 1.96	1990 ± 2270
UDS-25559	34.365070	−5.1900358	14730	1.33 ± 0.352	1090 ± 820
UDS-26121	34.282532	−5.1881309	14580	2.47 ± 0.359	1570 ± 1110
UDS-26268	34.485104	−5.1875911	12490	5.65 ± 1.15	1550 ± 1190
UDS-26269	34.440235	−5.1875911	13510	4.19 ± 1.04	2120 ± 2500
UDS-26407	34.324097	−5.1871338	13490	1.98 ± 0.568	2360 ± 4760
UDS-26459	34.290421	−5.1869621	13070	2.02 ± 0.477	835 ± 679
UDS-26538	34.291920	−5.1868200	14240	4.93 ± 1.03	962 ± 495
UDS-26618	34.480045	−5.1864872	11530	4.43 ± 1.01	11600 ± 52600
UDS-26705	34.481541	−5.1862388	13710	3.48 ± 0.861	518 ± 245
UDS-27230	34.426254	−5.1843290	16319	1.80 ± 0.411	596 ± 320
UDS-27865	34.372444	−5.1821599	11890	2.56 ± 0.633	716 ± 391
UDS-27895	34.344437	−5.1820588	11040	4.18 ± 0.995	2550 ± 2680
UDS-28292	34.259445	−5.1808429	12000	4.00 ± 0.944	2910 ± 3740
UDS-28727	34.408569	−5.1792831	12270	1.28 ± 0.288	2460 ± 7660
UDS-29074	34.404392	−5.1781740	15660	1.91 ± 0.493	2100 ± 2510
UDS-29115	34.378376	−5.1780520	14580	2.14 ± 0.386	1020 ± 469
UDS-29273	34.266163	−5.1774888	15360	1.29 ± 0.280	4030 ± 8890
UDS-29622	34.393024	−5.1763658	14130	5.84 ± 0.876	15900 ± 62300
UDS-29640	34.424297	−5.1762972	13540	3.16 ± 0.852	1660 ± 2090
UDS-29822	34.270069	−5.1758070	12220	10.2 ± 0.980	579 ± 97.9
UDS-29917	34.445358	−5.1754122	14100	3.56 ± 0.803	2740 ± 3280
UDS-29973	34.472187	−5.1752620	12640	1.67 ± 0.372	790 ± 633
UDS-30016	34.446590	−5.1751261	13110	3.04 ± 0.783	1890 ± 2520
UDS-30376	34.449577	−5.1739521	11660	8.08 ± 2.11	6320 ± 14600
UDS-30668	34.246864	−5.1730609	14650	3.64 ± 0.795	1420 ± 1020
UDS-31031	34.279873	−5.1718512	10830	6.90 ± 1.60	5330 ± 8540
UDS-31590	34.422554	−5.1703358	11220	4.78 ± 1.23	1180 ± 768
UDS-31871	34.484814	−5.1691728	12070	2.36 ± 0.628	8980 ± 47900
UDS-32628	34.431049	−5.1665592	13240	1.62 ± 0.302	605 ± 375
UDS-32944	34.367519	−5.1654339	11490	5.17 ± 1.07	22000 ± 191000
UDS-33192	34.337292	−5.1646581	14880	2.47 ± 0.621	832 ± 446
UDS-33306	34.321411	−5.1642699	14940	2.48 ± 0.515	5660 ± 13400
UDS-33520	34.273167	−5.1634960	13870	2.32 ± 0.586	841 ± 646
UDS-33616	34.380295	−5.1631808	13350	4.03 ± 0.783	1710 ± 1810
UDS-33727	34.315407	−5.1627512	14170	1.24 ± 0.305	565 ± 364
UDS-33910	34.287861	−5.1621542	14380	3.29 ± 0.746	1320 ± 982
UDS-33940	34.330647	−5.1621590	11570	3.30 ± 0.773	1660 ± 1520
UDS-34078	34.477646	−5.1617222	13530	3.54 ± 0.934	872 ± 557
UDS-34123	34.410664	−5.1614938	15990	2.16 ± 0.476	2050 ± 2200
UDS-34158	34.326962	−5.1613898	13030	2.60 ± 0.583	1410 ± 1420
UDS-34550	34.250740	−5.1600089	12160	2.15 ± 0.524	2050 ± 3180
UDS-34830	34.404507	−5.1590190	15590	1.95 ± 0.467	3340 ± 5820
UDS-34986	34.265911	−5.1584430	14200	2.87 ± 0.661	969 ± 583

Table 5
(Continued)

ID	R.A.	Decl.	Observed Wavelength (Å)	Line Flux	Line EW
UDS-35263	34.420460	−5.1574821	16000	1.58 ± 0.367	654 ± 431
UDS-35671	34.376427	−5.1560769	13110	1.90 ± 0.501	10200 ± 84700
UDS-35677	34.357334	−5.1560640	14100	3.58 ± 0.929	17800 ± 104000
UDS-35804	34.442146	−5.1555982	12560	2.65 ± 0.661	827 ± 515
UDS-36332	34.332657	−5.1538491	15480	5.11 ± 1.04	1190 ± 763
UDS-37099	34.576797	−5.1510220	16510	2.42 ± 0.612	2560 ± 3890
UDS-37129	34.256027	−5.1508918	14090	2.65 ± 0.649	977 ± 532
UDS-37347	34.359085	−5.1500411	12750	1.87 ± 0.457	907 ± 718
UDS-37694	34.582539	−5.1489148	15340	3.01 ± 0.767	2100 ± 2430
UDS-37824	34.256012	−5.1484051	15480	3.16 ± 0.457	684 ± 245
UDS-38006	34.276001	−5.1477509	15820	2.76 ± 0.512	64400 ± 1310000
UDS-38232	34.360844	−5.1470180	12070	3.92 ± 0.874	3490 ± 6140
UDS-38332	34.325348	−5.1467652	12380	5.17 ± 0.915	1160 ± 614
UDS-39034	34.253468	−5.1440878	12470	2.08 ± 0.497	5740 ± 23300
UDS-39355	34.337891	−5.1428971	11240	5.50 ± 1.36	26900 ± 243000
UDS-39657	34.291096	−5.1417279	13890	2.33 ± 0.638	848 ± 652
UDS-39687	34.365822	−5.1416449	11990	1.87 ± 0.445	3540 ± 9670
UDS-40509	34.354115	−5.1387291	14330	1.15 ± 0.302	964 ± 671
UDS-40829	34.345165	−5.1375790	14110	2.03 ± 0.407	926 ± 534
UDS-41487	34.368279	−5.1356001	15420	2.83 ± 0.510	869 ± 359
UDS-43331	34.367249	−5.1287551	12730	4.47 ± 0.921	1170 ± 715
UDS-43337	34.365799	−5.1286812	13759	6.77 ± 1.43	636 ± 276

Note. ID numbers come from Skelton et al. (2014); all EW values are quoted in the observed frame (Å); fluxes are in units of 10^{-17} erg s^{-1} cm^{-2}.

ORCID iDs

Michael V. Maseda https://orcid.org/0000-0003-0695-4414
Arjen van der Wel https://orcid.org/0000-0002-5027-0135
Hans-Walter Rix https://orcid.org/0000-0003-4996-9069
Ivelina Momcheva https://orcid.org/0000-0003-1665-2073
Gabriel B. Brammer https://orcid.org/0000-0003-2680-005X
Marijn Franx https://orcid.org/0000-0002-8871-3026
Britt F. Lundgren https://orcid.org/0000-0002-6463-2483
Rosalind E. Skelton https://orcid.org/0000-0001-7393-3336
Katherine E. Whitaker https://orcid.org/0000-0001-7160-3632

References

Amorín, R. O., Pérez-Montero, E., Contini, T., et al. 2014a, A&A, 578, A105
Amorín, R. O., Sommariva, V., Castellano, M., et al. 2014b, A&A, 568L, 8
Atek, H., Malkan, M., McCarthy, P., et al. 2010, ApJ, 723, 104
Blanton, M. R., & Roweis, S. 2007, AJ, 133, 734
Boerner, G., Mo, H., & Zhou, Y. 1989, A&A, 221, 191
Brammer, G. B., Sánchez-Janssen, R., Labbé, I., et al. 2012a, ApJL, 758, L17
Brammer, G. B., van Dokkum, P., & Coppi, P. 2008, ApJ, 686, 1503
Brammer, G. B., van Dokkum, P., Franx, M., et al. 2012b, ApJS, 200, 13
Bruzual, G., & Charlot, S. 2003, MNRAS, 344, 1000
Cardamone, C., Schawinski, K., Sarzi, M., et al. 2009, MNRAS, 399, 1191
Cooke, J. 2009, ApJL, 704, L62
Ferreras, I., Pasquali, A., Khochfar, S., et al. 2012, AJ, 144, 47
Fioc, M., & Rocca-Volmerange, B. 1997, A&A, 326, 950
Grogin, N., Kocevski, D., Faber, S., et al. 2011, ApJS, 197, 35
Hathi, N. P., Ferreras, I., Pasquali, A., et al. 2009, ApJ, 690, 1866
Kakazu, Y., Cowie, L. L., & Hu, E. M., 2007, ApJ, 668, 853
Kennicutt, R. C., Jr. 1998, ARA&A, 36, 189
Koekemoer, A., Faber, S., Ferguson, H., et al. 2011, ApJS, 197, 36
Kümmel, M., Walsh, J. R., Pirzkal, N., Kuntschner, H., & Pasquali, A. 2009, PASP, 121, 59
Lilly, S. J., Le Févre, O., Renzini, A., et al. 2007, ApJS, 172, 70
Malhotra, S., Rhoads, J. E., Pirzkal, N., et al. 2005, ApJ, 626, 666
Maseda, M. V., van der Wel, A., da Cunha, E., et al. 2013, ApJL, 778, L22
Maseda, M. V., van der Wel, A., Rix, H.-W., et al. 2014, ApJ, 791, 17
Masters, D., McCarthy, P., Burgasser, A. J., et al. 2012, ApJL, 752, L14
Meurer, G. R., Tsvetanov, Z. I., Gronwall, C., et al. 2007, ApJ, 134, 77
Momcheva, I. G., Brammer, G. B., van Dokkum, P., et al. 2016, ApJS, 225, 27
Nelson, E. J., van Dokkum, P. G., Brammer, G. B., et al. 2012, ApJL, 747, L28
Patel, S. G., Fumagalli, M., Franx, M., et al. 2013, ApJ, 778, 115
Pirzkal, N., Rothberg, B., Ly, C., et al. 2013, ApJ, 772, 48
Pirzkal, N., Xu, C., Malhotra, S., et al. 2004, ApJS, 154, 501
Rhoads, J. E., Malhotra, S., Pirzkal, N., et al. 2009, ApJ, 697, 942
Schmidt, K., Rix, H.-W., da Cunha, E., et al. 2013, MNRAS, 432, 285
Skelton, R. E., Whitaker, K. E., Momcheva, I. G., et al. 2014, ApJS, 214, 24
Smit, R., Bouwens, R. J., Labbé, I., et al. 2014, ApJ, 784, 58
Straughn, A. N., Meurer, G., Pirzkal, N., et al. 2008, AJ, 135, 1624
van der Wel, A., Straughn, A., Rix, H.-W., et al. 2011, ApJ, 742, 111
van der Wel, A., van de Ven, G., Maseda, M., et al. 2013, ApJL, 777, L17
van Dokkum, P. G., Brammer, G. B., Fumagalli, M., et al. 2011, ApJL, 743, L15
van Dokkum, P. G., Leja, J., Nelson, E. J., et al. 2013, ApJL, 771, L35